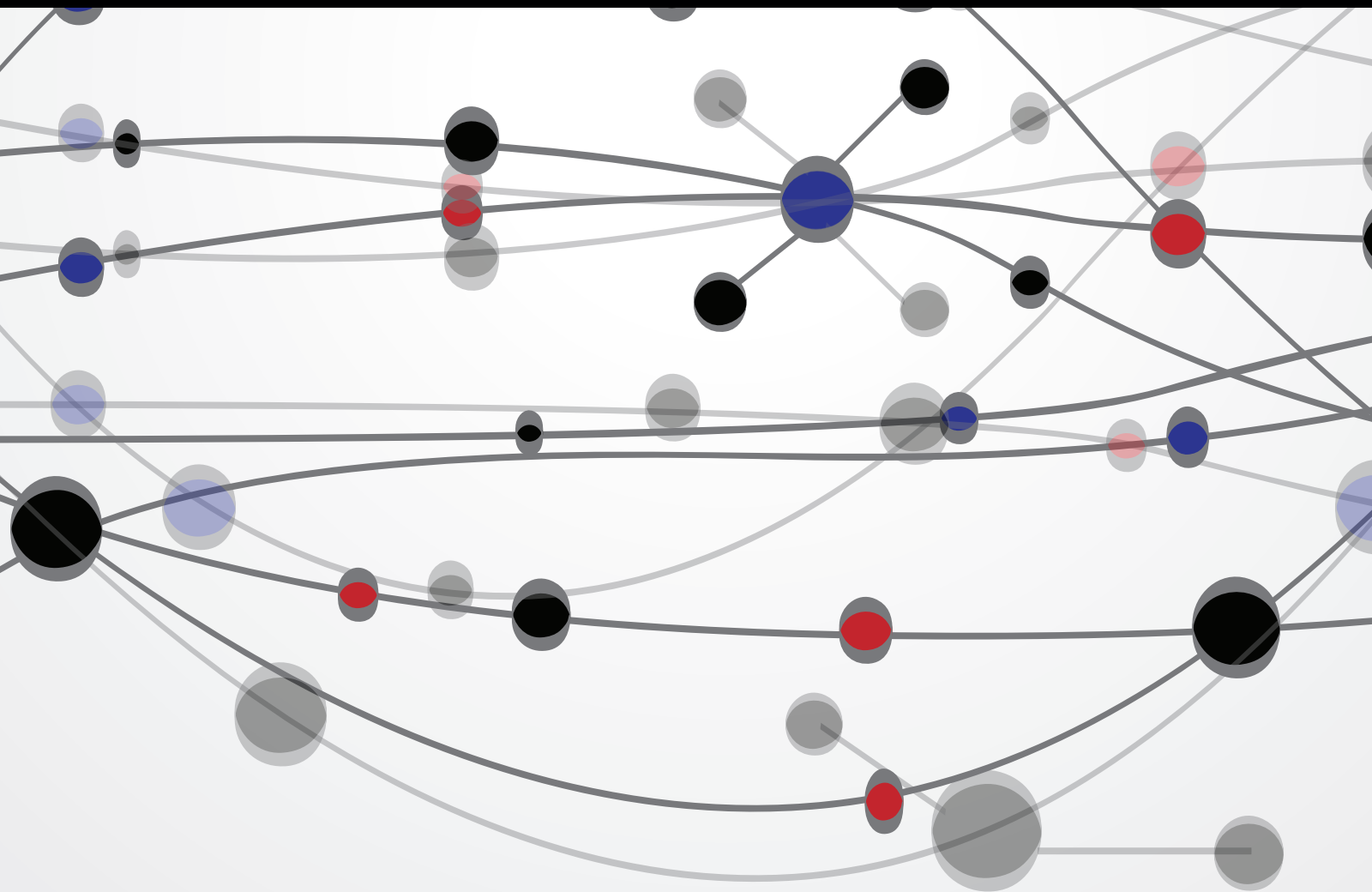


Wireless Networks and Mobile Communications for Internet of Things

Guest Editors: Shukui Zhang, Dajin Wang, Shan Lin, Hongli Xu, and Juncheng Jia





Wireless Networks and Mobile Communications for Internet of Things

The Scientific World Journal

Wireless Networks and Mobile Communications for Internet of Things

Guest Editors: Shukui Zhang, Dajin Wang, Shan Lin,
Hongli Xu, and Juncheng Jia



Copyright © 2015 Hindawi Publishing Corporation. All rights reserved.

This is a special issue published in “The Scientific World Journal.” All articles are open access articles distributed under the Creative Commons Attribution License, which permits unrestricted use, distribution, and reproduction in any medium, provided the original work is properly cited.

Contents

Computer Simulation and Field Experiment for Downlink Multiuser MIMO in Mobile WiMAX System,
Kazuhiro Yamaguchi, Takaharu Nagahashi, Takuya Akiyama, Hideaki Matsue, Kunio Uekado,
Takakazu Namera, Hiroshi Fukui, and Satoshi Nanamatsu
Volume 2015, Article ID 481676, 10 pages

Calibration of Smartphone-Based Weather Measurements Using Pairwise Gossip,
Jane Louie Fresco Zamora, Shigeru Kashihara, and Suguru Yamaguchi
Volume 2015, Article ID 494687, 9 pages

An Active Learning Approach with Uncertainty, Representativeness, and Diversity, Tianxu He,
Shukui Zhang, Jie Xin, Pengpeng Zhao, Jian Wu, Xuefeng Xian, Chunhua Li, and Zhiming Cui
Volume 2014, Article ID 827586, 6 pages

Optimization of Self-Directed Target Coverage in Wireless Multimedia Sensor Network, Yang Yang,
Yufei Wang, Dechang Pi, and Ruchuan Wang
Volume 2014, Article ID 416218, 9 pages

RSSI-Based Smooth Localization for Indoor Environment, Yujian Wang, Bin Zhao, and Zhaohui Jiang
Volume 2014, Article ID 639142, 8 pages

**A Novel Deployment Scheme Based on Three-Dimensional Coverage Model for Wireless Sensor
Networks,** Fu Xiao, Yang Yang, Ruchuan Wang, and Lijuan Sun
Volume 2014, Article ID 846784, 7 pages

Research Article

Computer Simulation and Field Experiment for Downlink Multiuser MIMO in Mobile WiMAX System

Kazuhiro Yamaguchi,¹ Takaharu Nagahashi,¹ Takuya Akiyama,¹ Hideaki Matsue,¹ Kunio Uekado,² Takakazu Namera,³ Hiroshi Fukui,³ and Satoshi Nanamatsu⁴

¹Department of Computer and Media Engineering, Tokyo University of Science, Suwa 5000-1, Toyohira, Chino-shi, Nagano 391-0292, Japan

²Azumino City, Nagano, Japan

³MIRAIT Technologies Corporation, Japan

⁴NPO CCC21L, Japan

Correspondence should be addressed to Kazuhiro Yamaguchi; yamaguchi@rs.tus.ac.jp and Hideaki Matsue; matsue@rs.suwa.tus.ac.jp

Received 10 October 2014; Revised 4 March 2015; Accepted 24 March 2015

Academic Editor: Dimitrios A. Karras

Copyright © 2015 Kazuhiro Yamaguchi et al. This is an open access article distributed under the Creative Commons Attribution License, which permits unrestricted use, distribution, and reproduction in any medium, provided the original work is properly cited.

The transmission performance for a downlink mobile WiMAX system with multiuser multiple-input multiple-output (MU-MIMO) systems in a computer simulation and field experiment is described. In computer simulation, a MU-MIMO transmission system can be realized by using the block diagonalization (BD) algorithm, and each user can receive signals without any signal interference from other users. The bit error rate (BER) performance and channel capacity in accordance with modulation schemes and the number of streams were simulated in a spatially correlated multipath fading environment. Furthermore, we propose a method for evaluating the transmission performance for this downlink mobile WiMAX system in this environment by using the computer simulation. In the field experiment, the received power and downlink throughput in the UDP layer were measured on an experimental mobile WiMAX system developed in Azumino City in Japan. In comparison with the simulated and experimented results, the measured maximum throughput performance in the downlink had almost the same performance as the simulated throughput. It was confirmed that the experimental mobile WiMAX system for MU-MIMO transmission successfully increased the total channel capacity of the system.

1. Introduction

Recently, increasing channel capacity and improving system performance are serious challenges for high speed wireless communication systems. To overcome these, multiple-input multiple-output (MIMO) techniques [1, 2] are employed such as long term evolution (LTE), IEEE 802.11n, and Worldwide Interoperability for Microwave Access (WiMAX). Multiple antennas can be used for increasing data rates through multiplexing or for improving performance through diversity such as in single user MIMO (SU-MIMO) systems. Multiuser systems with multiple antennas at the transmitters and/or receivers are called multiuser MIMO (MU-MIMO) systems. The SU-MIMO system can improve the channel capacity for only one user; however, there is some limitation in increasing

the number of receiving antennas on mobile stations. The MU-MIMO [3] system can also improve the total channel capacity by increasing the number of mobile stations, and MU-MIMO systems have been already researched for wireless communications with high wireless link capacity such as LTE-Advanced and IEEE 802.11ac technologies.

Many researchers have reported field experimental results with the 3.5-GHz frequency band [4, 5]. The 2.5-GHz frequency band has been allocated in Japan, and an experimental mobile WiMAX system was developed in Azumino City in Japan [6, 7]. A network service and applications have been provided to citizens within the local wireless network area. Base stations (BSs) complying with the mobile WiMAX based on IEEE 802.16e standard [8] were installed in 2009 and 2010 to increase the channel quality and channel capacity of

the system. As previous work, the basic throughput performance in a field experiment under a static condition of MU-MIMO transmission with the mobile WiMAX system was reported [9], and the RSSI and throughput performances within 500 m from the BS were measured [10]. In this paper, the transmission performance for downlink MU-MIMO systems based on the experimental mobile WiMAX system is evaluated with a computer simulation and field experiment. A MU-MIMO system based on the experimental mobile WiMAX system is constructed as a transmitter with 6 antennas and receivers with 2 antennas, and the number of streams is 1-2. In computer simulation, a MU-MIMO transmission system can be realized by using the block diagonalization (BD) algorithm. Transmission performances are evaluated in terms of bit error rate (BER) performance and a channel capacity in a spatially correlated multipath fading environment. Furthermore, in such an environment, we propose a method for evaluating transmission performance for the mobile WiMAX system with MU-MIMO by using the computer simulation. In the field experiment, received power and throughput performances for the downlink experimental mobile WiMAX system with MU-MIMO are measured. We show the transmission performance with the proposed evaluation method for the mobile WiMAX system with MU-MIMO under the spatially correlated multipath fading environment.

This paper consists of the following sections. In Section 2, we describe a system model and procedures for MU-MIMO transmission with the BD algorithm. In Section 3, we describe the results of the computer simulation and details of the proposed evaluation method, and in Section 4, we describe and analyze the results of the field experiment. In Section 5, we discuss the result of computational and field experimental results on interference. Finally, Section 6 concludes this paper.

2. Downlink MU-MIMO System Model

A downlink mobile WiMAX system model based on the IEEE 802.16e standard is constructed in this paper. The model with MU-MIMO technique is shown in Figure 1. N_T denotes the number of transmitting antennas at the base station, and N_R denotes the number of receiving antennas at a user. The maximum number of transmitting streams is 3; therefore, the number of users is 1-3 in the computer simulation described in Section 3. The number of transmitting and receiving antennas is determined with the experimental mobile WiMAX system in the field experiment described in Section 4.

In Figure 1, \mathbf{x}_k and \mathbf{y}_k , respectively, denote the input and output signals for k th user, where $k = 1, 2, \dots, K$. In the MU-MIMO transmission for the k th user, the input signal is multiplied by a weight matrix at the transmitter for the k th user \mathbf{W}_{Tk} ; then, it is transmitted to the user. The received signal for the k th user \mathbf{r}_k is also multiplied by a weight matrix at the receiver for the k th user \mathbf{W}_{Rk} ; then, output signal is obtained.

In this paper, we assumed that the MU-MIMO system is based on the OFDM system and that the subcarriers are influenced by flat fading through channels. When an input

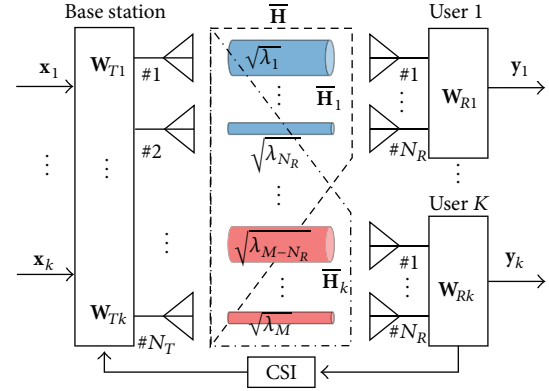


FIGURE 1: System model for downlink MU-MIMO system.

signal \mathbf{x}_k for the k th user is transmitted in this situation, the received signal for k th user is given by

$$\mathbf{r}_k = \mathbf{H}_k \sum_{i=1}^K \mathbf{W}_{Ti} \mathbf{x}_i = \mathbf{H}_k \mathbf{W}_{Tk} \mathbf{x}_k + \mathbf{H}_k \sum_{i=1, i \neq k}^K \mathbf{W}_{Ti} \mathbf{x}_i. \quad (1)$$

Here, noise components are ignored. In this equation, \mathbf{H}_k denotes the MIMO channel state matrix for the k th user, and K denotes the maximum number of users. Here, we assumed that the MIMO channel state information is perfectly received by the transmitter from the receivers.

The output signal for k th user \mathbf{y}_k is given by

$$\mathbf{y}_k = \mathbf{W}_{Rk} \mathbf{r}_k = \mathbf{W}_{Rk} \mathbf{H}_k \mathbf{W}_{Tk} \mathbf{x}_k + \mathbf{W}_{Rk} \mathbf{H}_k \sum_{i=1, i \neq k}^K \mathbf{W}_{Ti} \mathbf{x}_i. \quad (2)$$

In (2), the component $\mathbf{W}_{Rk} \mathbf{H}_k \mathbf{W}_{Tk} \mathbf{x}_k$ denotes the desired signal for the k th user, and the other components $\mathbf{W}_{Rk} \mathbf{H}_k \sum_{i=1, i \neq k}^K \mathbf{W}_{Ti} \mathbf{x}_i$ are the interference signals between the k th user and the other $K - 1$ users. Therefore, it is important for MU-MIMO transmission to eliminate the interference signals for each user.

In the conventional approaches for downlink MU-MIMO systems, dirty paper coding (DPC) [11] and BD algorithms [12] are well-known for multiuser detection. However, the DPC algorithm requires extremely high calculation cost. Therefore, to realize MU-MIMO transmission, we used the BD algorithm in this paper. In the MU-MIMO transmission system based on the BD algorithm, which includes linear pre- and postprocessing, the weight matrix at the transmitter must satisfy

$$\mathbf{H}_i \mathbf{W}_{Tj} = \mathbf{0} \quad \forall i, j \quad (1 \leq i, j \leq K). \quad (3)$$

Here, we assumed a new MIMO channel state matrix except for the k th user as follows:

$$\tilde{\mathbf{H}}_k = [\mathbf{H}_1^T \cdots \mathbf{H}_{k-1}^T \mathbf{H}_{k+1}^T \cdots \mathbf{H}_K^T], \quad (4)$$

where the operator $[\cdot]^T$ denotes a matrix transpose. The SVD of the matrix $\tilde{\mathbf{H}}_k$ is defined by

$$\tilde{\mathbf{H}}_k = \tilde{\mathbf{U}}_k \tilde{\Sigma}_k [\tilde{\mathbf{V}}_k^s \tilde{\mathbf{V}}_k^u]^H, \quad (5)$$

where the operator $[\cdot]^H$ denotes the Hermitian matrix transpose. In this equation, term $\tilde{\mathbf{V}}_k^s$ denotes the single space of all users except for the k th user, and term $\tilde{\mathbf{V}}_k^n$ denotes the null space that does not interfere without the other $K - 1$ users.

Because $\tilde{\mathbf{H}}_k \tilde{\mathbf{V}}_k^n = \mathbf{0}$, we can satisfy the condition in (3) by using the weight matrix $\tilde{\mathbf{V}}_k^n$.

After processing the block diagonalization, the MU-MIMO system can be achieved as K parallel SU-MIMO transmissions for each user.

In accordance with the SVD-SU-MIMO transmission [13–15] for the k th user, the SVD of the SVD-SU-MIMO channel state matrix $\tilde{\mathbf{H}}_k = \mathbf{H}_k \tilde{\mathbf{V}}_k^n$ is defined as

$$\tilde{\mathbf{H}}_k = \bar{\mathbf{U}}_k \bar{\boldsymbol{\Sigma}}_k [\bar{\mathbf{V}}_k^s \bar{\mathbf{V}}_k^n]^H, \quad (6)$$

where $\bar{\mathbf{U}}_k$ and $\bar{\mathbf{V}}_k^s$ are the left and right singular vectors, respectively, and $\bar{\boldsymbol{\Sigma}}_k$ is the diagonal matrix whose elements $\sqrt{\lambda_i}$ are the square roots of the null space eigenvalues. Thus, the weight matrix at the transmitter for SVD transmission is given as $\mathbf{W}_{Tk} = \tilde{\mathbf{V}}_k^n \bar{\mathbf{V}}_k^s$. By using the weight matrix at the receiver $\mathbf{W}_{Rk} = \bar{\mathbf{U}}_k^H$, the output signal for the k th user in (2) is rewritten as

$$\mathbf{y}_k = \bar{\boldsymbol{\Sigma}}_k \mathbf{x}_k. \quad (7)$$

In this equation, for example, the output signal for user 1 is represented as

$$\mathbf{y}_1 = \bar{\boldsymbol{\Sigma}}_1 \mathbf{x}_1 = \begin{bmatrix} \sqrt{\lambda_1} & \cdots & \mathbf{0} \\ \vdots & \ddots & \vdots \\ \mathbf{0} & \cdots & \sqrt{\lambda_{N_R}} \end{bmatrix} \mathbf{x}_1. \quad (8)$$

The MU-MIMO transmission without any interference between the k th user and the other users can be realized as parallel SVD-SU-MIMO transmission by using the above weight matrices at the transmitter and the receivers, and the quality of each parallel wireless link is different depending on the diagonal elements $\sqrt{\lambda_i}$ [3, 13–15].

Summarizing the above procedures, a transmitting weight matrix $\mathbf{W}_{Tk} = \tilde{\mathbf{V}}_k^n \bar{\mathbf{V}}_k^s$ is calculated by (5) and (6) by using the SVD operation with CSI. The input signal multiplied by the transmitting weight matrix is transmitted to the users. For each user, the receiving weight matrix $\mathbf{W}_{Rk} = \bar{\mathbf{U}}_k^H$ is calculated by (6) by using the SVD operation. The signal received by each user is multiplied by the receiving weight, and the output signal is obtained for each user.

Note that the above MU-MIMO transmission with BD algorithm can transmit signals only to the desired user without any interference between users under independently identically distributed (i.i.d.) channel conditions. In spatially correlated multipath fading environments, there are some interference values between received signals for each user [16].

3. Computer Simulation

3.1. Simulated Condition. To evaluate the system performance, we carried out a computer simulation by using

TABLE 1: Parameters for experimental mobile WiMAX system.

Parameters	Value
Frequency	2587 [MHz]
Bandwidth	10 [MHz]
Modulation scheme	QPSK/16QAM/64QAM
Convolutional code	1/2, 3/4, 5/6
Number of FFT points	1024
Effective OFDM symbol length	91.4 [μ s]
CP length	11.4 [μ s]
OFDM symbol length	102.9 [μ s]
Frame structure	OFDMA-TDD
Frame interval	5 [ms]
Number of OFDM symbols per frame	47
OFDM symbol ratio (DL : UL)	29 : 18
OFDM symbol ratio for data (DL : UL)	23 : 15
Number of transmitting antennas	6
Number of receiving antennas	2
Maximum number of streams	1 (Matrix A mode) 2 (Matrix A/B mode)
Channel model	12-ray Rayleigh fading model (Maximum delay is 3.3 [μ s])
Doppler frequency	5 [Hz]
Mode	Matrix A, Matrix A/B
Parameters for PUSC	DL/UL
Number of data subcarriers	720/560
Number of subchannels	30/35
Number of OFDM symbols per slot	2/3

the downlink MU-MIMO system shown in Figure 1. Table 1 lists the parameters for the simulations.

The parameters were determined in accordance with the experimental mobile WiMAX system based on the IEEE 802.16e standard. The downlink access scheme was OFDMA-TDD, and OFDM-QPSK, 16QAM, and 64QAM were used as modulation schemes. The number of transmitting antennas was 6, and the number of receiving antennas at one user was 2. The maximum number of streams was 3. In the MU-MIMO model, the frequency was 2587 MHz, and the bandwidth was 10 MHz. The input streams were modulated as QPSK, 16QAM, and 64QAM modulation scheme, and the number of streams was the same as the number of users. The number of FFT points was 1024. A 12-ray Rayleigh fading model whose maximum delay time is 3.3 μ s was used as the channel model, and the Doppler frequency was set to 5 Hz in consideration of transmission at walking speed.

3.2. BER Analysis. Figure 2 shows the average C/N versus the average BER in accordance with the number of streams and the modulation schemes under the multipath fading environment.

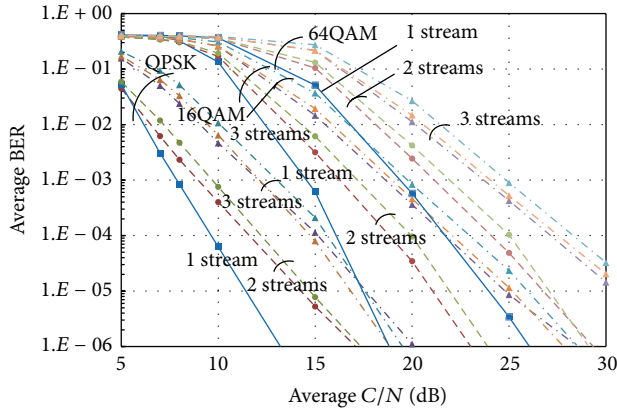


FIGURE 2: BER performance in accordance with modulation schemes and number of streams.

In the graph, the average BER performances are plotted for 1 user with 1 stream, for 2 users with 2 streams, and for 3 users with 3 streams in accordance with the modulation schemes. In the case of 1 stream, for example, a system having a BER of 10^{-6} required an average C/N of 13.2 dB in QPSK. However, the system having the same BER of 10^{-6} required an average C/N of 16.8 dB when the number of streams was 2. The difference of these required C/N s is 3.6 dB, and this indicates the interference signal value between signals for the other users. In the case of 3 streams, the system having the same BER of 10^{-6} required an average C/N of 21.6 dB. The interference values corresponded to C/I of 15.7 dB and 13.9 dB when the numbers of streams were 2 and 3, respectively.

The same as the result with QPSK modulation, systems having a BER of 10^{-6} required an average C/N of 20.8, 23.8, and 29.1 dB when the numbers of streams were 1, 2, and 3, respectively, in 16QAM. The interference values corresponded to C/I of 23.8 dB and 21.5 dB when the numbers of streams were 2 and 3, respectively. Furthermore, systems having a BER of 10^{-6} required an average C/N of 26.2, 30.0, and 34.7 dB when the numbers of streams were 1, 2, and 3, respectively, in 64QAM. The interference values corresponded to C/I of 28.5 dB and 26.6 dB when the numbers of streams were 2 and 3, respectively.

3.3. Channel Capacity Analysis. The total channel capacity on the MU-MIMO systems increased as the number of transmitting antennas and streams increased. Figure 3 shows the average $C/(N + I)$ versus the total channel capacity with the number of streams being 1–3 under the spatially correlated environment. The line and dashed-line in the graph denote the channel capacity under no correlated and spatially correlated Rayleigh fading environments, respectively.

In such an i.i.d. Rayleigh fading condition, the channel capacity based on the BD algorithm is calculated as

$$C_{BD} = \max \log_2 \mathbf{I} + \frac{\bar{\Sigma}^2 \Lambda}{\delta_n^2}, \quad (9)$$

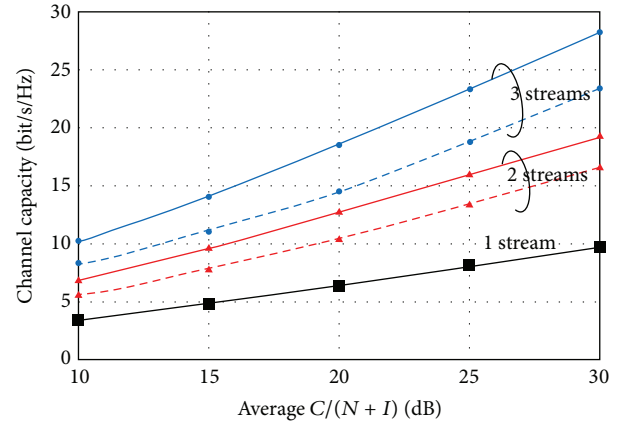


FIGURE 3: Channel capacity in accordance with spatially correlation and number of streams.

where

$$\bar{\Sigma} = \begin{bmatrix} \bar{\Sigma}_1 & \cdots & \mathbf{0} \\ \vdots & \ddots & \vdots \\ \mathbf{0} & \cdots & \bar{\Sigma}_K \end{bmatrix}. \quad (10)$$

The details for calculating C_{BD} are described in [17].

Since spatial correlation has played an important role in evaluating the SU-MIMO system, its effect can be applied to the MU-MIMO system. In spatially correlated Rayleigh fading environments, the channel capacity is lower than that in i.i.d. environments [17, 18]. To evaluate the transmission performance for the MU-MIMO system in a spatially correlated environment, we propose an evaluation method that uses computer simulation. Here, we calculated the transmission speed for the downlink mobile WiMAX system in order to evaluate the throughput performance in the field experiment described in Section 4. The downlink bandwidth is 10 MHz and the number of downlink subcarriers for data transmission is 720, so the downlink bandwidth for data transmission is $720/1024 \times 10 \text{ MHz} = 7.0 \text{ MHz}$. The maximum transmission speed for only 1 user in downlink is calculated as

$$\begin{aligned} \text{Transmission Speed} &= 6 \text{ [bit]} \times \frac{5}{6} \times 23 \times \frac{720}{5 \text{ [ms]}} \\ &= 16.17 \text{ [Mbps]}, \end{aligned} \quad (11)$$

where the primary modulation scheme is 64QAM, the convolutional coding rate is 5/6, and the number of OFDM symbols for data transmission per 1 OFDMA/TDD frame is 23.

Because only 23 OFDM symbols are used for downlink data transmission in 47 OFDM symbols per frame, the channel capacity per frequency with 1 stream can be calculated by

$$W_1 = \frac{16.17 \text{ [Mbps]} / 7 \text{ [MHz]}}{(23/47)} = 4.72 \text{ [bps/Hz]}. \quad (12)$$

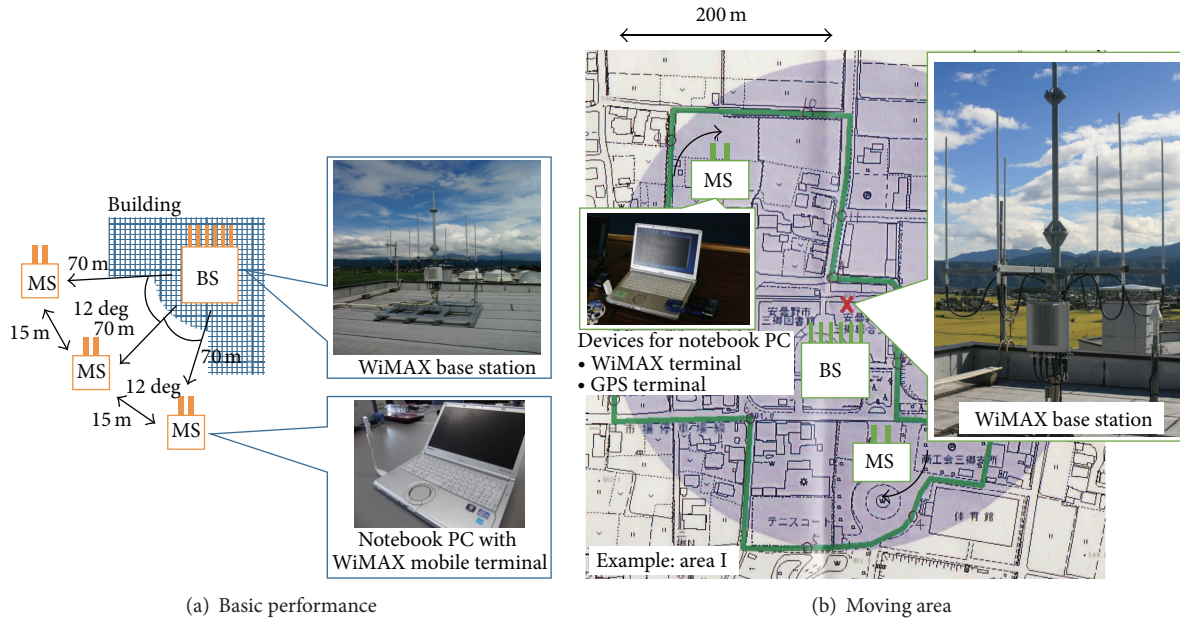


FIGURE 4: Setup for field experiment.

Here, the average $C/(N + I)$ value corresponds to about 15 dB as shown in Figure 3, and the channel capacity becomes depleted because the interference value cannot be eliminated completely if the number of streams is larger than 2. Under this spatially correlated condition, the channel capacity per frequency with 2 streams W_2 and 3 streams W_3 was about 8.0 bps/Hz and 12.1 bps/Hz, respectively. Thus, it was converted to the transmission speed of 27.4 Mbps for 2 streams and 41.4 Mbps for 3 streams. In the field experiment, we used the simulated results of 16.17 Mbps for 1 stream and 27.4 Mbps for 2 streams for the evaluation because the maximum number of streams for the experimental mobile WiMAX system was 2.

4. Field Experiment

4.1. Overview of Experimental Mobile WiMAX System. Figure 4 shows an overview of the experimental mobile WiMAX system constructed in Azumino City in Japan. In the network area of the system, we measured the received power and the throughput performances for MU-MIMO transmission within 200–500 m centering on the BS.

A WiMAX BS complying with IEEE 802.16e was used, and the parameters are listed in Table 1. The frequency was 2587 MHz, which is an open frequency band for local communities, and the bandwidth was 10 MHz and called the “local band.” The frame structure was OFDMA/TDD, and its interval was 5 ms, which was decided by the system profile of the mobile WiMAX. The ground height of the BS was about 17 m. Here, CSI feedback was transmitted from the MSs to the BS by using the codebook algorithm [19].

The number of transmitting antennas at the BS is 6, and the number of receiving antennas at a MS was 2. The number of users was 1-2 because the maximum number of streams in

the WiMAX system with Matrix A/B mode was 2. In Matrix A mode, the maximum number of streams is 1, and the system can obtain the transmitting diversity gain to improve the channel quality. In Matrix A/B mode, the maximum number of streams is 2. The number of streams in Matrix A/B mode is changed into 1 or 2 dynamically, and the system can increase the total channel capacity by using the MU-MIMO technique when the number of streams is 2.

The received power and the throughput of downlink were measured by using a notebook PC. Users each had a notebook PC with a WiMAX terminal device and GPS terminal devices, and the samples of the received power, throughput, and position were measured. The throughput performance in the UDP layer was measured by using the same notebook PC connected to the WiMAX BS directly. The interval getting the samples was 1 second.

In the field experiments, at first, throughput performance is measured under the static and LOS conditions in order to compare the basic performance with MU-MIMO transmission with Matrix A and Matrix A/B modes. An overview of the basic performance is shown in Figure 4(a).

Then, as shown in Figure 4(b), the received power and throughput performance were measured by walking in “Area I” and “Area II.” These areas were within 200 and 500 m from the experimental mobile WiMAX BS, respectively. In them, there were many positions under line-of-sight (LOS) and non-LOS (NLOS) conditions because of buildings and trees. When the number of streams was 1, only 1 user was walked, and samples were measured. When the number of streams was 2, 2 users were walked, and samples were measured at the same time.

4.2. Extension for MU-MIMO from SU-MIMO. To evaluate the basic performance of downlink MU-MIMO transmission based on the experimental mobile WiMAX system, we

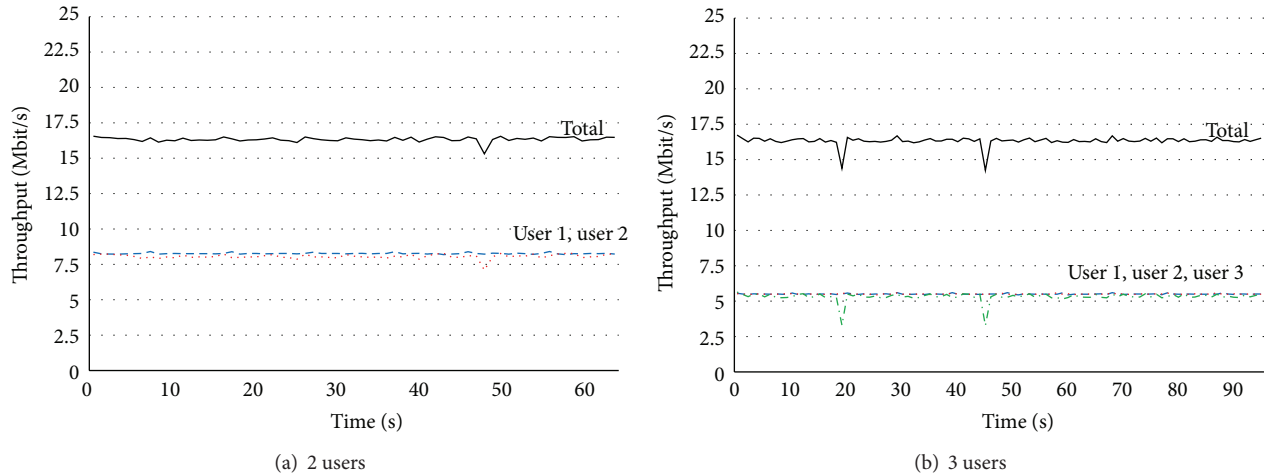


FIGURE 5: Basic throughput performance with Matrix A mode.

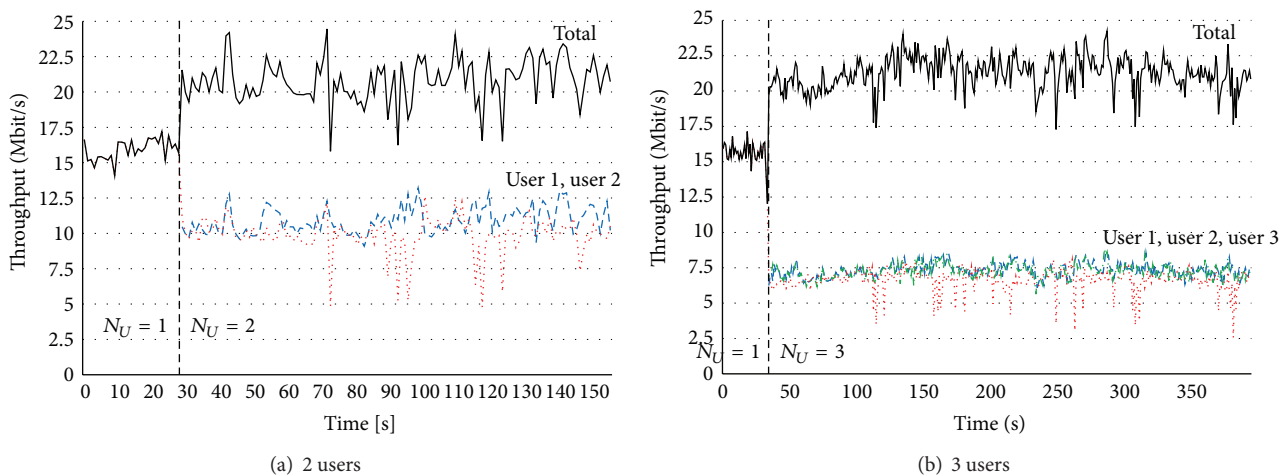


FIGURE 6: Basic throughput performance with Matrix A/B mode.

measured throughput performance with Matrix A and Matrix A/B modes under static and LOS conditions.

Figure 5 shows the measured throughput performance with Matrix A mode, and the numbers of users were 2 in (a) and 3 in (b). From these graphs, the maximum total throughput in (a) and (b) was the same value. Because Matrix A mode can only improve the channel quality, the channel capacity cannot be increased. As shown in (a), the measured throughputs for users 1 and 2 were about 8 Mbps, and the measured total throughput was about 16 Mbps. As shown in (b), the measured throughputs for each user were about 5.3 Mbps. In Matrix A mode, each user can be provided almost the same throughput performance.

Figure 6 shows the measured throughput performance with Matrix A/B mode, and the number of users were 2 in (a) and 3 in (b). Comparing the maximum throughput with Matrix A mode and Matrix A/B mode, the maximum throughput with Matrix A/B mode was higher than that with Matrix A mode. Because Matrix A/B mode can increase the total channel capacity, the channel capacity in accordance with the number of streams can be obtained. In these graphs,

first, the throughput was measured only with 1 user within 30 seconds. After a lapse of 30 seconds, throughputs with 2 and 3 users were measured. The results in Figure 6 also show that the maximum throughput with Matrix A/B mode, whose number of streams was 2, was about 23 Mbps, and the throughputs for each user were almost the same values.

4.3. Received Power Performance. Figure 7 shows both a route map and the received power at each point on the moving route, and Figure 8 shows the result of the measured received power versus the relative frequency in (a) and the cumulative frequency in (b).

In Area I, the maximum received power was about -30 dBm, the minimum was about -70 dBm, and the mode value was about -50 dBm. In Area II, the maximum received power was about -35 dBm, the minimum was about -75 dBm, and the mode value was about -55 dBm. In total area, the mode value was about -55 dBm. The distance between the WiMAX BS and the positions in Area II was longer than that in Area I, so that the received power in Area II was lower than that in Area I. Compared with

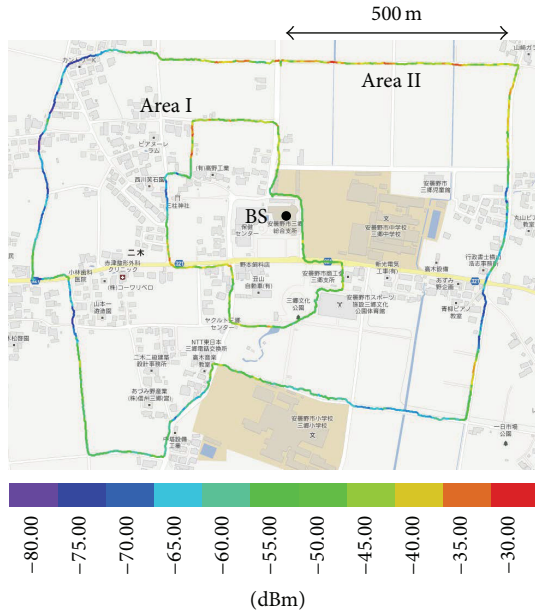


FIGURE 7: Route map and received power at each point.

the CDF of received power in (b), the received powers were -53 , -58 , and -57 dBm when the CDF in Area I, Area II, and the total area became 50%, respectively. The received powers were -58 , -70 , and -68 dBm when the CDF in Area I, Area II, and the total area became 10%, respectively. Moreover, the CDF of received power in Area I was 10 dBm, almost single-digit, decreasing to under -55 dBm, and the CDF of received powers in both Area II and the total area was 10 dBm, almost single-digit, decreasing to under -65 dBm. Therefore, the received and transmitted signals in the total area were under the influence of the fading environment.

4.4. Received Throughput Performance. Figure 9 shows both a route map and the measured throughput at each point on the moving route. Figure 10 shows the result of the measured throughput versus the relative frequency under Area I in (a), Area II in (b), and the total area in (c).

In each graph, “1 stream” denotes the measured throughput with only 1 user and 1 stream. “2 streams” denotes the measured throughput with 2 users and 2 streams, and the throughputs of each user are plotted. “Sum of 2 streams” denotes the sum of the throughputs of 2 users at the same time.

4.4.1. Area I. When the number of streams was 1, the maximum throughput was 13 Mbps, the minimum was 8 Mbps, and the mode value of throughput was 9 Mbps, as shown in Figure 10(a). When the number of streams was 2, the maximum was 12 Mbps, and the minimum was 8 Mbps for each user. The throughputs for each user were distributed similarly. We summarized the throughputs for each user at the same time, and the maximum and the minimum throughputs were 23 and 15 Mbps, respectively.

4.4.2. Area II. When the number of streams was 1, the maximum throughput was 13 Mbps, the minimum was 5 Mbps,

and the mode value of throughput was 8 Mbps, as shown in Figure 10(b). When the number of streams was 2, the maximum throughput was 10 Mbps and the minimum was 4 Mbps for each user. The throughputs for each user were also distributed similarly. The maximum and the minimum throughputs, summarizing the throughputs for each user at the same time, were 18 and 7 Mbps, respectively. Comparing between Areas I and II, the received power in Area II was lower than that in Area I, so that the throughput in Area II was also lower than that in Area I.

4.4.3. Total Area. Finally, Figure 10(c) shows the result in the total area (Area I + Area II). When the number of streams was 1, the maximum throughput was 13 Mbps, the minimum was 5 Mbps, and the mode value of throughput was 9 Mbps. When the number of streams was 2, the throughputs for each user were distributed as the same pattern, and the maximum throughput was 12 Mbps, the minimum was 4 Mbps, and the mode value of throughput was 8 Mbps. The maximum and minimum throughputs, summarizing the throughputs for each user at the same time, were 23 Mbps and 7 Mbps, and the mode value was 16 Mbps.

Note that the downlink maximum throughputs in the physical layer calculated in the above section were 16.2 Mbps and 27.4 Mbps when the numbers of streams were 1 and 2, respectively. The maximum measured throughputs were 13 Mbps and 23 Mbps in the UDP layer; therefore, the throughputs for only 1 and 2 streams were almost the same values as the simulated throughputs in Section 3.3. Furthermore, the MU-MIMO system with 2 streams has twice the throughput performance as compared with that with 1 stream if the system can eliminate interference between signals for the other users perfectly. Although there was some interference between the users, the total throughput performance with 2 streams can be improved by the beamforming in all areas. Therefore, it was confirmed that the MU-MIMO transmission system based on the mobile WiMAX was successfully constructed, and increasing and evaluating the total channel capacity on the system were successfully performed.

5. Discussion

In the computer simulation, we assumed that the transmitter can receive channel information perfectly with CSI feedback from the receivers. However, in the actual field environment, channel information feedback with codebook algorithm [19] was constructed. Such channel information with the codebook algorithm is not perfectly equal compared with the simulated condition. These errors of such feedback CSI cause the interference values between signals for each user, and the sum of throughput performances for 2 users is not equal to twice the throughput for 1 user. The influence caused by the interference should be analyzed in field experiments. For example, the performance of beamforming gains with the experimental WiMAX BS is described and analyzed in [20]. To analyze the interference between the signals for 2 users, beamforming gains should also be measured in the future.

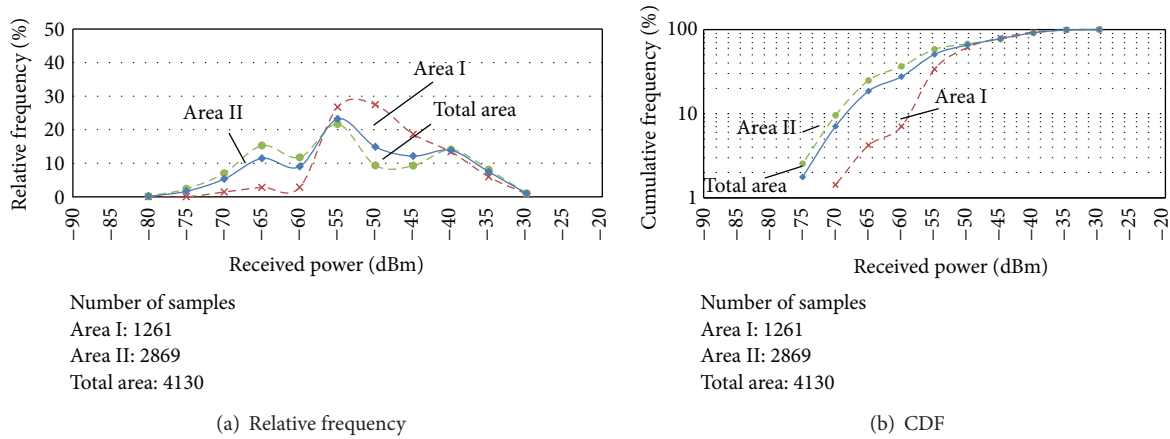


FIGURE 8: Measured received power distribution.

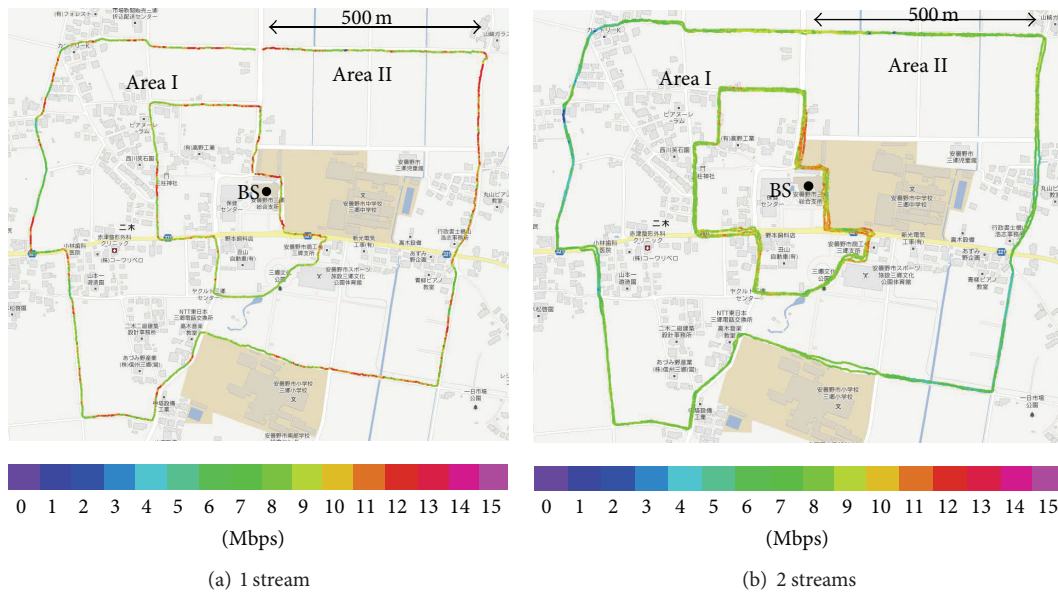


FIGURE 9: Route map and measured throughput at each point.

Although there are few interference values for MU-MIMO transmission with the experimental mobile WiMAX system, the improvement of the total throughput shows that MU-MIMO transmission was realized with the experimental mobile WiMAX system. Furthermore, under spatially correlated multipath fading environments the throughput performance can be preindicated by using the simulated results.

6. Conclusion

We evaluated the transmission performance for a downlink MU-MIMO system by computer simulation and in a field experiment. For the field experiment, an experimental mobile WiMAX system was constructed based on the IEEE 802.16e standard, and the BS had 6 transmitting antennas. The numbers of streams in the computer simulation and field

experiment were 1-3 and 1-2, respectively, and the MSs had 2 receiving antennas for each user. A MU-MIMO system model in the computer simulation was constructed in accordance with the experimental mobile WiMAX system, and MU-MIMO transmission based on the BD algorithm was performed. In the computer simulation, BER performance and channel capacity were analyzed under spatially uncorrelated and correlated multipath fading environments. The results show that the interference values between signals for the other users influenced the BER performance and throughput performance. Furthermore, we proposed a method for evaluating transmission performance for the mobile WiMAX system with MU-MIMO under a spatially correlated multipath fading environment. In the field experiment, the received power and downlink throughput performance were measured by walking around areas. The results show that the maximum downlink throughput with 1 stream was about 13 Mbps and the maximum total throughput with 2 streams

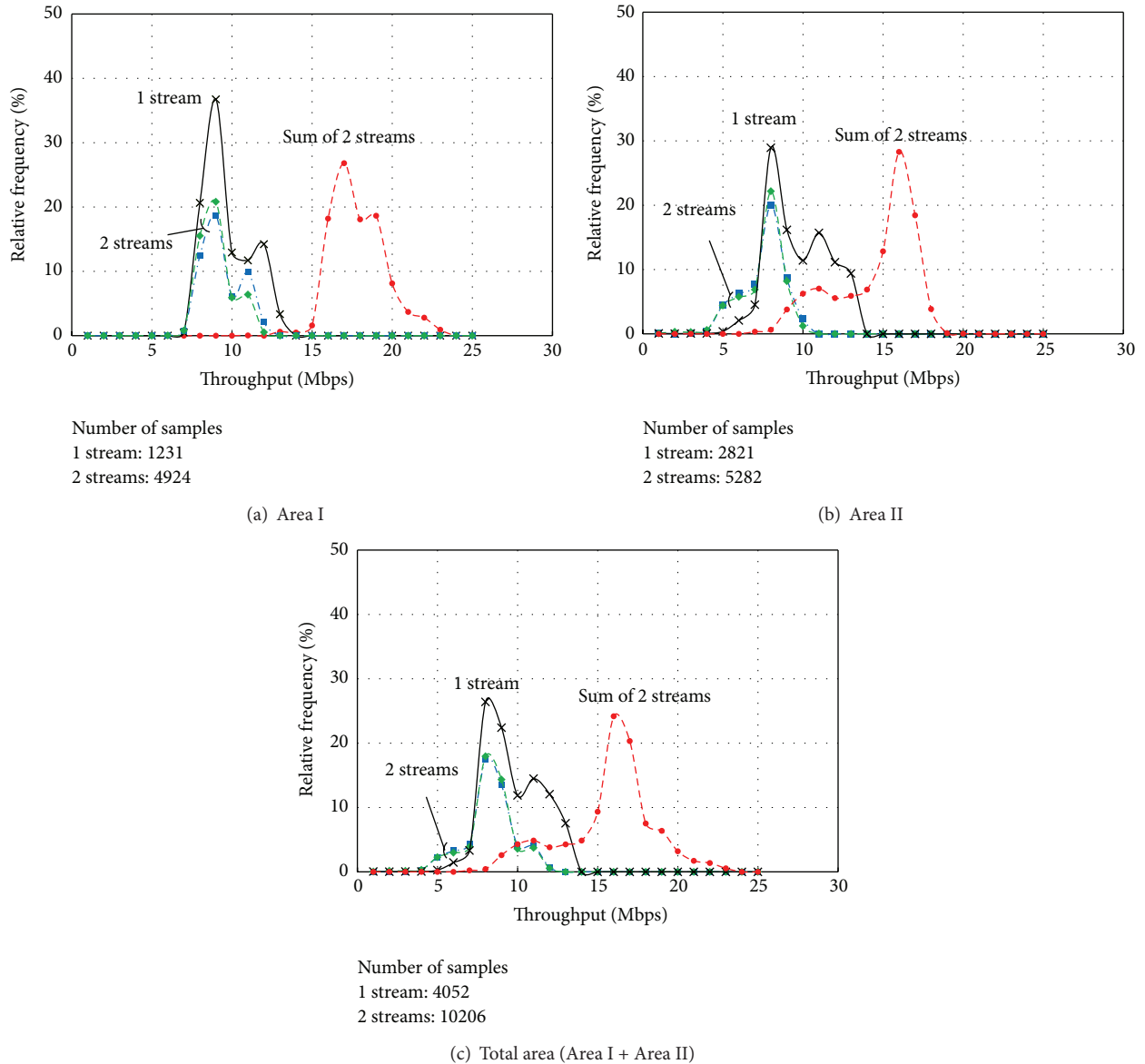


FIGURE 10: Throughput performance distribution in accordance with areas and number of streams.

was about 23 Mbps. Therefore, it was confirmed that MU-MIMO transmission based on mobile WiMAX successfully confirmed increased the total channel capacity of the system. Moreover, the experimental throughput performance could be evaluated correctly by using the proposed evaluation method.

Conflict of Interests

The authors declare that there is no conflict of interests regarding the publication of this paper.

References

[1] A. Goldsmith, *Wireless Communications*, Cambridge University Press, Cambridge, UK, 2005.

[2] G. J. Foschini and M. J. Gans, “On limits of wireless communications in a fading environment when using multiple antennas,” *Wireless Personal Communications*, vol. 6, no. 3, pp. 311–335, 1998.

[3] Q. H. Spencer, C. B. Peel, A. L. Swindlehurst, and M. Haardt, “An introduction to the multi-user MIMO downlink,” *IEEE Communications Magazine*, vol. 42, no. 10, pp. 60–67, 2004.

[4] Y. A. Alqudah and A. Tahat, “Path loss and propagation models at 3.5 GHz using deployed WiMAX network,” in *Proceedings of the International Conference on Information Networking (ICOIN '11)*, pp. 301–305, January 2011.

[5] M. C. Walden and F. J. Rowell, “Urban propagation measurements and statistical path loss model at 3.5 GHz,” in *Proceedings of the IEEE Antennas and Propagation Society International Symposium and USNC/URSI Meeting*, pp. 363–366, July 2005.

- [6] K. Ota, H. Matsue, S. Miyazawa et al., "Field evaluation on mobile WiMAX network and network services in Azumino city," in *Proceedings of the IEEE Region 10 Conference: Sustainable Development Through Humanitarian Technology (TENCON '12)*, Cebu, Philippines, November 2012.
- [7] K. Ota, H. Matsue, S. Miyazawa et al., "Link budget analysis and field experiments on mobile wimax system in azumino city," in *Proceedings of the IEEE Global Telecommunications Conference (GLOBECOM '11)*, pp. 1–5, December 2011.
- [8] IEEE 802.16e-2005 Standard, *IEEE Standard for Local and Metropolitan Area Networks—Part 16: Air Interface for Fixed and Mobile Broadband Wireless Access Systems—Amendment for Physical and Medium Access Control Layers for Combined Fixed and Mobile Operation in Licensed Bands*, 2005.
- [9] K. Yamaguchi, T. Nagahashi, T. Akiyama et al., "Performance evaluation of downlink MU-MIMO transmission based on mobile WiMAX system in computer simulations and field experiments," in *Proceedings of the International Conference on Information and Communication Technology Convergence (ICTC '14)*, pp. 253–258, Busan, Republic of Korea, October 2014.
- [10] T. Nagahashi, K. Miyasaka, T. Akiyama et al., "Throughput performance for field experiments in MU-MIMO systems," *IEICE Technical Reports*, vol. 113, no. 301, RCS2013-174, pp. 1–6, 2013 (Japanese).
- [11] M. H. Costa, "Writing on dirty paper," *IEEE Transactions on Information Theory*, vol. 29, no. 3, pp. 439–441, 1983.
- [12] Q. H. Spencer, A. L. Swindlehurst, and M. Haardt, "Zero-forcing methods for downlink spatial multiplexing in multiuser MIMO channels," *IEEE Transactions on Signal Processing*, vol. 52, no. 2, pp. 461–471, 2004.
- [13] H. P. Bui, Y. Ogawa, T. Nishimura, and T. Ohgane, "Performance evaluation of a multi-user mimo system with prediction of time-varying indoor channels," *IEEE Transactions on Antennas and Propagation*, vol. 61, no. 1, pp. 371–379, 2013.
- [14] K. Miyashita, T. Nishimura, T. Ohgane, Y. Ogawa, Y. Takatori, and K. Cho, "High data-rate transmission with Eigenbeam-space division multiplexing (E-SDM) in a MIMO channel," in *Proceedings of the IEEE 56th Vehicular Technology Conference*, vol. 3, pp. 1302–1306, IEEE, September 2002.
- [15] L.-U. Choi and R. D. Murch, "A transmit preprocessing technique for multiuser MIMO systems using a decomposition approach," *IEEE Transactions on Wireless Communications*, vol. 3, no. 1, pp. 20–24, 2004.
- [16] F. Kaltenberger, D. Gesbert, R. Knopp, and M. Kountouris, "Correlation and capacity of measured multi-user MIMO channels," in *Proceedings of the IEEE 19th International Symposium on Personal, Indoor and Mobile Radio Communications (PIMRC '08)*, pp. 1–5, September 2008.
- [17] M. Chiani, M. Z. Win, and A. Zanella, "On the capacity of spatially correlated MIMO Rayleigh-fading channels," *IEEE Transactions on Information Theory*, vol. 49, no. 10, pp. 2363–2371, 2003.
- [18] D.-S. Shiu, G. J. Foschini, M. J. Gans, and J. M. Kahn, "Fading correlation and its effect on the capacity of multielement antenna systems," *IEEE Transactions on Communications*, vol. 48, no. 3, pp. 502–513, 2000.
- [19] X. Zheng and E. Lindskog, "A simplified channel model for mimo communications with polarization," in *Proceedings of the 43rd Asilomar Conference on Signals, Systems and Computers*, pp. 1407–1411, November 2009.
- [20] V. Desai, J. F. Kepler, and F. W. Vook, "Field data showing the downlink adaptive beamforming gains in an experimental IEEE 802.16e-2005 OFDMA system," in *Proceedings of the IEEE Radio and Wireless Symposium (RWS '08)*, pp. 619–622, January 2008.

Research Article

Calibration of Smartphone-Based Weather Measurements Using Pairwise Gossip

Jane Louie Fresco Zamora, Shigeru Kashihara, and Suguru Yamaguchi

Graduate School of Information Science, Nara Institute of Science and Technology, 8916-5 Takayama, Ikoma, Nara 630-0192, Japan

Correspondence should be addressed to Jane Louie Fresco Zamora; louie-z@is.aist-nara.ac.jp

Received 10 October 2014; Accepted 28 January 2015

Academic Editor: Karim Kabalan

Copyright © 2015 Jane Louie Fresco Zamora et al. This is an open access article distributed under the Creative Commons Attribution License, which permits unrestricted use, distribution, and reproduction in any medium, provided the original work is properly cited.

Accurate and reliable daily global weather reports are necessary for weather forecasting and climate analysis. However, the availability of these reports continues to decline due to the lack of economic support and policies in maintaining ground weather measurement systems from where these reports are obtained. Thus, to mitigate data scarcity, it is required to utilize weather information from existing sensors and built-in smartphone sensors. However, as smartphone usage often varies according to human activity, it is difficult to obtain accurate measurement data. In this paper, we present a heuristic-based pairwise gossip algorithm that will calibrate smartphone-based pressure sensors with respect to fixed weather stations as our referential ground truth. Based on actual measurements, we have verified that smartphone-based readings are unstable when observed during movement. Using our calibration algorithm on actual smartphone-based pressure readings, the updated values were significantly closer to the ground truth values.

1. Introduction

The Intergovernmental Panel on Climate Change (IPCC) reported on extreme changes in climate beginning in the 1950s. Moreover, significant increases in the frequency of heavy precipitation and its intensity were forecasted to occur in this century [1]. With the decline in the number and quality of global weather daily reports [2], this becomes a problem when dealing with rain-related disasters. Examples of these disasters are very strong winds that typically occur before and during the rain, as well as flash flooding and landslides that usually occur during or after the rain has happened. This is especially true for Asia with reported total deaths of 1,005,608 (in thousands) caused by flooding and landslides [3].

To observe rain events or the atmospheric condition in general, meteorologists use weather instruments to measure the temperature, wind, pressure, and humidity of the environment [4]. This observation system is a combination of in situ weather devices, radars, and geostationary satellites monitoring the atmosphere. Recently, the national meteorological services (NMS) employed automatic weather stations for ground observations and weather radars with increased

spatial and temporal resolutions. For example, surface observations by the Japan Meteorological Agency are provided by their Automated Meteorological Data Acquisition System (AMeDAS), which is composed of 1,300 automatic weather stations [5]. These weather stations are sparsely distributed all over the country on an average of 17 km apart. Meanwhile, the USA obtains surface weather information from their Automated Surface Observing System (ASOS), which also reports basic weather elements similar to AMeDAS [6]. Furthermore, the development of phase-array radars is ongoing and a few X-band radars have already been installed in selected prefectures in Japan. These instruments have resolutions of several 100 meters in area and can provide data within the span of seconds to a few minutes. However, the wide use of these sophisticated instruments, especially in developing countries, has yet to materialize.

Additionally, there are emerging private companies that provide weather information as a service. To name a few, they are Weathernews, Inc. (WNI) [7] and the Japan Weather Association (JWA) [8] based in Japan, Weather Underground [9] and Accuweather [10] in the US, and WeatherOnline [11] and MeteoGroup [12] in Europe. A majority of these

companies cater to clients who need customized weather information from sea to land. The resources of these institutions are diverse and wide, which enables them to deliver accurate and prompt information that, however, comes with a cost. WNI, for instance, provides notifications on warnings for localized heavy rains only to individuals who are registered as clients. This particular feature is only available when an individual pays for the required monetary dues. In general, companies and businesses avail of these weather information services for the continuous operation of their enterprise. Thus, only individuals who are willing to pay for the monthly service dues and add-on payments would typically avail of this service.

Considering the need for high resolution surface weather data in forecasting extreme rain-related events, we need to examine low-cost and low-maintenance solutions. The additional installation of high-end weather instruments that are typically used by NMSs would normally depend on the national budget. Also, aside from purchasing these pieces of equipment, the government may also need additional labor to maintain them. As for private weather services, it may not be practical for some individuals especially in developing countries to pay a monthly fee if they only need updates on particular days. They may opt for the free weather service by the government but the information would typically be insufficient and sometimes inaccurate. As a solution, researchers find alternatives in sensor network technologies to observe ground surface weather. SensorScope [13], for example, is a weather station network composed of assembled commercial environmental sensors that are robust and can be deployed in remote areas with low maintenance. Another approach to surface weather observation is by using rain-induced signal attenuation in microwave links to observe and characterize rain events as in [2, 14]. Even with these developments, however, we may need more observation points of high spatial and temporal resolutions especially for understanding heavy precipitation that typically occurs at scales of subkilometer.

A prior work [15] on using distributed devices for surface weather observation suggested the need for a calibration method to effectively and reliably aggregate weather information. As one of the solutions to address the problem of collaborating different types of devices, narrowing the focus to smartphone-based measurements can be a fundamental approach. Thus, analyzing measurements from embedded smartphone sensors would be a better way of obtaining high density synoptic weather information considering that many people currently use smartphones. However, one problem is that a smartphone is not necessarily a fixed sensor and is typically, for instance, kept inside trouser or shirt pockets and bags or held in-hand for sending messages or calling. This could obviously affect the measurement quality if we aim for a continuous long-term data gathering. For example, in most cases, portable environmental sensors like the ones embedded in the smartphones are helpful when the user would like to find out current weather conditions. It is on this instance that the user holds out the device and obtains the instantaneous measurements. Nonetheless, we would like to record the environmental conditions even when the user

does not deliberately perform the measurements. This is so because we try to take advantage of the possibly large amount of data that we could provide to general forecasting services especially for predicting extreme rain-related events. Thus, we propose to utilize smartphones, smartphone-based sensors, and other existing commercial weather sensors to provide additional and high-dense information of surface ground weather to support general forecasting services.

Similar to how weather instruments are calibrated and maintained, however, smartphone-based data should undergo similar data correction processes to yield reliable synoptic weather data. Therefore, in this paper, we investigate how to correct or adjust smartphone-based environmental data even when the device is normally used as a smartphone. Using commercial weather instruments and built-in smartphone sensors, we adjust the device-based measurement with a heuristic-based pairwise gossip algorithm. In our general setup, fixed sensors like the commercial weather stations are assumed to produce proper information and therefore the majority of the adjustments are to be performed on the smartphone-based data. To do so, we consider the basic context-based information such as acceleration to observe user activity and adjust the measured information accordingly.

Quantitative estimation of the current environmental conditions, such as temperature, humidity, and pressure, allows general forecasting services to have an outlook of the weather in the next few minutes partly based on ground surface information. If the estimate is far from actual conditions, this could remarkably affect the calibration with other weather instruments and eventually the forecasting model outputs. Therefore, if we could accordingly adjust the values from the source in reference to a relative ground truth, then we may be able to mitigate forecasting errors from the lowest level of computation. The contribution of this paper is the formulation of a heuristic-based pairwise gossip algorithm that will adjust pressure values as measured by the embedded sensors in the smartphone based on a normal usage. Adjusting the smartphone-based value when the user is stationary or moving requires the reference measurements of a weather station as our established ground truth. In this way, it does not require complex formulations to easily calibrate the pressure sensor on the smartphone.

The rest of the paper is divided into detailed discussions as follows. Section 2 provides a brief background on mobile phone sensing and sensor network calibration. Section 3 discusses our experimentation with embedded smartphone pressure sensors. Section 4 presents the heuristic-based pairwise gossip algorithm that will adjust environmental data accordingly with a fixed weather station. Lastly, Section 5 summarizes the paper and discusses future work.

2. Related Work

When mobile phones with position, motion, and environmental sensors began to be manufactured, it gradually became a recognized device for sensor networks. Examples of such embedded sensors are the accelerometer, gyroscope,

TABLE 1: List of smartphone models used and their available sensors.

Common name	Galaxy Nexus [16]	S3 [17]	S4 [18]
Model	I9250	GT-I9300	GT-I9500
Android OS version	4.3	4.2.2	4.3
Light (lux)	✓	✓	✓
Proximity (cm)	✓	✓	✓
Gyroscope (rad/s)	✓	✓	✓
Accelerometer (m/s ²)	✓	✓	✓
Magnetometer (μ T)	✓	✓	✓
Pressure (hPa)	✓	✓	✓
Temperature ($^{\circ}$ C)	N/A	N/A	✓
Humidity (%)	N/A	N/A	✓

light meter, proximity sensor, magnetometer, pressure, temperature, and humidity sensors [19]. Lane et al. [20] emphasized that the conception of mobile phone sensing (MPS) research field is due to a variety of feasible applications using mobile phone sensors. These applications range between social network services, environmental monitoring, and personal health improvement. A typical example of an MPS application would be user context recognition systems [21] that aim to deliver better services based on user behaviour, for instance. Context includes user activities and interactions with other users or with the environment that is based on the MPS data. More often, to get a general view of a group of users, the data has to be sourced from a multiple group of users having similar qualifying criteria. These criteria are based on categorization of MPS data by statistical methods like mean, median, variance, and so forth, to analyze patterns in the data and group-like patterns accordingly. In addition to context recognition, which frequently makes use of position or motion sensor data, environmental application of MPS as listed in [22] also includes utilizing microphones and cameras to provide audio and image samples of the environment, respectively. Another example of environmental MPS is discussed in [23] where it makes use of the temperature sensor to estimate urban air temperatures. With recent mobile phone models like those in Table 1, it is now possible to observe pressure, ambient temperature, and relative humidity for meteorological applications.

However, “crowdsourced” environmental data is largely affected most especially by how individuals are using their devices when data is taken. Several surveys like [24–26], for instance, reveal that individuals would typically keep the devices inside their shirt or trousers pockets or inside shoulder bags or backpacks. Although these survey results were mainly used for activity recognition, we expect that measurements performed in such instances may offset the ideal measured value and notably affect the accuracy and reliability of environmental analysis. Thus, in [27], it has been emphasized that calibration is important in sensor networks to avoid unreliable measurements. This is typical for environmental sensors which weather forecasts rely on and significant for crowdsourced data affected by several human factors. Furthermore, calibration allows for the identification of errors in the system that may be attributed to offset

faults, gain faults, and drift faults. While calibration is often a difficult task, it can be typically implemented in sensor networks before they are deployed or while they are on deployment. An example of calibration that is performed on sensors in situ is the work on target detection using low-cost sensors as in [28]. The study proposed a calibration algorithm based on feedback control theory and a combination of data fusion and Bayesian detection models to properly identify a target exposed under the sensors. Results from small-scale testbed and simulation using real vehicle detection data have proven that target detection using their algorithm achieved optimal performance. Meanwhile, another approach to calibrating sensor networks is based on a gossip protocol [29]. The goal was to estimate a signal signature based on the collective sensor node values while calibrating the values at the same time. Distributed processing techniques were applied to uncalibrated sensors in the network to correct them and determine the signal pattern. Based on their system model and the gossip-based distributed algorithm, the distributed signature learning and node calibration (D-SLANC) algorithm was derived. This algorithm enables local calibration among sensor nodes and addresses the global estimation problem.

Similarly in this paper, we would like to address faults with the embedded smartphone sensors with high-end commercial weather stations as our relative ground truth. In this way, we may be able to utilize the smartphones as a network of weather instruments that can provide general forecasting services with sufficient synoptic ground weather information for their forecasts. Thus, using analytical techniques of context recognition like in [30, 31] and gossip-based concepts, we would like to investigate the effect of placing the device inside a shoulder bag with some user activity in our aim to correct embedded smartphone sensor measurement at the device level.

3. Investigation of Smartphone Sensor Data as Affected by User Activity

Based on the survey results of mobile phone usage provided in [25], 35% of the respondents put their devices inside a bag. This is greater than both the 30% of respondents who put it inside their trouser pocket and 13% who put it inside the chest pocket. Therefore, considering these statistics, we chose to observe first the effect of placing the device inside a bag using two experiments. Using several models of Samsung smartphones listed in Table 1, we investigate on the pressure data having the sensor common to all devices in the list, while the device is measuring from inside a shoulder bag. Surface pressure is an indication of the changes in atmospheric forces that is helpful for meteorologists to predict what kind of weather we will be experiencing. For now, we simply focus on the pressure readings for the weather measurement since the environmental sensor is most common to some smartphone models which are currently being manufactured. Each device is then installed with an Android application that we developed, which logs the available sensor data for every second. The application, in general, samples

the instantaneous measurement of the embedded smartphone sensors at every second and then continuously logs these values as a CSV file in the internal device storage.

We used two units of the Samsung S3 models and one unit each of the Samsung Galaxy Nexus and S4 models, subjecting four devices overall in both experimental setups. Both experimental setups used the same shoulder bag by the same user to perform the measurements. Motion sensors, such as the gyroscope, accelerometer, and magnetometer, were observed in three dimensions subjective to the device orientation. Meanwhile, environmental sensors like light, proximity, pressure, temperature, and humidity were recorded as is. In both experiments, we refer our readings to high-end commercial weather stations, such as the Vaisala WXT520 [32] to provide us with measurements for our estimation reference. It is important to note that we are using several devices, each of which has a particular margin of error. As for the Vaisala, it has an acceptable error of ± 0.5 hPa considering that it has been calibrated according to standard. The pressure sensor in the smartphones has a maximum absolute error of 4 hPa by the specifications according to [33]. Considering these errors, we cannot directly compare the accuracy of smartphone devices to the Vaisala since each instrument was developed for different purposes. However, we find that the pressure sensors in the smartphones can be proven to be useful if calibrated accordingly and if there is potentially enough data. By sufficient data, this could mean having at least one available smartphone device in a 100-meter unit area.

Generally in our experiments, we measure within 10-meter distance as an example of similar measurement situations. Pressure measurements do not significantly change in several hundred meters horizontally but the change in terrain will. In particular with smartphone devices as point sensors, the reported pressure may not be similar when measured in an elevated area as opposed to flat land within several hundred meters. As for the first experiment, it was conducted to investigate the precision of the barometric readings by smartphones compared with that of the weather station. A bigger picture of this scenario is when a user is idling nearby a fixed weather station and with the device measuring on the background. In the setup shown in Figure 1, the user was required to stand one meter from the reference weather station while carrying the shoulder bag with the devices inside it. A meter away from the weather station minimizes the influence on the instrument. The measurements were performed for three separate afternoons while sampling sensor data for 10 minutes in each event. Studies on context recognition would typically sample for one to a few minutes to get enough dataset. For similar experiments to ours, the duration may vary depending on the desired sample size. In our case, we decided on 10 minutes to get enough samples of both environmental and motion sensors. Also, the reference weather station measures every minute and 10 samples are sufficient to describe the surface pressure. Before determining how precise the smartphone-based pressure readings with that of Vaisala, we first preprocessed the data. As the observations were logged in seconds, we wanted to match the per minute resolution of the weather stations.

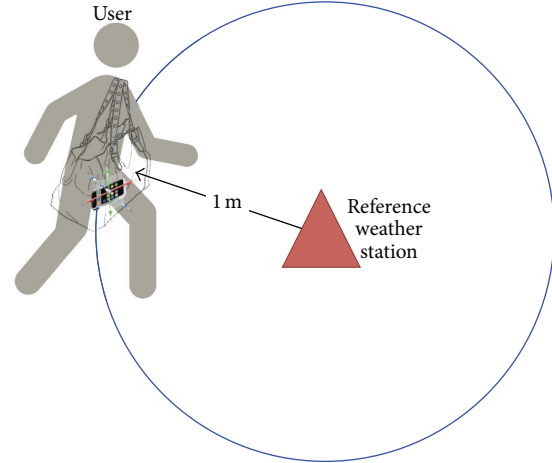


FIGURE 1: Setup of the stationary user experiment.

To do so, we sampled an overlapping window on the same minute (60 units) and determined the median. We use these values of median per minute and implemented them in the following uncertainty range equation α as in

$$\alpha = \left(\overline{X}(t) - x_{\min}(t) \right) + \left(x_{\max}(t) - \overline{X}(t) \right), \quad (1)$$

where $\overline{X}(t)$ is equal to $\sum_{i=1}^n x_i(t) + x_{\text{ref}}(t)$ divided by N for $n = 4$ smartphone devices used and $N = n + 1 = 5$, which includes the reference weather station having a measurement value of $x_{\text{ref}}(t)$. Put simply, it is the average of the barometric pressure values of both smartphone devices and weather station at time t . Then, we determined $x_{\min}(t)$ and $x_{\max}(t)$ by comparing pressure readings from among the 4 devices while excluding the weather station since it is a reference. After comparing the smartphone-based pressure readings, we determine the highest pressure value as $x_{\max}(t)$ and the lowest as $x_{\min}(t)$. In general, determining α can give us a quick and general idea on how much the pressure readings in the smartphone differ with the Vaisala WXT520. Moreover, it is also helpful in knowing how close are the pressure readings among different device models. A sample calculation result can be found at Table 2 based on the sample data in Table 3 where the average uncertainty of smartphone-based sensors for 10 minutes of observed barometric pressure was 2.13. Therefore, in our actual measurements of a stationary user with the devices in the shoulder bag, we can express that the pressure may be approximately ± 2 precise with Vaisala in reference to the sample calculations.

The second experiment, as in Figure 2, was performed to observe the effects of user motion on the pressure readings on the smartphone. As a basic scenario for our proposed system, we imagine a user passing by a reference sensor, which is the kind of user motion that we would like to investigate with this experiment. With the same setup, the user at this time was asked to move around the weather station by walking in a leisurely manner. Each set was composed of 10 rounds, to obtain sufficient sample, that was about 7 minutes long while pausing for 2 minutes in between sets. The movement pattern was designed to estimate the duration of

TABLE 2: Uncertainty calculation results based on the Vaisala WXT520.

Time	$\bar{X}(t)$	$x_{\min}(t)$	$x_{\max}(t)$	Uncertainty
14:00	990.47	989.20	991.28	2.08
14:01	990.44	989.15	991.29	2.14
14:02	990.48	989.19	991.31	2.12
14:03	990.47	989.17	991.34	2.167
14:04	990.41	989.14	991.29	2.15
14:05	990.41	989.15	991.27	2.12
14:06	990.34	989.12	991.24	2.12
14:07	990.35	989.14	991.24	2.10
14:08	990.35	989.12	991.31	2.19
14:09	990.34	989.14	991.24	2.10

TABLE 3: Sample pressure data for uncertainty calculation.

Time	Vaisala	S3(1) \bar{x}	S3(2) \bar{x}	Nexus \bar{x}	S4 \bar{x}
14:00	991.1	991.28	991.14	989.61	989.20
14:01	991.1	991.29	991.13	989.55	989.15
14:02	991.1	991.31	991.2	989.62	989.19
14:03	991.1	991.34	991.13	989.59	989.17
14:04	991	991.29	991.1	989.53	989.14
14:05	991.1	991.27	990.98	989.54	989.15
14:06	991	991.24	990.84	989.49	989.12
14:07	991	991.24	990.79	989.56	989.14
14:08	991	991.31	990.78	989.54	989.12
14:09	991	991.24	990.79	989.51	989.14

the rounds so we can replicate the same duration, which was 7 minutes for each round. The pause was done to compare moving and stationary events and serve as a marker between sets. Figure 3 illustrates the raw readings of pressure and accelerometer data taken from the Samsung S4 device as an example. In the chart, the stages of walking and pauses can be easily distinguished by the instability and stability of the accelerometer readings, respectively.

To closely examine the difference between pressure measurements during the presence or absence of movement, we first divided the raw pressure data into partitions of the corresponding stable and unstable measurements of acceleration. This division is shown in Figure 3, where we have three sets of user movement which correspond to an unstable acceleration and three sets in which the user is not moving which correspond to a stable acceleration. Then, we calculated the variance for each partition and the results are shown in Table 4.

Examining the variance of pressure measured between movement and inactivity can indicate the ability of the sensor to stabilize its readings even when subjected to physical disturbance. Weather stations generally follow a standard for fixed setups to provide accurate and precise readings uniformly without having to consider the effect of movement. However, as we are dealing with portable sensors, this is one aspect that we need to further consider for producing reliable measurements similar to that of fixed weather stations.

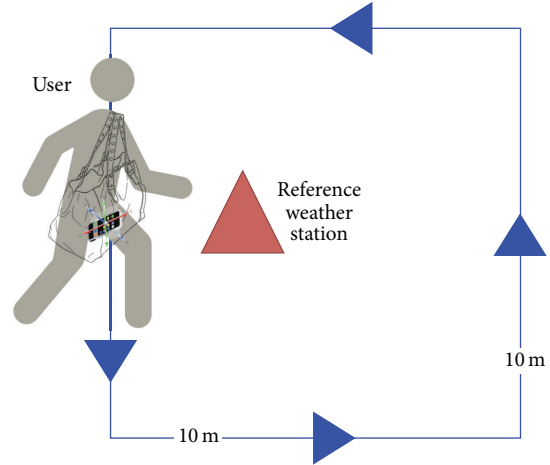


FIGURE 2: Setup of the moving user experiment.

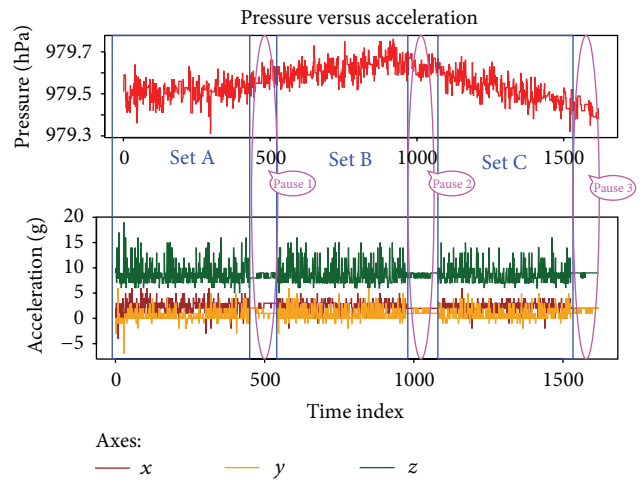


FIGURE 3: Division of moving and stationary partitions each at 7 and 2 minutes, respectively.

TABLE 4: Sample result of calculated variance between partitions of moving and stationary user.

Partition name	Variance
Set A	0.0021
Pause 1	0.0018
Set B	0.0025
Pause 2	0.0013
Set C	0.0032
Pause 3	0.0017

We hypothesize then that the variance of the sensor is higher during movement than when the user is inactive, and thus, we can presume that the sensor is unstable and stable, respectively. To verify this, an upper one-tailed F -test was performed between phases of walking and inactivity as shown in the results of Table 5. The results show that the F value for all comparisons is greater than the F_{critical} values, which rejects the null hypothesis that the variances are equal and

TABLE 5: F -test result for a sample observation.

Partition	F	F_{critical}
Set A versus Pause 1	1.18	0.92
Set B versus Pause 2	1.91	1.49
Set C versus Pause 3	1.82	1.45

proves that the variance of pressure values during movement is higher than when the user is inactive.

Overall, we found that the smartphone pressure sensor reading has an uncertainty value of ± 2 when compared with Vaisala WXT520 from our first experiment. Moreover, we verified via an upper one-tailed F -test that the variance of the smartphone-based pressure readings is higher during user movement than when the user is stationary. Although the pressure readings were not explicitly proven to be accurate in the experiments, this would still imply that the embedded sensor is more stable in providing pressure readings if the user handling the device is stationary as opposed to when the user is moving.

4. Smartphone-Based Sensor Calibration via Pairwise Gossip

Based on our findings on the effect of motion on smartphone sensor readings of pressure, we present our heuristic-based pairwise gossip algorithm. To calibrate embedded smartphone sensors with respect to a fixed weather station, our algorithm relies on the variance of the pressure readings. It is also based on the actual difference of the pressure readings between the smartphone-based sensor and the fixed weather station. Gossip algorithms [34] are generally used for the classic estimation of values in a network by distributed averaging. This particular algorithm has its advantages for distributed averaging in sensor networks as it enables quick and efficient analysis of distributed data over sensor networks especially when faced with several constraints as emphasized in [35]. Such constraints include the lack of centralization, dynamically changing network topology, and sensor hardware limitations. The standard gossip algorithm is in the following form:

$$x(t+1) = W(t)x(t), \quad (2)$$

where $W(t)$ is random weight matrix and $x(t)$ is the current value of a node in a network. Ideally for gossip algorithms, the weights must converge to a value of 1. In actual pairwise gossiping as stated in [34], random pairs of neighboring nodes exchange their information and calculate the average of their values as some time t and update their values with the average, thereafter. In this paper, we apply the same principle of pairwise gossiping by maintaining a one-to-one pairing with the weather station to calibrate the embedded smartphone sensors. However, instead of a random weight assignment, we calculate the weights that equate to a unit value based on the variance of the smartphone-based measurement and the actual difference of the measurements between the smartphone-based sensors and reference weather station.

TABLE 6: Sample raw data from a 10-minute event.

Time	S3(1)	S3(2)	Nexus	S4
14:00:00	991.39	991.11	989.57	989.16
14:00:01	991.35	991.14	989.6	989.16
14:00:02	991.33	991.16	989.58	989.16
\vdots	\vdots	\vdots	\vdots	\vdots
14:09:59	991.23	990.90	989.58	989.14

Let us first consider the following sensing model equation [34]:

$$z_i(t) = H_i\theta + w_i(t), \quad (3)$$

where θ is the value that we want to estimate with our actual pressure readings in the smartphone. In our case, we assign it as our reference value which is the weather station measurement. Meanwhile, H_i and $w_i(t)$ are the gain and offset of the system in place, respectively. Ideally, $H_i = 1$ and $w_i(t) = 0$ are true if, for instance, the embedded pressure sensor in the smartphones behaves similarly to Vaisala. However, in reality, we have the effects of the surrounding environment, user activity, sensor limitations, and so forth. To explain this concept further, we formulate the following heuristics-based pairwise gossip algorithm to adjust and update the pressure readings in the smartphone as in

$$x_i(t+1) = W_\alpha\theta_i(t) + W_\beta x_i(t), \quad (4)$$

where $x_i(t+1)$ is our updated pressure reading ($z_i(t)$ or y). Meanwhile, $W_\alpha\theta_i(t)$ ($H_i\theta$ or mx) is our reference value θ for some ratio of W_α . Finally, $W_\beta x_i(t)$ ($w_i(t)$ or b) is some ratio of W_β based on variance ($\text{Var}(t)$) of $x_i(t)$ and actual difference ($\text{AbsDiff}(t)$) of $x_i(t)$ from θ . The current heuristics algorithm is applicable to a one-to-one calibration of smartphone-based data with a reference weather station. To use the algorithm, the scenario requires that the smartphone is measuring within coverage area of the weather station and consequently located adjacent to the weather station. Thus, (4) presently does not take distance into consideration in the calculation. Furthermore, it follows that $W_\alpha + W_\beta = 1$ considering that the weights ideally converge to one. And as for our heuristics-based pairwise algorithm, since we only need to compare two values every time, we simply assigned $W_\alpha = 1 - W_\beta$, where W_β is the ratio of $\text{Var}(t)/\text{AbsDiff}(t)$. To further understand the process of obtaining W_α and W_β , we will use a dataset of raw barometric pressure logged by all devices used from one of our measured events as in Table 6.

Referring to $S3(1)_{\text{raw}}$ as a more specific example for our calculation process, we first determine the median per minute of the raw pressure readings $S3(1)_{\text{raw}}$. This will produce $S3(1)_{\bar{x}}$ values that are in the similar temporal resolution as the weather station measurements of pressure. Refer to Table 3 for a sample result of these median values per minute for each device. Then, we calculate the variance of the pressure readings of the raw data of each device per minute or $\text{Var}_{S3(1)_{\text{raw}}}(t)$, for example. Next, we obtain the absolute difference of pressure readings between the calculated medians

TABLE 7: S3(1) calculation result of variance and absolute difference.

Time	Vaisala	S3(1) $_{\bar{x}}$	Var(t)	AbsDiff(t)
14:00	991.1	991.28	0.0049859	0.17978
14:01	991.1	991.29	0.0037714	0.19140
14:02	991.1	991.31	0.0037007	0.20952
14:03	991.1	991.34	0.0090520	0.23600
14:04	991	991.29	0.0046557	0.29380
14:05	991.1	991.27	0.0047261	0.16914
14:06	991	991.24	0.0055904	0.23865
14:07	991	991.24	0.0054008	0.23590
14:08	991	991.31	0.0056691	0.31200
14:09	991	991.24	0.0041641	0.24316

TABLE 8: S3(1) calculation result of $W(t)$ and $x_i(t + 1)$.

Time	Vaisala	S3(1)	W_α	$W_\beta = 1 - W_\alpha$	$x_i(t + 1)$
14:00	991.1	991.28	0.027733	0.97227	991.1
14:01	991.1	991.29	0.019704	0.98030	991.1
14:02	991.1	991.31	0.017663	0.98234	991.1
14:03	991.1	991.34	0.038356	0.96164	991.11
14:04	991	991.29	0.015847	0.98415	991
14:05	991.1	991.27	0.027943	0.97206	991.1
14:06	991	991.24	0.023425	0.97657	991.01
14:07	991	991.24	0.022894	0.97711	991.01
14:08	991	991.31	0.018170	0.98183	991.01
14:09	991	991.24	0.017125	0.98287	991

per minute, $\text{AbsDiff}_{\text{Vaisala-S3(1)}_{\bar{x}}}(t)$, for instance, at each device and of the weather station measurements. Refer to Table 7 for the results of Samsung S3 as an example of these calculations.

Then, we consider the effects of the user motion via the variance of the smartphone-based readings and the actual difference of the readings between the smartphone-based sensor and the weather station. We do this by calculating the ratio between $\text{Var}_{(\text{S3(1)})_{\text{raw}}}(t)$ and $\text{AbsDiff}_{\text{Vaisala-S3(1)}_{\text{median}}}(t)$, which we refer to as our W_β . Then, we obtain W_α by $1 - W_\beta$ considering the prior weight condition that requires the weights equal to one. Finally, using these calculated weights, we can update the value of $x_i(t + 1)$ as in Table 8.

The resulting adjustments have significantly transformed the measurements and those measurements are now very close to the reference values as shown in the comparison graph in Figure 4. Each device model essentially has different values of W_α and W_β as reflected in some sample values in Tables 9 and 10, respectively.

In summary, we formulated a heuristic-based pairwise gossip algorithm that adjusts the smartphone measurement values with respect to the weather station measurement. Prior to this, we verified that the variance is higher, for instance, when the user is moving as opposed to when it is stationary. The difference in variance can be linked to the stability and instability of the embedded smartphone sensors. Therefore, to employ this finding, we calculated the weights in accordance with the ratio of the variance of the raw pressure data and the actual difference between the median pressure

TABLE 9: Calculated W_α of different device models.

Time	S3(1)	S3(2)	Nexus	S4
14:00	0.97227	0.84940	0.99894	0.99937
14:01	0.98030	0.81662	0.99896	0.99942
14:02	0.98234	0.93642	0.99852	0.99945
14:03	0.96164	0.85621	0.99615	0.99890
14:04	0.98415	0.95145	0.99813	0.99932
14:05	0.97206	0.92999	0.99847	0.99957
14:06	0.97657	0.97966	0.99752	0.99920
14:07	0.97711	0.97323	0.99998	0.99971
14:08	0.98183	0.98382	0.99859	0.99926
14:09	0.98287	0.96791	0.99768	0.99845

TABLE 10: Calculated W_β of different device models.

Time	S3(1)	S3(2)	Nexus	S4
14:00	0.027733	0.15060	0.0010565	0.00062344
14:01	0.019704	0.18338	0.0010387	0.00057949
14:02	0.017663	0.063578	0.0014766	0.00055123
14:03	0.038356	0.14379	0.0038511	0.0010974
14:04	0.015847	0.048554	0.0018666	0.00067643
14:05	0.027943	0.070009	0.0015258	0.00043013
14:06	0.023425	0.020340	0.0024820	0.00079598
14:07	0.022894	0.026771	0.000017361	0.00029228
14:08	0.018170	0.016183	0.0014091	0.00074171
14:09	0.017125	0.032091	0.0023210	0.0015459

data and the reference weather station values. These weight calculations apply to calibrating embedded smartphone sensors with fixed weather stations as an established ground truth. Moreover, the weights W_α and W_β are not constant over time. In real measurements, therefore, we can calibrate smartphone-based measurements based on the weights even when the user is moving. For instance, in a setup where the user is located within the coverage of a fixed weather station, the established ground truth measurements would most likely have a larger percentage in the calibration. If the ground truth measurements are presumed to be accurate, these values can be representative estimates of the synoptic ground weather condition. Thus, the percentage of the supporting weather information from the smartphone sensor data is dependent on the weights whereby the effect of movement is mitigated via the variance and absolute difference. As a result of a one-to-one fixed setup, the smartphone sensors would be updated with values closer to the representative estimate.

5. Conclusion and Future Work

In this paper, we showed a heuristic-based pairwise gossip algorithm to adjust embedded smartphone pressure sensor measurements. Based on our experiments with the smartphone pressure sensors, we found that the pressure sensors of the different Samsung smartphone models we used have a certain precision value compared with Vaisala WXT520

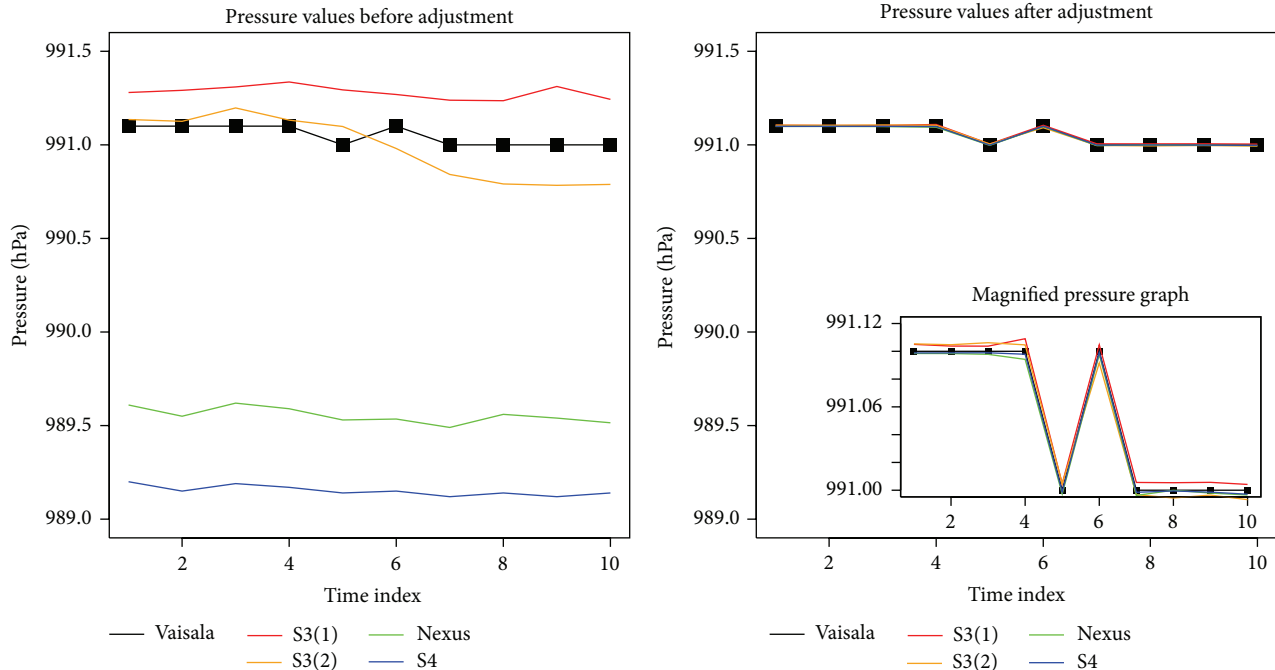


FIGURE 4: Comparison of pressure per minute before and after adjustments.

which we established as our referential ground truth. Moreover, the pressure readings were verified to be unstable when the user is moving compared to when the user is stationary. Thus, to adjust accordingly, we consider the effect of user activity while the device is measuring from inside a shoulder bag by integrating the variance of the raw pressure readings with respect to the actual difference from the reference weather station as our weight ratio. These weight ratios are then consolidated with the pairwise gossip algorithm which updates the pressure reading of the embedded smartphone sensor.

By adjusting the sensor measurements accordingly, we can provide an almost accurate and precise synoptic weather information to general forecasting services. Moreover, as this information can possibly be densely available due to the popular use of smartphones, general weather forecasting services can mitigate errors at the sensor level with this particular calibration method. Thus, this paper contributes a straightforward and heuristic linear estimation using the principles of pairwise gossip. A limitation of this method, however, is that the smartphone requires to be located nearby a weather station at present.

As future work, we plan to extend and update our algorithm to consider scalable and real-time smartphone-based measurements. Consequently, the distance of the mobile device from the reference weather station and from other nearby devices has to be considered and included in the calibration algorithm. Moreover, the method will be improved such that calibration is possible even without a reference weather station. For one device calibrated nearby a reference weather station, all other neighboring smartphone devices can be calibrated in reference to it. The smartphone can then retain the calibration information and may not constantly

need a reference weather station. Also, we may have to consider other environmental sensors like the temperature and humidity and determine if the same algorithm and principles apply.

Conflict of Interests

The authors declare that there is no conflict of interests regarding the publication of this paper.

Acknowledgments

This work is supported in part by NAIST Foundation. The authors would like to thank Professor Takehiko Satomura from Kyoto University for his contribution in their research. The authors also acknowledge Naoya Sawada of the Internet Engineering Laboratory, NAIST, for his contribution to the Android application.

References

- [1] IPCC, *Managing the Risks of Extreme Events and Disasters to Advance Climate Change Adaptation: A Special Report of Working Groups I and II of the Intergovernmental Panel on Climate Change*, edited by C. B. Field, V. Barros, T. F. Stocker, D. Qin, D. J. Dokken, K. L. Ebi, M. D. Mastrandrea, K. J. Mach, G. Plattner, S. K. Allen, M. Tignor, and P. M. Midgely, Cambridge University Press, 2012.
- [2] A. Overeem, H. Leijnse, and R. Uijlenhoet, "Country-wide rainfall maps from cellular communication networks," *Proceedings of the National Academy of Sciences of the United States of America*, vol. 110, no. 8, pp. 2741–2745, 2013.

- [3] IFRC, *World Disasters Report 2013 Focus on Technology and the Future of Humanitarian Action*, edited by P. Vinck, Imprimerie Chirat, Lyon, France, 2013.
- [4] C. Ahrens and P. Samson, *Extreme Weather & Climate*, Brooks Cole Publishing, 2010.
- [5] Japan Meteorological Agency, Observations, 2014, <http://www.jma.go.jp/jma/en/Activities/observations.html>.
- [6] NWS Office of Meteorology, *Automated Surface Observing System (ASOS)*, 1999, <http://www.nws.noaa.gov/ost/asotech.html>.
- [7] Weathernews, Inc., Weathernews, 2014, <http://weathernews.com/>.
- [8] Japan Weather Association, Japan Weather Association, 2014, <http://www.jwa.or.jp/english/>.
- [9] The Weather Channel LLC, Weather Underground, 2014, <http://www.wunderground.com/>.
- [10] Accuweather, Accuweather, 2014, <http://www.accuweather.com/en/world-weather>.
- [11] WeatherOnline Limited, WeatherOnline, 2014, <http://www.weatheronline.co.uk/>.
- [12] Meteogroup, Meteogroup, 2014, <http://www.meteogroup.com/en/gb/home.html>.
- [13] F. Ingelrest, G. Barrenetxea, G. Schaefer, M. Vetterli, O. Couach, and M. Parlange, "Sensorscope: application-specific sensor network for environmental monitoring," *ACM Transactions on Sensor Networks*, vol. 6, no. 2, article 17, 2010.
- [14] H. Messer, A. Zinevich, and P. Alpert, "Environmental sensor networks using existing wireless communication systems for rainfall and wind velocity measurements," *IEEE Instrumentation and Measurement Magazine*, vol. 15, no. 2, pp. 32–38, 2012.
- [15] J. L. Fresco Zamora, N. Sawada, T. Sahara, S. Kashihara, Y. Taenaka, and S. Yamaguchi, "Surface weather observation via distributed devices," in *Proceedings of the IEEE International Instrumentation and Measurement Technology Conference (I2MTC '14)*, pp. 1405–1410, Montevideo, Uruguay, May 2014.
- [16] Samsung, "Samsung GALAXY Nexus," 2014, <http://www.samsung.com/us/mobile/cellphones/SPH-L700ZKASPR>.
- [17] Samsung, "Samsung GALAXY SIII," 2014, <http://www.samsung.com/global/galaxys3/specifications.html>.
- [18] Samsung, "Samsung GALAXY S4," 2014, <http://www.samsung.com/global/microsite/galaxys4/>.
- [19] Android, "Sensors overview," 2014, http://developer.android.com/guide/topics/sensors/sensors_overview.html.
- [20] N. D. Lane, E. Miluzzo, H. Lu, D. Peebles, T. Choudhury, and A. T. Campbell, "A survey of mobile phone sensing," *IEEE Communications Magazine*, vol. 48, no. 9, pp. 140–150, 2010.
- [21] S. A. Hoseini-Tabatabaei, A. Gluhak, and R. Tafazolli, "A survey on smartphone-based systems for opportunistic user context recognition," *ACM Computing Surveys*, vol. 45, no. 3, article 27, 2013.
- [22] C. J. Ferster and N. C. Coops, "A review of earth observation using mobile personal communication devices," *Computers and Geosciences*, vol. 51, pp. 339–349, 2013.
- [23] A. Overeem, J. C. R. Robinson, H. Leijnse, G. J. Steeneveld, B. K. P. Horn, and R. Uijlenhoet, "Crowdsourcing urban air temperatures from smartphone battery temperatures," *Geophysical Research Letters*, vol. 40, no. 15, pp. 4081–4085, 2013.
- [24] F. Ichikawa, J. Chipchase, and R. Grignani, "Where's the phone? A study of mobile phone location in public spaces," in *Proceedings of the IEE Mobility Conference—the 2nd International Conference on Mobile Technology, Applications and Systems*, p. 142, November 2005.
- [25] Y. Kawahara, H. Kurasawa, and H. Morikawa, "Recognizing user context using mobile handsets with acceleration sensors," in *Proceedings of the IEEE International Conference on Portable Information Devices (PORTABLE '07)*, pp. 1–5, Orlando, Fla, USA, May 2007.
- [26] G. Bieber, J. Voskamp, and B. Urban, "Activity recognition for everyday life on mobile phones," in *Universal Access in Human-Computer Interaction. Intelligent and Ubiquitous Interaction Environments*, C. Stephanidis, Ed., vol. 5615 of *Lecture Notes in Computer Science*, pp. 289–296, Springer, Berlin, Germany, 2009.
- [27] K. Ni, N. Ramanathan, M. N. H. Chehade et al., "Sensor network data fault types," *ACM Transactions on Sensor Networks*, vol. 5, no. 3, pp. 1–29, 2009.
- [28] R. Tan, G. Xing, X. Liu, J. Yao, and Z. Yuan, "Adaptive calibration for fusion-based cyber-physical systems," *ACM Transactions on Embedded Computing Systems*, vol. 11, no. 4, article 80, 25 pages, 2012.
- [29] N. Ramakrishnan, E. Ertin, and R. L. Moses, "Gossip-based algorithm for joint signature estimation and node calibration in sensor networks," *IEEE Journal on Selected Topics in Signal Processing*, vol. 5, no. 4, pp. 665–673, 2011.
- [30] D. Figo, P. C. Diniz, D. R. Ferreira, and J. M. P. Cardoso, "Preprocessing techniques for context recognition from accelerometer data," *Personal and Ubiquitous Computing*, vol. 14, no. 7, pp. 645–662, 2010.
- [31] H. Martín, A. M. Bernardos, J. Iglesias, and J. R. Casar, "Activity logging using lightweight classification techniques in mobile devices," *Personal and Ubiquitous Computing*, vol. 17, no. 4, pp. 675–695, 2013.
- [32] Vaisala, "Vaisala Weather Transmitter WXT520 Access to Real Time Weather Data," 2013, <http://www.vaisala.com/en/products/multiweathersensors/Pages/WXT520.aspx>.
- [33] G. Liu, K. M. A. Hossain, M. Iwai et al., "Beyond horizontal location context: measuring elevation using smartphone's barometer," in *Proceedings of the ACM International Joint Conference on Pervasive and Ubiquitous Computing: Adjunct Publication (UbiComp '14)*, pp. 459–468, September 2014.
- [34] A. G. Dimakis, S. Kar, J. M. F. Moura, M. G. Rabbat, and A. Scaglione, "Gossip algorithms for distributed signal processing," *Proceedings of the IEEE*, vol. 98, no. 11, pp. 1847–1864, 2010.
- [35] S. Boyd, A. Ghosh, B. Prabhakar, and D. Shah, "Gossip algorithms: design, analysis and applications," in *Proceedings of the 24th Annual Joint Conference of the IEEE Computer and Communications Societies (INFOCOM '05)*, vol. 3, pp. 1653–1664, March 2005.

Research Article

An Active Learning Approach with Uncertainty, Representativeness, and Diversity

Tianxu He,¹ Shukai Zhang,^{1,2} Jie Xin,^{1,2} Pengpeng Zhao,¹
Jian Wu,¹ Xuefeng Xian,^{1,3} Chunhua Li,¹ and Zhiming Cui^{1,3}

¹ School of Computer Science and Technology, Soochow University, Suzhou 215006, China

² State Key Lab. for Novel Software Technology, Nanjing University, Nanjing 210093, China

³ Suzhou Vocational University, Suzhou 215104, China

Correspondence should be addressed to Zhiming Cui; szzmcai@suda.edu.cn

Received 30 May 2014; Accepted 10 July 2014; Published 11 August 2014

Academic Editor: Juncheng Jia

Copyright © 2014 Tianxu He et al. This is an open access article distributed under the Creative Commons Attribution License, which permits unrestricted use, distribution, and reproduction in any medium, provided the original work is properly cited.

Big data from the Internet of Things may create big challenge for data classification. Most active learning approaches select either uncertain or representative unlabeled instances to query their labels. Although several active learning algorithms have been proposed to combine the two criteria for query selection, they are usually ad hoc in finding unlabeled instances that are both informative and representative and fail to take the diversity of instances into account. We address this challenge by presenting a new active learning framework which considers uncertainty, representativeness, and diversity creation. The proposed approach provides a systematic way for measuring and combining the uncertainty, representativeness, and diversity of an instance. Firstly, use instances' uncertainty and representativeness to constitute the most informative set. Then, use the kernel k -means clustering algorithm to filter the redundant samples and the resulting samples are queried for labels. Extensive experimental results show that the proposed approach outperforms several state-of-the-art active learning approaches.

1. Introduction

According to an IDC report, the global data volume in 2014 has reached 8.7 ZB and will reach 40 ZB. With storage and transmission expanding PB level and EB level, it is indicated that big data will play an important role as important resources. Many supervised learning algorithms have been largely used in classification tasks [1, 2]. For a classification problem, the performance of classifier depends heavily on the labeled sample set. However, obtaining the labeled samples is very difficult while the labeled samples are scarce. In order to reduce the cost of labeling, active learning methods have been adopted to control the labeling process. Active learning is an effective method to solve these problems, which select high information content unlabeled samples to be labeled by experts [3, 4]. Querying the most informative instances is probably the most popular approach for active learning. Therefore, the querying strategy naturally becomes a research hotspot of active learning algorithms.

There are numerous different query strategies that have been used to decide which instances are most informative. The strategies are generally divided into two categories. One is based on uncertainty sampling [5, 6], which considers samples' uncertainty as information content and selects the most uncertain samples for labeling. Although most uncertainty query selection strategies have a wide range of applications and achieve good results in many circumstances, they fail to take information in the large amount of unlabeled instances into account and are prone to query outliers. Another category overcomes the disadvantages of uncertainty sampling and considers the samples' uncertainty and representativeness [7, 8].

In general, heuristic methods have been proposed to balance between the uncertainty and the representativeness of the selected sample. They encourage the selection of cluster centers. However, no measure has been taken to avoid repeating labeling samples in the same cluster. Namely, all methods above did not consider redundancy between

selected samples. Batch mode active learning methods will be affected by this problem. In order to accelerate the learning process, it is necessary to speed up the learning process by selecting more than one sample each iteration. So it needs to examine the diversity of the selected samples. To solve the above problems, we propose a novel active learning strategy that exploits information content measured by uncertainty, representativeness, and diversity of unlabeled instances. Samples selected for labeling are with high uncertainty and representativeness and little redundancy.

Our new query selection measure includes two steps. The first step is acquiring high information content samples set by combining uncertainty sampling and representativeness sampling. For the high informative samples set, we apply diversity sampling to get the final samples for labeling. The combination of the two terms is given in a general weighted product form and we use the kernel k -means clustering algorithm for diversity sampling. We conduct experiments on a few benchmark datasets and present promising results for the proposed active learning approach.

2. Related Work

A typical active learning framework assumes that there is a small set of labeled data L and a large pool U of unlabeled data available. Firstly, L is used to train the classifier C . Then, queries are selectively drawn from the pool, which is usually assumed to be closed. Typically, instances are queried in a greedy approach, according to an information measure used to estimate all instances in the pool, and labels for them are assigned by an expert. These new labeled samples are included into L and the classifier C is retrained. Querying loops continue for some predefined iterations or until a stop criterion is met.

A large number of active learning techniques have been introduced in the literature. Many methods employ an uncertainty sampling principle to select the unlabeled instance they are most hesitant to label. In [5], the most uncertain instance is taken as the one that has the largest entropy value on its probable labels. However, in multiclass problems, the entropy does not often well reflect the uncertainty of the sample. Some may have larger classification uncertainty than the ones whose entropy may be higher. For the above problem, Joshi et al. [6] proposed a more effective active learning sample selection criterion BvSB. This criterion considers the difference between the probability values of the two classes having the highest estimated probability value as a measure of uncertainty, which results in a better performance in practical applications. Another common sampling strategy is based on the reduction of version space, among which query-by-committee (QBC) algorithm is the most popular one. QBC algorithms train a committee of classifiers and choose the instance on which the committee members most disagree [9]. In essence, the QBC is also based on uncertainty sampling. One immediate problem is that these approaches select samples close to the classification boundary in that they only consider uncertainty of samples, which are prone to be outliers. In order to avoid labeling outlier samples,

representativeness sampling is an effective solution and there are some studies for a combination of uncertainty and representative aspects. References [10, 11] employ the unlabeled data by using the prior density as weights for uncertainty measures. A similar framework is proposed in [8], which uses a cosine distance to measure samples' representativeness. Literature [12] proposed an adaptive active learning method and showed better performance. Although different prediction models have been employed in these methods, they all ignore samples' cluster information or diversity information. Therefore these methods have the drawback of repeatedly labeling samples in the same cluster, which has little help for improving accuracy. In this paper, we develop a new active learning method which utilizes uncertainty sampling, representativeness sampling, and diversity sampling.

3. Proposed Approach

In this section, we present a novel active learning method that combines the three sampling criteria. The proposed active learning method has four key components: an uncertainty measure, a representativeness measure, an information content measure, and a diversity measure. We will introduce each of them below.

3.1. Uncertainty Measure. Uncertainty sampling aims to choose the most uncertain instance to label. We employ the best-versus-second-best (BvSB) [6] approach, which considers the difference between the probability values of the two classes having the highest estimated probability value as a measure of uncertainty. Assume that our estimated probability distribution for a certain example is denoted by P . Probability value of the best class guess and the second best guess are, respectively. We obtain the BvSB measure and refer [6] for detained information:

$$\begin{aligned} \text{Uncertainty}(x_i) &= \text{BvSB} = \arg \min_{x_i \in U} (p(y_{\text{Best}} | x_i) - p(y_{\text{Second-Best}} | x_i)). \end{aligned} \quad (1)$$

3.2. Representativeness Measure. As mentioned earlier, uncertainty sampling may suffer from the problem of selecting outlier samples. In order to prevent selecting these samples, representativeness sampling is an effective solution. The representativeness of a sample can be evaluated based on how many samples there are similar to it. So, samples with high representativeness are less likely to be outliers. In this section, we use the Gaussian Process [13] framework to measure the representativeness information between the current sample and the remaining unlabeled sample set.

Similar to the literature [12], we define representativeness measure for a candidate sample x_i as follows:

$$\text{Rep}(x_i) = H(x_i) - H(x_i | U_{x_i}), \quad (2)$$

where U_{x_i} denotes the set of unlabeled instances after removing x_i from U and $H(x_i)$ and $H(x_i | U_{x_i})$, respectively, represent entropies of x_i and the remaining unlabeled samples.

```

Input: labeled data set  $L$  unlabeled data set  $U$ 
Repeat
  Training on  $L$  to get the probabilistic classification model  $C$ 
  for each  $x_i$  in  $U$ 
    Use (1) to measure the uncertainty of sample  $x_i$ 
    Use (2) to measure the representativeness of sample  $x_i$ 
    Use (3) to measure the information content of sample  $x_i$ 
  end for
  Select the high information content set  $S$ ;
  Apply kernel  $k$ -means clustering algorithm to  $S$ ;
  Select  $k$  centers  $S_k$  from each of the clusters;
  Query true labels  $Y_k$  of the  $k$  selected samples;
   $L = L \cup \langle S_k, Y_k \rangle$ 
   $U = U \setminus \langle S_k, Y_k \rangle$ 
Output: final high-performance classifier  $C$ .
    
```

ALGORITHM 1: Incorporating uncertainty, representativeness, and diversity for active learning.

A Gaussian Process is a joint distribution over a set of random variables and the marginal distribution over any finite subset of variables is multivariate Gaussian. So we compute the entropy terms with it. For our issue, each instance is associated with a random variable. A symmetric kernel function $K(\cdot, \cdot)$ is then used to produce the covariance matrix, such that

$$\sum_{ii} = K(x_i, x_i), \tag{3}$$

$$\sum_{U_i U_i} = \begin{pmatrix} K(x_1, x_1) & K(x_1, x_2) & \cdots & K(x_1, x_n) \\ K(x_2, x_1) & K(x_2, x_2) & \cdots & K(x_2, x_n) \\ \vdots & \vdots & \ddots & \vdots \\ K(x_n, x_1) & K(x_n, x_2) & \cdots & K(x_n, x_n) \end{pmatrix}, \tag{4}$$

where the covariance matrix $\sum_{U_i U_i}$ is actually a kernel matrix defined over all the unlabeled instances and we assume $U_i = \{1, 2, \dots, n\}$.

According to the property of multivariate Gaussian distribution, we can know that

$$\sum_{i|U_i}^2 = \sum_{ii}^2 - \sum_{iU_i}^{-1} \sum_{U_i i} \tag{5}$$

Closed-form solutions exist for the entropy terms such that

$$H(x_i) = \frac{1}{2} \ln \left(2\pi e \sum_{ii} \right), \tag{6}$$

$$H(x_i | U_{x_i}) = \frac{1}{2} \ln \left(2\pi e \sum_{i|U_i} \right).$$

Using (6), the representativeness definition can finally be in the following form:

$$\text{Rep}(x_i) = \frac{1}{2} \ln \left(\frac{\sum_{ii}}{\sum_{i|U_i}} \right). \tag{7}$$

3.3. Information Content Measure. Given the uncertainty measure and the representativeness measure defined above, we seek to combine the strengths of both. The main idea is to pick samples that are not only with high uncertainty but also with high representativeness. We use the combination value of the two measures as information content value. The higher the combination value is, the higher the information content of corresponding sample is.

Specifically, we propose to combine the two values in a general product form and the information content of sample x_i is as follows:

$$\text{Infor}(x_i) = \alpha * \text{Uncertainty}(x_i) * \text{Rep}(x_i), \tag{8}$$

where α is a tradeoff controlling parameter over the two terms. Samples with high $\text{Infor}(x_i)$ value are more likely to be selected for labeling.

3.4. Diversity Measure. As we know, the high information content set may contain samples in the same cluster. In order to avoid selecting superfluous samples, we apply the kernel k -means clustering algorithm to cluster samples with high information content. We get the k clusters C_1, C_2, \dots, C_k .

Then we choose the k cluster centers $S_k = \{x_{C_1}, x_{C_2}, \dots, x_{C_k}\}$ for labeling, which can effectively guarantee that samples for labeling are with high information content and little redundancy.

First we consider representativeness and diversity criteria at the same time and get the high information content set S . Furthermore, diversity sampling is considered and redundant samples are filtered. So we cluster the samples in the high information content set and choose the clustering center of each cluster into a batch for labeling.

The overall framework of our active learning algorithm is given in Algorithm 1.

TABLE 1: Dataset properties and the corresponding sizes used.

Dataset	Classes	Features	Initial set size	Unlabeled set size	Test set size
USPS	10	256	30	5000	2000
Letters	26	16	30	5000	3000
Pendigits	10	16	30	7000	3498

TABLE 2: Cluster number for each dataset.

Dataset	Labeled numbers at each round
USPS	10
Pendigits	10
Letters	26

4. Experimental Results

In order to evaluate the effectiveness of our proposed approach described in previous sections, we demonstrate results on three UCI datasets: the Letter Recognition Data Set, USPS: optical recognition of handwritten digits originally from the US Postal Service, and Pendigits: pen-based recognition of handwritten digits. The chosen datasets and their properties are summarized in Table 1 along with initial samples set, unlabeled samples set, and test set sizes used in our experiments.

The experiments are conducted to compare the proposed active learning approach to a number of active learning methods, including (1) BvSB [6], which is the uncertainty sampling method, and (2) information density (ID), which denotes the active learning method in [8] that uses the cosine distance to measure an information density and selects uncertain and representative instances.

LibSVM is employed to train the train a SVM classifier for all these approaches, and it provides probabilistic predictions over the class labels.

4.1. Size of k for Each Dataset. Table 2 shows the number of cluster for each dataset. Note that class numbers of each dataset have already been known in advance. Then, we adjust the k parameter according to the class number of each dataset to cluster current high information content samples set.

4.2. Classification Accuracy on Three Datasets. In Figure 1, we show results on the USPS dataset, a dataset consisting of handwritten digits from the US Postal Service. At each active learning round, we select 10 samples for labeling. At early iterations, performances of all methods are similar. As the number of labeled samples increases, our method gradually dominates the other two approaches and the proposed approach selects the most useful samples.

This difference between the three active selection methods becomes more clearly when we look at the results on the Letters dataset. Similar to USPS dataset, we select 10 samples for labeling. We can know that, for achieving the same value

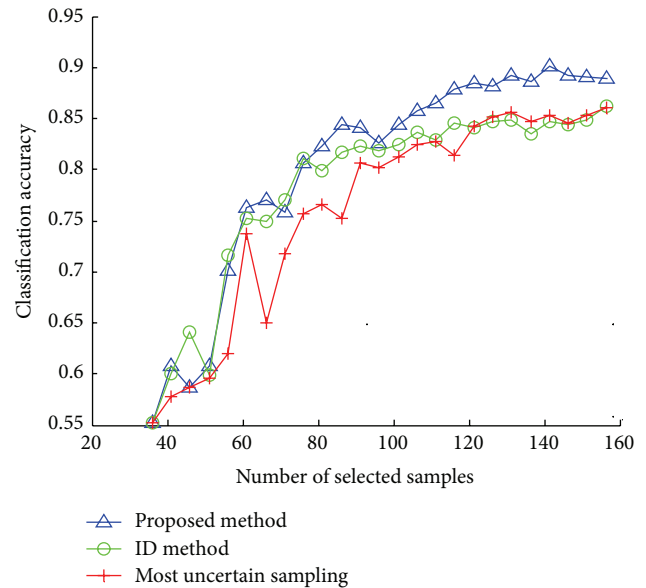


FIGURE 1: Results on USPS dataset.

of classification accuracy on the test data, our method needs far fewer training samples than the other two approaches. Note that ID method does marginally better than most uncertain sampling. The difference can be attributed to the fact that ID method combines uncertainty and representativeness of samples while most uncertain sampling only considers uncertainty of samples.

Figure 3 shows classification accuracy plots on the Letters dataset, which has 26 classes. Most uncertain sampling and ID method perform even worse on this problem due to the larger number of classes. They give a bad indicator of information content of unlabeled samples in this case, and they give comparable poor performance. Even with a larger number of classes, the figure indicates that our approach outperforms other active selection methods.

4.3. Comparison of Diversity. All the results show that our approach in selecting diversity samples is very effective, especially in Pendigits dataset (see Figure 2). From Figures 4 and 5, our method selects samples included in all classes while the other two methods only choose samples with uncertainty or representativeness which is distributed in only a part of classes. Therefore, the proposed method performs better than other methods in most cases.

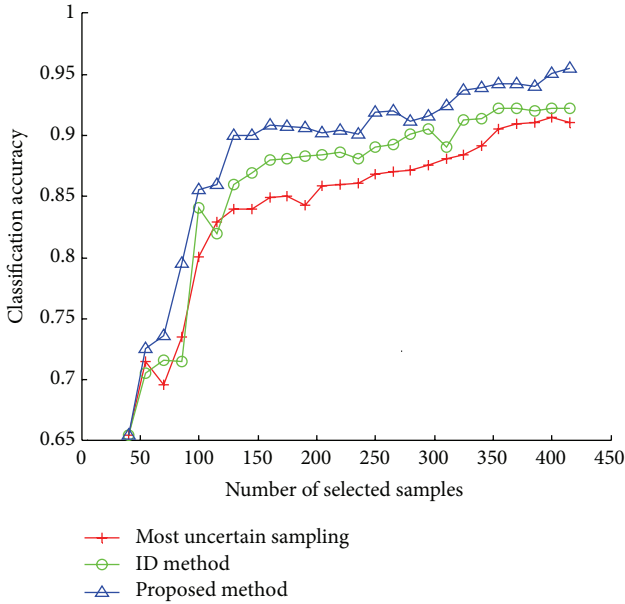


FIGURE 2: Results on Pendigits dataset.

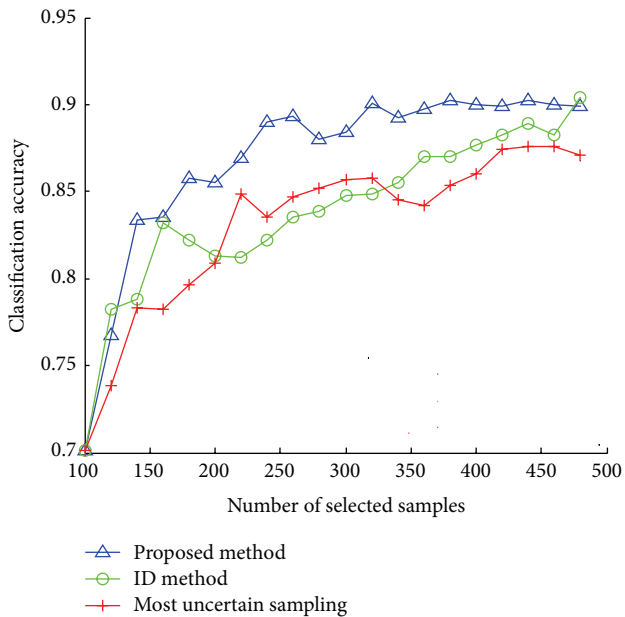


FIGURE 3: Results on Letters dataset.

5. Conclusion and Future Work

In this paper, we presented a novel adaptive active learning approach which combines uncertainty measure and representativeness measure with diversity measure together to conduct samples selection. The proposed method can select samples with high information content and little redundancy. Experiments on multiple datasets show advantages of our approach. The expert in our approach is assumed to be accurate, indefatigable (always answers the queries), and insensitive to costs. Labeling an optimal utility subset is still costly and expensive in many cases. Crowdsourcing labelers,

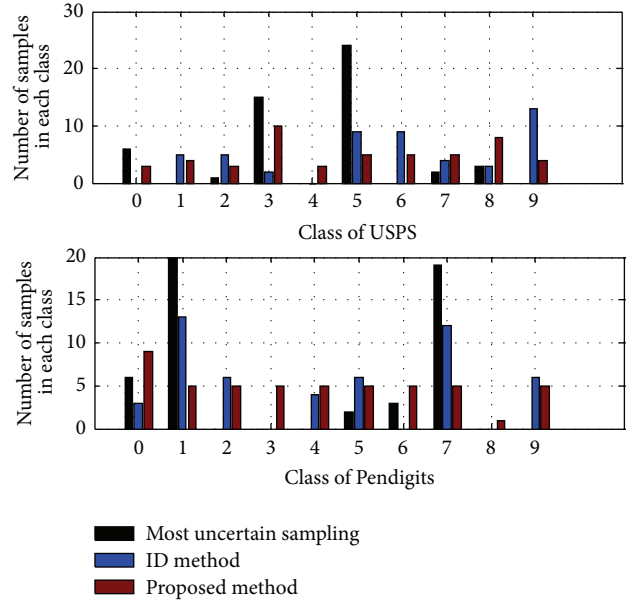


FIGURE 4: Comparison of diversity on 10 classes.

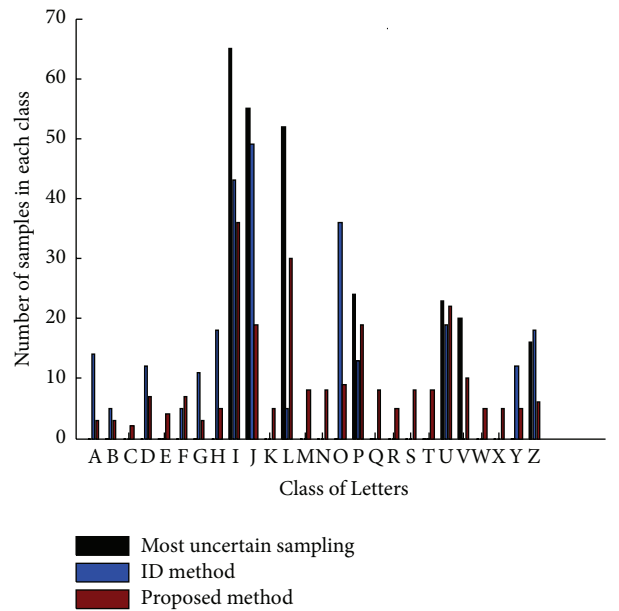


FIGURE 5: Comparison of diversity on 26 classes.

which are composed of some cheap and noisy labelers, have now been considered for active learning. Future work will extend to reduce the cost of this issue.

Conflict of Interests

The authors declare that there is no conflict of interests regarding the publication of this paper.

Acknowledgments

This work is supported by the Natural Science Foundation of Jiangsu Province under Grant no. BK2011376, The Opening Project of Suzhou High-Tech Key Laboratory of Cloud Computing & Intelligent Information Processing no. SXZ201302, Science and Technology Support Program of Suzhou no. SG201257, Science and Technology Support Program of Jiangsu Province no. BE2012075, Suzhou Key Laboratory of Converged Communication (no. SKLCC2013XX), The Opening Project of Suzhou High-Tech Key Laboratory of Cloud Computing & Intelligent Information Processing no. SXZ201302, Provincial Key Laboratory for Computer Information Processing Technology (no. KJS1329), Open Fund of Jiangsu Province Software Engineering R&D Center no. SX201205, and Jiangsu College Graduate Research and Innovation Plan no. CXLX12_0810. This work is also supported by the National Natural Science Foundation of China under Grants nos. 61070169, 61003054, and 61170020 and Jiangsu Province Colleges and Universities Natural Science Research Project under Grant no. 13KJB520021.

References

- [1] A. Prest, C. Schmid, and V. Ferrari, "Weakly supervised learning of interactions between humans and objects," *IEEE Transactions on Pattern Analysis and Machine Intelligence*, vol. 34, no. 3, pp. 601–614, 2012.
- [2] D. Tuia, M. Volpi, L. Copa, M. Kanevski, and J. Muñoz-Mari, "A survey of active learning algorithms for supervised remote sensing image classification," *IEEE Journal on Selected Topics in Signal Processing*, vol. 5, no. 3, pp. 606–617, 2011.
- [3] B. Settles, "Active learning literature survey," *University of Wisconsin, Madison*, vol. 52, pp. 55–66, 2010.
- [4] Y. Fu, X. Zhu, and B. Li, "A survey on instance selection for active learning," *Knowledge and Information Systems*, vol. 35, no. 2, pp. 249–283, 2013.
- [5] A. Holub, P. Perona, and M. C. Burl, "Entropy-based active learning for object recognition," in *Proceedings of the IEEE Computer Society Conference on Computer Vision and Pattern Recognition Workshops (CVPRW '08)*, pp. 1–8, Anchorage, Alaska, USA, June 2008.
- [6] A. J. Joshi, F. Porikli, and N. Papanikolopoulos, "Multi-class active learning for image classification," in *Proceedings of the IEEE Computer Society Conference on Computer Vision and Pattern Recognition Workshops*, pp. 2372–2379, June 2009.
- [7] Z. Xu, R. Akella, and Y. Zhang, "Incorporating diversity and density in active learning for relevance feedback," in *Advances in Information Retrieval*, pp. 246–257, Springer, Berlin, Germany, 2007.
- [8] B. Settles and M. Craven, "An analysis of active learning strategies for sequence labeling tasks," in *Proceedings of the Conference on Empirical Methods in Natural Language Processing (EMNLP '08)*, pp. 1070–1079, Association for Computational Linguistics, October 2008.
- [9] S. Majidi and G. Crane, "Committee-based active learning for dependency parsing," in *Research and Advanced Technology for Digital Libraries*, vol. 8092 of *Lecture Notes in Computer Science*, pp. 442–445, Springer, Berlin, Germany, 2013.
- [10] C. Zhang and T. Chen, "An active learning framework for content-based information retrieval," *IEEE Transactions on Multimedia*, vol. 4, no. 2, pp. 260–268, 2002.
- [11] A. McCallum and K. Nigam, "Employing EM in pool-based active learning for text classification," in *Proceedings of the 15th International Conference on Machine Learning*, 1998.
- [12] X. Li and Y. Guo, "Adaptive active learning for image classification," in *Proceedings of the IEEE Conference on Computer Vision and Pattern Recognition (CVPR '13)*, pp. 859–866, Portland, Ore, USA, June 2013.
- [13] A. Kapoor, K. Grauman, R. Urtasun, and T. Darrell, "Active learning with gaussian processes for object categorization," in *Proceeding of the 11th IEEE International Conference on Computer Vision (ICCV '07)*, pp. 1–8, Rio de Janeiro, Brazil, October 2007.

Research Article

Optimization of Self-Directed Target Coverage in Wireless Multimedia Sensor Network

Yang Yang,^{1,2} Yufei Wang,³ Dechang Pi,¹ and Ruchuan Wang³

¹ College of Computer Science and Technology, Nanjing University of Aeronautics and Astronautics, Nanjing, Jiangsu 210016, China

² Department of Information Technology, Nanjing Radio and TV University, Nanjing City Vocational College, Nanjing, Jiangsu 210002, China

³ College of Computer, Nanjing University of Posts and Telecommunications, Nanjing, Jiangsu 210003, China

Correspondence should be addressed to Yang Yang; nj.yangyang@163.com

Received 2 May 2014; Accepted 23 May 2014; Published 30 June 2014

Academic Editor: Shukui Zhang

Copyright © 2014 Yang Yang et al. This is an open access article distributed under the Creative Commons Attribution License, which permits unrestricted use, distribution, and reproduction in any medium, provided the original work is properly cited.

Video and image sensors in wireless multimedia sensor networks (WMSNs) have directed view and limited sensing angle. So the methods to solve target coverage problem for traditional sensor networks, which use circle sensing model, are not suitable for WMSNs. Based on the FoV (field of view) sensing model and FoV disk model proposed, how expected multimedia sensor covers the target is defined by the deflection angle between target and the sensor's current orientation and the distance between target and the sensor. Then target coverage optimization algorithms based on expected coverage value are presented for single-sensor single-target, multisensor single-target, and single-sensor multitargets problems distinguishingly. Selecting the orientation that sensor rotated to cover every target falling in the FoV disk of that sensor for candidate orientations and using genetic algorithm to multisensor multitargets problem, which has NP-complete complexity, then result in the approximated minimum subset of sensors which covers all the targets in networks. Simulation results show the algorithm's performance and the effect of number of targets on the resulting subset.

1. Introduction

Wireless multimedia sensor network (WMSN) [1], an advancing form of wireless sensor network (WSN) [2], is a multihop self-organizing distributed sensing network which is constituted by battery of multimedia sensor nodes with ability of calculation, storage, and wireless communication. Through multimedia sensor in nodes, this advanced network can find, collect, and handle many kinds of media information, such as audio, video, and image, in surrounding environment. Then the multimedia data will be sent to information gathering center by multihop trunking scheme. After data analysis in information gathering center, overall and effective environment monitoring will be accomplished [1, 3].

One of the most important issues in WSN is sensing coverage, which is also measurement for service quality in WSN [4]. In traditional sensor network, the sensor coverage is usually hypothesized as omnidirectional and predefined as a crude round [1]. But, in WMSN, the coverage method is

very different with its traditional sensor network. The nodes in WMSN, such as video and image sensor nodes, catch a directed visual field, named as field of view (FoV) [5]. Usually the hypothesis is that direction of multimedia sensor node is adjustable [6]. When the node is randomly deployed into malicious environment, it can cover the target and the area self-directly through cooperation with neighbor nodes.

In this paper, the coverage expectation value from node to target is delineated through probabilistic models of FoV disk, which is the ground for self-direction wireless multimedia sensor node and better coverage of target. The optimization algorithms for single-node single-target, multinode single-target, and single-node multitarget are given to solve the coverage problem. Also, the self-directed direction of target covered by FoV disk for every node is set as candidate sensor direction. Genetic algorithm is used to discriminate the self-directed coverage optimization in multinode multitarget circumstance and to discover the minimum set of nodes for coverage of all targets.

2. Relevant Work

Coverage issue of randomly deployed sensor node is the hotspot in this field. In traditional WSN, most researches hypothesise that the omnidirectional sensor node which covers area is a circle with its center in node. But, in WMSN, the sensor cover area is usually hypothesized as sector, which is not applicable for traditional coverage algorithm [6, 7]. Coverage issue can be divided into two categories, the area coverage which ensures that the whole area is covered by sensor node and the target coverage which ensures that every interested target in district is covered by at least one sensor node.

New distributed algorithm has been raised after research in self-directed WMSN [6]. This algorithm realizes node optimal sensing direction, minimal node coverage redundancy in sensing field, and maximal multimedia coverage. Directional sensor network deployment with connectivity and coverage guarantee has been considered in recent study [8]. In this study, minimal directional sensor network was deployed to form a connected network covering interested area. For the target coverage in directional sensor network, different priority was assigned to target [7]. Taking into account the distance between the target and node, a problem of target coverage based on priority has been suggested and a minimal node set was tried to be chosen for all targets monitoring.

In target coverage problem of directional sensor network, the direction and rotation of angle in node directional compensation were not considered [9]. Also, for resolving multinode multitarget coverage optimization, a battery of fixed sensing direction was set up for every sensor node, which was related to node angle of sensing [9]. But rotatable self-directed sensor node has 360° sensing direction. In this research, the self-directed direction and angle of rotation are inducted into self-direction process of multimedia sensor network node, which could decrease the adjustment of sensor node to save energy while optimizing target coverage.

3. Network Hypothesis and Multimedia Coverage FoV Model

The network field in our research is two-dimensional Euclidean field with randomly distributed multimedia sensor nodes and a certain number of interested targets, which means that the sensing direction and position of all nodes are random and independent. The same as the hypothesis in recent study [6], the image sensor is equipped with multimedia sensor node to provide FoV with angle value Θ , which could bilaterally rotate to redefine sensing direction in two-dimensional Euclidean area. Simultaneously, it is hypothesized that monitoring target and multimedia sensor node can achieve their position information through lightweight positioning technology of WSN [10]. Also the nodes in network are hypothesized to have same sensing model, which means that they have identical sensing radius and angle. Since the WMSN is self-oriented, the sensor nodes constituting network can regulate their sensing angle, which means that inexpensive multimedia node can rotate around its vertical axis [6].

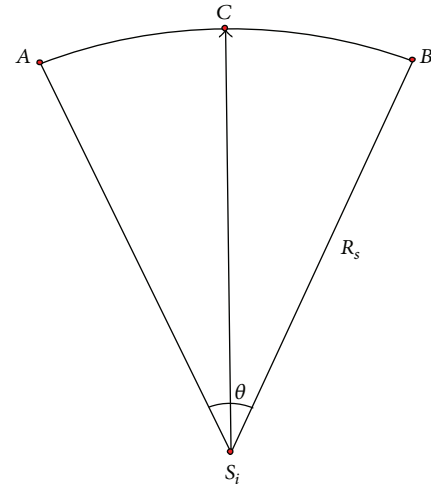


FIGURE 1: 2D FoV sensing model.

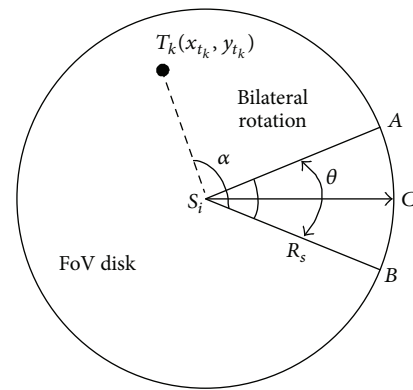


FIGURE 2: FoV disk model.

In a WMSN, $S = \{s_1, s_2, \dots, s_N\}$ is the set of multimedia sensor nodes, R_s is sensing radius of node, and interested target battery is $T = \{t_1, t_2, \dots, t_m\}$. With regard to sensing model of multimedia sensor node, the definition is provided as follows.

Definition 1. 2D FoV: 2D FoV is a directional sensing area of multimedia sensor node, which is hypothesized as a proximate sector in two-dimensional space (Figure 1). 2D FoV of node s_i is defined as tetrad (s_i, R_s, θ, s_iC) , with s_i as sensor, R_s as sensing radius, θ as vertex angle of sector, and s_iC as current sensing direction of node s_i which divide sector into two halves.

Definition 2. 2D FoV disk: the 2D FoV disk of multimedia sensor node is defined as a set of all possible 2D FoV of node, which should be a round area with radius as R_s (Figure 2).

Definition 3. Target coverage of multimedia sensor node $C_{T_k}(s_i)$: equation (1) shows the coverage $C_{T_k}(s_i)$ of node s_i to target T_k :

$$C_{T_k}(s_i) = \begin{cases} 1, & d(s_i, T_k) < R_s, \quad 0 \leq \angle T_k s_i C < \frac{\theta}{2} \\ 0, & \text{other.} \end{cases} \quad (1)$$

```

Input: multimedia sensor node  $s_i$ , interested target  $T_k$ , sensing radius  $R_s$ , FoV vertex angle  $\theta$ , sensing direction  $s_iC$ 
Output:  $C_{T_k}(s_i)$ 

Define Rotate Direction; // rotated direction of node, value as CLOCKWISE or ANTICLOCKWISE
Define Rotate Angle; // rotated angel of node
Calculate  $d(s_i, T_k)$ ; // distance between multimedia sensor node  $s_i$  and interested target  $T_k$ 
IF  $d(s_i, T_k) > R_s$  THEN
     $C_{T_k}(s_i) = 0$ ;
    RETURN  $C_{T_k}(s_i)$ ;
END
IF  $d(s_i, T_k) \leq R_s$  THEN
    Calculate  $\angle T_k s_i C$ ; // the angel between sensing direction  $s_i$  to interested target  $T_k$ 
    IF  $\angle T_k s_i C = 0$  THEN
         $C_{T_k}(s_i) = 1$ ;
        RETURN  $C_{T_k}(s_i)$ ;
    END
    IF  $0 < \angle T_k s_i C \leq \pi$  THEN
        RotateDirection = anticlockwise;
        RotateAngle =  $\angle T_k s_i C$ ;
    END
    IF  $\pi < \angle T_k s_i C < 2\pi$  THEN
        RotateDirection = clockwise;
        RotateAngle =  $2\pi - \angle T_k s_i C$ ;
    END
    ROTATE( $s_i$ , RotateDirection, RotateAngle); //  $s_i$  rotated RotateAngle to RotateDirection
     $C_{T_k}(s_i) = 1$ 
    RETURN  $C_{T_k}(s_i)$ .
    
```

ALGORITHM 1: Single-node single-interested target self-direction coverage algorithm.

If the interested target was located in one FoV disk of some node and not covered by this node in present, there is the possibility that this target could be covered by this node when proceeding with its self-direction. Taking into account decline of monitoring quality followed by increasing distance between interested target and node, along with the deflected angle between the interested target and current sensing direction of node ($\angle T_k s_i C$ as shown in Figure 2), the coverage expectation value of node to interested target is defined.

Definition 4. Expectation value of multimedia sensor node to target $EC_{T_k}(s_i)$: equation (2) shows coverage expectation value of node s_i to target T_k :

$$EC_{T_k}(s_i) = \begin{cases} \lambda \left(1 - \frac{d(s_i, T_k)}{R_s} \right) + \beta \left(1 - \frac{\angle T_k s_i C}{\pi} \right), & d(s_i, T_k) < R_s, \quad 0 \leq \angle T_k s_i C \leq \pi \\ \lambda \left(1 - \frac{d(s_i, T_k)}{R_s} \right) + \beta \left(1 - \frac{2\pi - \angle T_k s_i C}{\pi} \right), & d(s_i, T_k) < R_s, \quad \pi < \angle T_k s_i C < 2\pi \\ 0, & d(s_i, T_k) \geq R_s, \end{cases} \quad (2)$$

where $\angle T_k s_i C$ means current sensing direction to interested target anticlockwise, with value between $[0, 2\pi)$ and parameter $0 \leq \lambda \leq 1, 0 \leq \beta \leq 1$, which defined the adjustable weight of diverted angle and distance between target and node in coverage expectation.

4. Self-Directed Target Coverage Optimization

4.1. Single-Node Single-Target Self-Direction. At first, single-node single interested target coverage, the simplest circumstance, is discussed. The hypothesis is that interested target was located in FoV disk of node but not covered by node, which needs self-directed adjustment to be covered (Algorithm 1). As long as the target was located in FoV disk, it does not need to regard the distance between target and node in single-node single-target self-direction model. The purpose is the minimal rotated angle of node to realize optimal coverage to interested target which is located in s_iC , sensing direction of node.

4.2. Multinode Single-Target Self-Directed Coverage. The problem of multinode single-target self-direction is existence of multiple multimedia sensor nodes. The hypothesis is that interested target is not covered by any node while all nodes can cover the interested target through self-direction. According to the coverage expectation value $EC_{T_k}(s_i)$ of multimedia sensor node to target, the node with maximal

```

Input: set of multimedia sensor nodes  $S$ , interested target  $T_k$ , sensing radius  $R_s$ , FoV vertex
angel  $\theta$ , sensing direction  $SC$  corresponding to node set  $S$ 
Output:  $C_{T_k}(s_i)$ 

Define  $s_i$ ; //node selected to cover interested target,  $s_i \in S$ 
Define RotateDirection; //rotated direction of node, value as CLOCKWISE or ANTICLOCKWISE
Define RotateAngle; //rotated angel of node
Let  $B = \emptyset$ ; //for node set of FoV disk coverage target  $T_k$ 
Let  $EC_{T_k} = \emptyset$ ; //for coverage expectation of node to interested target in  $B$ ;
FOR each  $s \in S$ 
    Calculate  $d(s, T_k)$ 
    IF  $d(s, T_k) \leq R_s$  THEN
         $B = B \cup \{s\}$ ;
        Calculate  $\angle T_k s C$ 
        Calculate  $EC_{T_k}(s)$ 
         $EC_{T_k} = EC_{T_k} \cup \{EC_{T_k}(s)\}$ ;
    END
END
 $EC_{T_k}(s_i) = \text{MAX}(EC_{T_k})$ ;
 $s_i = B[i]$ ;
IF  $0 < \angle T_k s_i C \leq \pi$  THEN
    RotateDirection = anticlockwise;
    RotateAngle =  $\angle T_k s_i C$ ;
END
IF  $\pi < \angle T_k s_i C < 2\pi$  THEN
    RotateDirection = clockwise;
    RotateAngle =  $2\pi - \angle T_k s_i C$ ;
END
ROTATE( $s_i$ , RotateDirection, RotateAngle); //  $s_i$  rotated RotateAngle to RotateDirection
 $C_{T_k}(s_i) = 1$ 
RETURN  $C_{T_k}(s_i)$ .

```

ALGORITHM 2: The algorithm of multinode single-target self-directed coverage.

coverage expectation value is chosen to proceed with self-direction and cover interested target, which is located in sensing direction of node, in optimal angle. The distance between interested target and node and the angel adjusted during self-direction must be considered (see Algorithm 2).

4.3. Single-Node Multitarget Self-Directed Optimal Coverage.

The problem of single-node multitarget direction is how to cover maximal interested targets in node self-direction in the circumstance of multiple interested targets randomly located in FoV disk of some node (see Algorithm 3). The central idea of the algorithm is how to select the interested target subset, which is the maximal subset of the difference between any two targets deflection angles less than or equal to FoV vertex angle, as the target of node self-directed coverage optimization when measured by deflection angle of interested target to node current sensing direction.

4.4. Multinode Multitarget Self-Directed Coverage Optimization. The problem of multinode multitarget self-directed coverage optimization in WMSN is how to find the minimal node set S' covering a definite interested target set T after self-direction. According to coverage corresponding relationship

after optimization, the self-direction is proceeded to cover the target node. For expediently showing the self-direction (direction and angle of rotation) of every node, the variance is introduced.

Node s_i rotates to direction j in angle of Q , 1 as clockwise, 0 as anticlockwise, or 0

The multinode multitarget self-directed coverage optimization can be described as follows:

$$\text{Minimize } |S'| \quad (3)$$

$$\text{Subject to } t \in S', \quad \forall t \in T, S' \subseteq S \quad (4)$$

$$\sum_{j=0,1} \sum_{0 \leq \theta \leq \pi} \text{ROTATE}_{ij\theta} \leq 1, \quad \forall s_i \in S', \quad (5)$$

where $t \in S'$ is t falling in $\bigcup_{s_i \in S'} \text{FoV}$ After Rotate_{s_i} , which means that interested target t is covered after node set S' self-direction. Objective function (3) is minimal subset of multimedia sensor node which can cover all targets after self-direction. Objective function (4) is reciprocal value of coverage expectation for minimal node subset to all targets. Restrictive condition (5) promises that every interested target can be covered by node set S' after self-direction. Restrictive

```

Input: multimedia sensor node  $s_i$ , interested target set  $T$ , sensing radius  $R_s$ , FoV vertex angel  $\theta$ , sensing direction  $s_iC$ 
Output:  $C_{TSET}(s_i)$ , TSET as covered goal set after node self-direction optimization

Define RotateDirection; // rotated direction of node, value as CLOCKWISE or ANTICLOCKWISE
Define RotateAngle; // rotated angel of node
Const  $N$ ; //number of interested target
Let TSC =  $\emptyset$ ; // for angel between node sensing direction to all targets in target set  $T$ 
Let CHA [ $N$ ] [ $N$ ] = {0}; // two-dimensional array, for difference among elements in some limit or not.
Let TSET =  $\emptyset$ ;
FOR each  $T_k \in T$ 
    Calculate  $\angle T_k s_i C$ ; // angel between sensing direction  $s_i$  to interested target  $T_k$ 
    TSC = TSC  $\cup$   $\{\angle T_k s_i C\}$ 
END
 $\vartheta$ ;
Sorting TSC from minimal to maximal;
Calculate the difference absolute value between every two elements in TSC. If the difference
absolute value less than or equal to  $\theta$ , then set CHA corresponding element as 1;
All elements, which numerical of every line is 1 in top triangle of Matrix CHA, constitute the set
with absolute value less than or equal to  $\theta$ ;
Chose the line with maximal numerical equal to 1 in top triangle of Matrix CHA and put
corresponding nodes into set TSET;
Form subset TSETTSC corresponding to set TSC based on the covered target set TSET;
Calculate the mean of maximum and minimum in TSETTSC and recorded as  $\vartheta$ 
IF  $0 < \vartheta \leq \pi$  THEN
    RotateDirection = anticlockwise;
    RotateAngle =  $\vartheta$ ;
END
IF  $\pi < \vartheta < 2\pi$  THEN
    RotateDirection = clockwise;
    RotateAngle =  $2\pi - \vartheta$ ;
END
ROTATE( $s_i$ , RotateDirection, RotateAngle);
 $C_{TSET}(s_i) = 1$ ;
RETURN  $C_{TSET}(s_i)$  TSET
    
```

ALGORITHM 3: Algorithm of single-node multi-interested target self-direction optimal coverage.

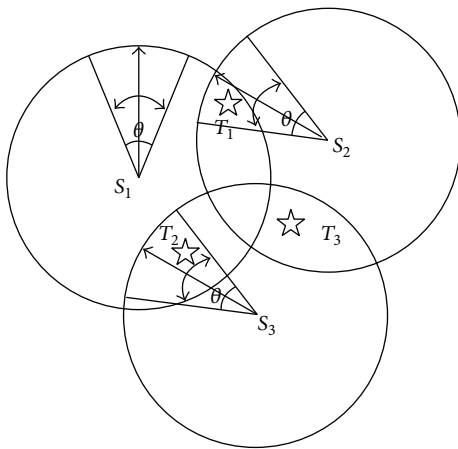


FIGURE 3: A trinode tri-interested target multimedia sensor network.

condition (5) promises that every sensor node $s_i \in S'$ can only rotate to one direction at a given angle at any time.

To be described more vividly, a dilatation figure of multinode multitarget self-directed coverage optimization based on simple example in Figure 3 is shown in Figure 4. In literate [11, 12], the potential sensing direction of every node is fixed. But, in this algorithm, every node can define its potential sensing direction according to node covered by its FoV disk, which is named as self-direction. The top of figure includes multimedia sensor node, self-direction action, and interested target. The left side column represents node set S . The middle column is self-direction action when every node is covering interested target in its own FoV disk. The right column is interested target set T . Every multimedia sensor node S_i is connected with its own self-direction action. Every node can only choose one side because every multimedia sensor node can only do one self-direction action at one time. Every interested target connects with corresponding self-direction action, which means some node can cover this target after self-direction.

Genetic algorithm is used. According to the methods used in [11, 13], the random algorithm in Algorithm 4 is used at first to generate initiate population. It means to generate all

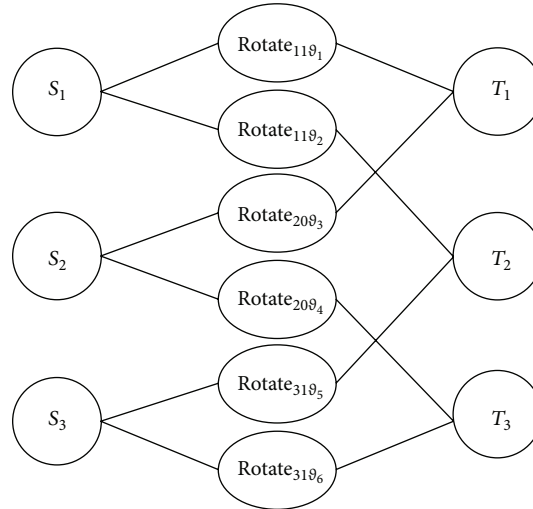


FIGURE 4: Dilatation figure of Figure 3.

```

Input: dilatation G
Output: subset of self-direction action(ROTATE)

randomly chose a self-direction action for every node and denote it as W;
Let  $W' = \emptyset$ ;
WHILE(every target  $T_i \in T$  is covered by self-direction action in W)
  Randomly chose a self-direction action Rotate  $\in W$ 
   $W' = W$ ;
   $W = W - \{\text{Rotate}\}$ ;
END
RETURN  $W'$ 

```

ALGORITHM 4: Random algorithm to generate all possible paths in dilatation G.

possible paths of node set covering all targets through self-direction action based on dilatation figure.

Random algorithm showed in Algorithm 4 may generate empty set. But through executing this algorithm repeatedly, a bigger set of feasible paths in dilatation can be generated, which can be used as initiate group for genetic algorithm. Discriminate algorithm based on genetic algorithm is shown in Algorithm 5.

5. Simulation Analysis

Simulation analysis is performed to multinode multi-interested target self-direction optimal coverage discriminate algorithm based on genetic algorithm [14]. The MATLAB 7.6.0 and genetic algorithm toolbox function are used. N multimedia sensor nodes and m interested targets are randomly sown into $400\text{ m} \times 400\text{ m}$ area. Sensing direction of node is randomly distributed in $[0, 2\pi]$ and every interested target should be covered by FoV disk of at least one node. While simulation, the number of sensor nodes is set as 100, sensing angle of sensing node is set as $\pi/3$, and sensing radius is set as 100 m. Ability of algorithm with 10, 20, and 30 interested targets is investigated individually. Algorithm

runs 100 times under every circumstance. Figure 5 shows the stability of multitarget self-direction coverage optimization by this algorithm under three circumstances. Floating error range of optimal results is less than 3 nodes. The floating range of algorithm running results increased slightly with augmented interested target.

Figure 6 shows optimal solution of target function and ability tracking of algorithm in different number of interested targets. It can be discerned that our algorithm can generate optimal solution with fewer iteration frequencies, which would increase with augmented interested target. Figure 7 shows the relationship between number of interested targets and optimal solution of target function. The size of minimal node set which can totally monitor interested targets increases linearly with increasing in number of interested targets. Every data in figure means average value of algorithm ran 100 times.

6. Conclusion

In this paper, the factor of rotation angle, rotation direction, and distance between node and interested target when multimedia sensor node self-directed cover interested target

```

Input: dilatation G
Output: minimal node set contented to target optimization

MAXGEN = 100; //maximal genetic algebra;
GGAP = 0.9; //generation gap;
trace = zeros(MAXGEN, 2); //initiate value of genetic algorithm ability tracking;
Repeatedly run algorithm in Algorithm 4 to generate a enough big feasible path set W;
Chrom = W; //initiate group
gen = 0;
ObjV = Target(Chrom); //calculate target function value (number of nodes) of initiate group;
WHILE gen < MAXGEN
    FitnV = ranking(ObjV); //allocate accommodation value
    SelCh = select("sus", TestChrom, FitnV, GGAP); //chose
    SelCh = recomb("xovsp", SelCh, 0.7); //recombinant
    SelCh = mutbga(SelCh, f); SelCh = fix(SelCh); //variation
    ObjVsel = Target(SelCh); //calculate target function value in descendant
    [Chrom ObjV] = reins(Chrom, SelCh, 1, 1, ObjV, ObjVsel); //re-insert
    gen = gen + 1;
    remove individual in descendant which can not totally cover target set;
    descendant after removal of un-contented individual named as Chrom2;
    ObjV2 = Target(Chrom2);
    trace(gen, 1) = min(ObjV2);
    trace(gen, 2) = mean(ObjV2);
END
RETURN minimal node set which can cover T through self-direction
    
```

ALGORITHM 5: Multinode multi-interested target self-direction optimal coverage discriminate algorithm based on genetic algorithm.

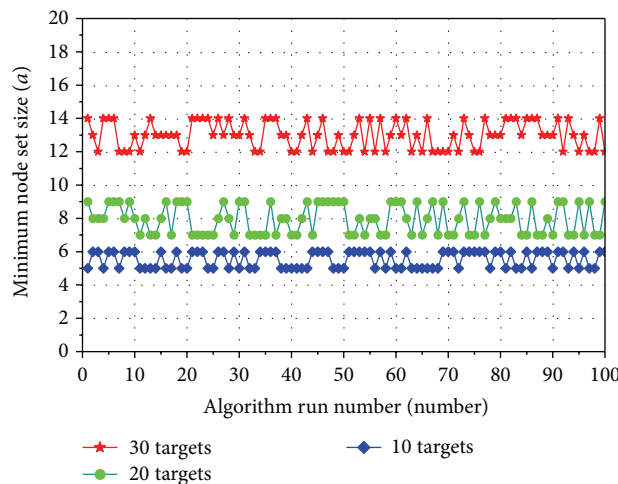


FIGURE 5: Stability of algorithm.

in self-directed MSN is discussed. Also we investigate single-node single-target, multinode multitarget, and single-node multitarget self-directed coverage optimization, so node can self-direct in maximal coverage expectation value, which means covering more closer targets with lesser rotation angle. For multinode multitarget self-directed coverage optimization, the hypothesis that all nodes have fixed sensing

direction in literature [11] is abandoned. The potential self-directed sensing direction in node is defined by number of interested targets in its FoV disk, which would more fit the feature of randomly deployed WMSN. Then the problem is abstracted into optimization problem with restrictive conditions. Genetic algorithm is used to discriminate. Also simulation analysis is performed. Further study may focus on

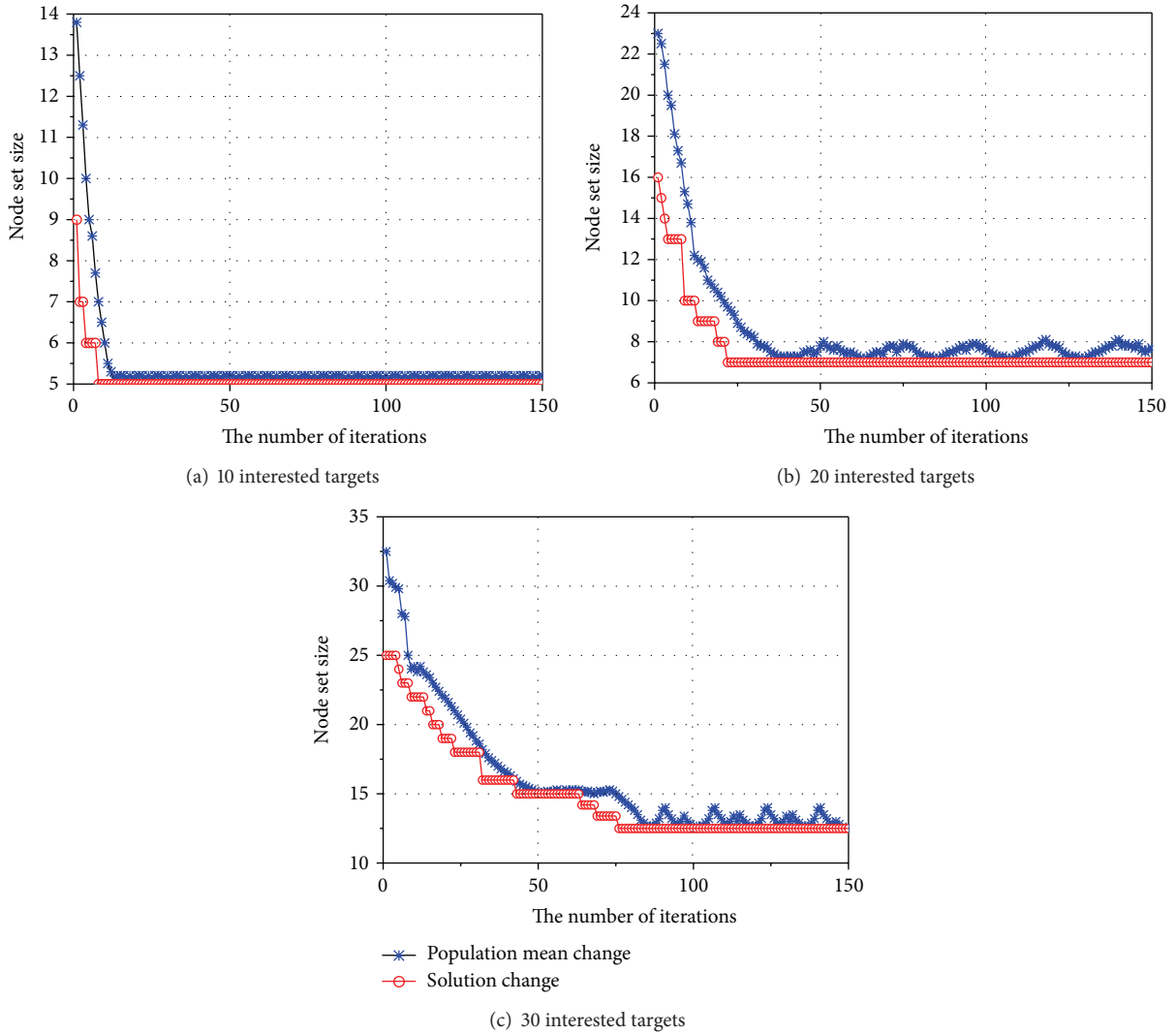


FIGURE 6: Optimal solution of target function and ability tracking of algorithm.

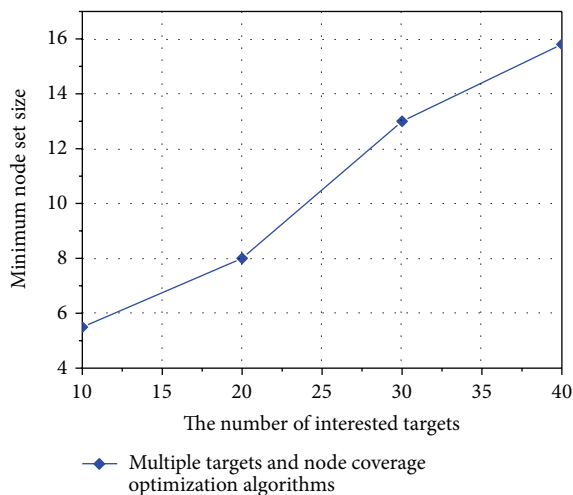


FIGURE 7: Relationship between number of interested targets and optimal solution of target function.

how to realize multinode multitarget self-directed coverage optimization with induction of coverage expectation based on minimal node covering interested target.

Conflict of Interests

The authors declare that there is no conflict of interests regarding the publication of this paper.

Acknowledgments

Foundation item: This paper is sponsored by Qing Lan Project and the National Natural Science Foundation of China (nos. 61170065, 61373017, 61171053, 61103195, and 61203217).

References

- [1] I. F. Akyildiz, T. Melodia, and K. R. Chowdhury, "A survey on wireless multimedia sensor networks," *Computer Networks*, vol. 51, no. 4, pp. 921–960, 2007.
- [2] I. F. Akyildiz, W. Su, Y. Sankarasubramaniam, and E. Cayirci, "Wireless sensor networks: a survey," *Computer Networks*, vol. 38, no. 4, pp. 393–422, 2002.
- [3] M. Huadong and T. Dan, "Multimedia sensor network and its research progresses," *Journal of Software*, vol. 17, no. 9, pp. 2013–2028, 2006.
- [4] A. Ghosh and S. K. Das, "Coverage and connectivity issues in wireless sensor networks: a survey," *Pervasive and Mobile Computing*, vol. 4, no. 3, pp. 303–334, 2008.
- [5] U. M. Erdem and S. Sclaroff, "Optimal placement of cameras in floorplans to satisfy task requirements and cost constraints," in *Proceedings of the 5th Workshop on Omnidirectional Vision, Camera Networks and Non-Classical Cameras (Omnivis '04)*, Prague, Czech Republic, May 2004.
- [6] N. Tezcan and W. Wang, "Self-orienting wireless multimedia sensor networks for occlusion-free viewpoints," *Computer Networks*, vol. 52, no. 13, pp. 2558–2567, 2008.
- [7] J. Wang, C. Niu, and R. Shen, "Priority-based target coverage in directional sensor networks using a genetic algorithm," *Computers and Mathematics with Applications*, vol. 57, no. 11-12, pp. 1915–1922, 2009.
- [8] M. Cardei, D. MacCallum, X. Cheng et al., "Wireless sensor networks with energy efficient organization," *Journal of Interconnection Networks*, vol. 3, no. 3-4, pp. 213–229, 2002.
- [9] D. Tian and N. D. Georganas, "A coverage-preserving node scheduling scheme for large wireless sensor networks," in *Proceedings of the 1st ACM International Workshop on Wireless Sensor Networks and Applications (WSNA '02)*, pp. 32–41, Atlanta, Ga, USA, September 2002.
- [10] P. Wan and C. Yi, "Coverage by randomly deployed wireless sensor networks," *IEEE Transactions on Information Theory*, vol. 52, no. 6, pp. 2658–2669, 2006.
- [11] M. Cardei and J. Wu, "Energy-efficient coverage problems in wireless ad-hoc sensor networks," *Computer Communications*, vol. 29, no. 4, pp. 413–420, 2006.
- [12] P. K. Sahoo, J. P. Sheu, and W. S. Lin, "Dynamic coverage and connectivity maintenance algorithms for wireless sensor networks," in *Proceedings of the 2nd International Conference on Communication System Software and Middleware and Workshops (COMSWARE '07)*, pp. 1–9, Bangalore, India, January 2007.
- [13] X. F. Han, X. Cao, E. L. Lloyd, and C. C. Shen, "Deploying directional sensor networks with guaranteed connectivity and coverage," in *Proceedings of the 5th Annual IEEE Communications Society Conference on Sensor, Mesh and Ad Hoc Communications and Networks (SECON '08)*, pp. 153–160, San Francisco, Calif, USA, June 2008.
- [14] T. He, C. Huang, B. M. Blum, J. A. Stankovic, and T. Abdelzaher, "Range-free localization schemes for large scale sensor networks," in *Proceedings of the 9th Annual International Conference on Mobile Computing and Networking (MobiCom '03)*, pp. 81–95, San Diego, Calif, USA, September 2003.

Research Article

RSSI-Based Smooth Localization for Indoor Environment

Yujian Wang, Bin Zhao, and Zhaohui Jiang

IPPF RD, Alcatel-Lucent Shanghai Bell Co. Ltd., Shanghai 201206, China

Correspondence should be addressed to Yujian Wang; yujian.wang@alcatel-sbell.com.cn

Received 9 May 2014; Accepted 3 June 2014; Published 29 June 2014

Academic Editor: Hongli Xu

Copyright © 2014 Yujian Wang et al. This is an open access article distributed under the Creative Commons Attribution License, which permits unrestricted use, distribution, and reproduction in any medium, provided the original work is properly cited.

Radio frequency (RF) technique, for its better penetrability over traditional techniques such as infrared or ultrasound, is widely used for indoor localization and tracking. In this paper, three novel measurements, point decision accuracy, path matching error and wrong jumping ratio, are firstly defined to express the localization efficiency. Then, a novel RSSI-based smooth localization (RSL) algorithm is designed, implemented, and evaluated on the WiFi networks. The tree-based mechanism determines the current position and track of the entity by assigning the weights and accumulative weights for all collected RSSI information of reference points so as to make the localization smooth. The evaluation results indicate that the proposed algorithm brings better localization smoothness of reducing 10% path matching error and 30% wrong jumping ratio over the RADAR system.

1. Introduction

Nowadays, location is the important information for many innovative applications [1]. For example, smart asset management (SAM) system requires the position of each asset. As the asset is moved from one place to another, the manager should master the physical movement in a real-time manner. With location information, the system helps to reduce the searching time of each asset and improve its usage efficiency for the enterprise. Obviously, it is of significant importance to determine the real-time position of each mobile entity (e.g., an asset), which is called *indoor localization or tracking*.

The techniques for indoor tracking are classified into two broad categories: non-RF and RF techniques. In the former category, non-RF methods, such as infrared or ultrasound, may be used alone or together with RF for indoor tracking [2, 3]. From the view of marketing, the additional equipments, such as accelerometer, compass, and gyroscope, increase the cost of the large-scale deployment. Besides, these techniques may not work well in the complicated indoor environment for its worse penetration. For instance, the signals will be blocked when the devices are buried in the users' wallets or bags [1].

As RF measurement (e.g., RSSI) will be easily obtained during the wireless communication, there are many RSSI-based methods for indoor localization. Previous work mostly cares about the position error, which denotes the average distance between the real position and located position.

However, this measurement cannot fully reflect the performance for continuous localization in practice. For example, the entity is moving from point *A* to point *B*. Whereas, as the instability and unreliability of RSSI, the obtained tracking path is *A-C-B*, though point *C* does not lie between point *A* and point *B*. In this case, though the one-shot wrong jumping may not greatly increase the average position error, this will result in wrong path determination. So that the users may regard the localization result as unreasonable for the wrong tracking path. To express the tracking efficiency, we call it smooth localization if the computed path by the algorithm is exactly the same as the real path for a mobile entity. However the multipath reflection and wireless interference bring some challenges to implement the smooth localization. (1) RSSI is not stable. The value of RSSI is determined by the transmission power, distance, transmission path, and so forth. Even between two fixed nodes, the RSSI value varies as time goes by. (2) RSSI is not always reliable. Transmission reliability will change under different scenarios. When the number of mobile entities is increasing, the communication interference increases, which reduces the transmission reliability. (3) There is no causal relationship between RSSI and Euclidean distance, so that large distance estimation is brought about by judging from RSSI information only.

The researchers have designed many algorithms to conquer one or some of the above challenges for indoor localization. For example, as there is no apparent function between

RSSI and Euclidean distance, several works [4] compute the nodes' localizations based on the connectivity information. Then, RSSI is used to enhance the location precision [5, 6]. However, there is mere work dealing with the unreliability and instability of RSSI, which make many algorithms unfit for the practical applications. The existing RF-based tracking systems mostly focus on the precise position or average position error. However, no apparent performance measurement has been studied for smooth localization. For example, the MERIT system [7] defines a new measurement for indoor localization, called area decision accuracy, to determine where the entity locates by comparing the average RSSIs of different areas. As RSSI is not always stable or reliable, it does not work well under the indoor environment. MERIT [7] requires the denser AP deployment and does not fit for the areas with different area sizes. As in the SAM application, wrong area decision will result in wrong asset searching and asset statistics. With the negative features of RSSI, smooth localization becomes an extremely difficult challenge for researchers. As we know, there is no special work aiming to smooth localization. The main contribution of this paper is as follows.

- (i) Three novel measurements, point decision accuracy, path matching error, and wrong jumping ratio, are defined to express the localization smoothness for indoor environment.
- (ii) A RSSI-based smooth localization (RSL) algorithm is proposed for the indoor localization. The algorithm first selects some reference points and constructs a connected graph for these points based on the architectural features. Then, reference points will be assigned weights and accumulative weights by the collected RSSI information. Finally, a novel tree-based mechanism is designed to estimate the moving track with high probability for smooth localization.
- (iii) The proposed algorithm is validated on the WiFi test bed. The evaluation results indicate that the proposed algorithm can get better localization smoothness compared with the previous works. For example, the RSL algorithm can reduce the path matching error and wrong jumping ratio by about 10% and 30% over the RADAR system.

In Section 2, the localization framework is introduced, and three novel performance measurements for smooth localization are defined. The RSSI-based smooth localization algorithm is discussed in detail in Section 3. The validation is described in Section 4 according to the above measurements. Finally, the conclusion is drawn in Section 5.

2. Localization Performance Measurement

2.1. Localization Framework. Many algorithms of previous work may locate the mobile entity to arbitrary positions in the field. However, as RSSI information is unstable and wireless transmission apt to be unreliable, the traditional RSSI-based methods might result in unstable localization. That is, the localization result will jump from one point to another, while

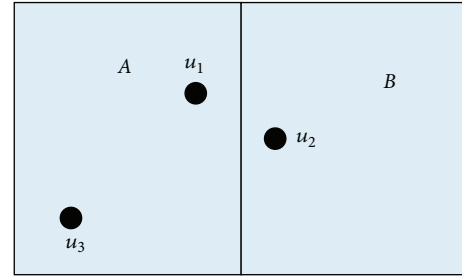


FIGURE 1: Illustration of localization measurement.

the entity is stationary to a fixed spot. To provide smooth localization, this procedure mainly consists of two steps: (1) RSSI sampling and (2) position determination. Like the previous method [8], the localization framework first selects many reference points (also called representational points) in the field. For example, the central point of a room will be selected to represent this room. The system samples the RSSI information on these discrete points for a durative period. In the runtime, the mobile entity will be located on some presampled positions by the collected RSSI information. In the second step, different mechanisms are designed to improve the localization performance. The main advantage of this framework is to increase the localization efficiency and stability compared with the previous mechanisms [7]. The task of this paper is to design efficient methods to improve the localization smoothness under this practical framework.

2.2. Localization Measurement Definition. The previous algorithms [5, 7–9] mostly take the average position error, which denotes the distance between the real position and located position, as the main performance measurement. However, this measurement cannot often reflect the real effect for indoor localization. For example, there are two rooms in a field, shown in Figure 1. Assume that the current position of a mobile entity is u_1 . Two localization algorithms obtain the different position results, denoted by and through RSSI information. From the view of average position error, position u_2 is closer to u_1 than to u_3 , so that theoretically the average position error between u_1 and u_2 is smaller than that of u_1 and u_3 . However, u_1 is located in the same room as u_3 . Thus, it is more reasonable to locate the mobile entity on position u_3 compared to position u_2 .

In the following, we will define some practical performance measurements for indoor localization. There are two different scenes for indoor localization. One is static, the other is mobile.

For static scenes, the entity mostly stays at one position or around for a long time. Under the above localization framework, each position in the field will be logically appointed to a reference point. For example, two points are in the same area or close to each other. We adopt the *point decision accuracy* (PDA) to measure the localization efficiency under the static scenes. In this case, point decision accuracy is defined as the correct probability that the mobile entity is located at the appointed reference point by the localization algorithm. For example, as shown in Figure 1, we regard that each point in

the area A is appointed to position u_3 , for they lie in the same room. The system collects the RSSI information for 100 time slots as the mobile entity is on point u_1 . If there are 90 time slots in which the localization result is u_3 , we regard that the point decision accuracy of this algorithm is about 0.9. If each area only contains one reference point, point decision is the same as area decision [7]. Thus, PDA is more general than area decision accuracy.

For mobile scenes, the entity continuously moves from one position to another. However, one may stay on a certain point for a short time compared with a long period. To reflect the effect of the practical movement, we will define two measurements to express the localization smoothness. One is called as *path matching error* (PME). We consider the discrete-time division. Assume that entity u locates on a point $p(t)$ in time slot t . Note that, the mobile entity may not locate on a reference point. In comparison, as each position will be logically appointed to a reference point in the field, we use the appointed reference point to denote the real position. That is, $p(t)$ is a reference point, to which the real position of entity u may be appointed. Then, a real path can be described as a position string $RP = p(1), \dots, p(n)$, where n is the total number of time slots. After information processing, the server may obtain the localization result $r(t)$ in time slot t . Note that, $r(t)$ is a reference point under the above localization framework. Thus a localization result path denoted by $LP = r(1), \dots, r(n)$ is obtained. To express the similarity between two paths, we compute their maximum common substring of two paths RP and LP , denoted by $MCS(RP, LP)$. Moreover, its length is denoted by $|MCS(RP, LP)|$. Then, PME is calculated as

$$PME(RP, LP) = 1 - \frac{|MCS(RP, LP)|}{n} \quad (1)$$

The other measurement is called *wrong jumping ratio* (WJR). The unstable and unreliable RSSI information will result in wrong jumping, which greatly debases the localization. Assume that the real track of a mobile entity is "1133." With RSSI information, the localization result is "1123." So, there is one wrong jumping from point 1 to point 2. Note that, this jumping will result in wrong path computation. WJR is defined as the average number of wrong localization jumping during 100 time slots. For example, the system collects the RSSI information and computes the localization for n time slots. The number of wrong localization jumping is m . Then, WJR is defined as

$$WJR = \frac{m}{n} \times 100. \quad (2)$$

The smooth localization aims to reduce the path matching error and to avoid the wrong localization jumping. Now, we give examples to illustrate the definitions of PME and WJR. For example, the real path consists of some discrete positions and is expressed by $RP = "1112233345"$. Assume that the first algorithm derives the path as $LP_1 = "1112223345"$. By the definition, the maximum common substring of RP and LP_1 is "111223345," and its length is 9. So, its path matching error is 0.1. Though LP_1 cannot fully be matched to RP , there is

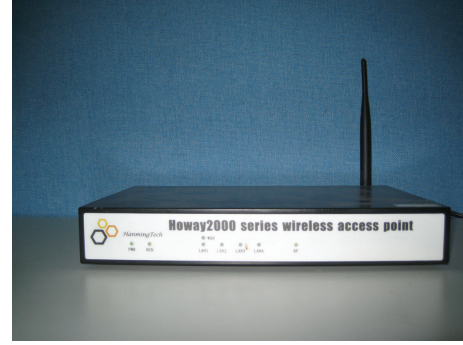


FIGURE 2: Access point.

no wrong jumping between two paths. Thus, the WJR of LP_1 is 0. This algorithm just locates the entity to point 3 with a delay. Assume the second algorithm obtains a path $LP_2 = "1142223345"$. Similarly, the maximum common substring of RP and LP_2 is "11223345," and its length is 8. As a result, its path matching error is 0.2. Observing the localization result LP_2 , there is one wrong localization jumping from point 1 to point 4, and its WJR is $(1/10) \times 100 = 10$. The third algorithm obtains a path $LP_3 = "1142233245"$. The maximum common substring of RP and LP_3 is "11223345," and its length is 8. Then, its path matching error is 0.2. However, there are two wrong jumping, from point 1 to point 4 and from point 3 to point 2, respectively. Its WJR is $(2/10) \times 100 = 20$. According to the above description, we regard that LP_1 is much smoother than paths LP_2 and LP_3 . Though LP_2 and LP_3 reach the same PME, LP_2 will work better than LP_3 for WJR.

3. Smooth Localization Algorithm Description

In this section, we will design a RSSI-based smooth localization (RSL) algorithm, which aims to obtain higher point decision accuracy, lower path matching error, and lower wrong jumping ratio. The RSL algorithm consists of three steps, reference point selection, graph construction, and localization determination, respectively.

3.1. System Equipments. Before algorithm description, we first introduce the main equipment in the system.

There are two main categories of equipments in the system. One is access point (AP), shown in Figure 2. Each AP can support the standard 802.11 b/g/n and is used to collect the detection packets from all the mobile entities in each time slot. Moreover, all access points can form a wireless backbone network and transmit the obtained RSSI information to the localization server. As WiFi networks are widely deployed, the localization system can be built on these wireless networks, which helps to save deployment costs. The other is WiFi-compatible card, shown in Figure 3. Each mobile entity will take a card, which locally broadcasts the detection packets to the neighboring access points. In the system, each card is only capable of wireless transmission, which is energy efficient, cheap, and fit for large-scale applications. After RSSI



FIGURE 3: WiFi-compatible card.

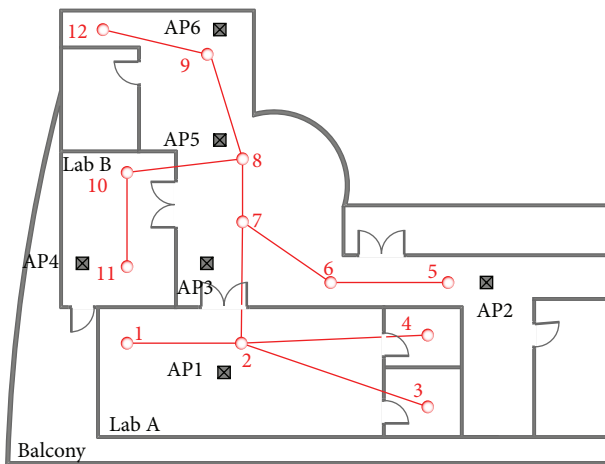


FIGURE 4: Reference point selection and graph construction.

collection, the localization server will determine the real-time position for each entity.

3.2. Reference Point Selection and RSSI Sampling. In this subsection, we first describe the rule for reference point selection in the target field. Inside the building, the fixed structures have formed the natural partitions, such as offices, meeting rooms, and aisles. Generally, a representational position will be selected in each area, such as points 3 and 4 in Figure 4. However, there are some rooms with a larger size. We will choose multiple reference points which are uniformly distributed in one room, such as points 10 and 11 in Figure 4. As the RSSI information varies much more in a large room, the selection of multiple reference points may help to improve the localization accuracy and efficiency. After selection of reference points, we sample the RSSI information on each reference point for a durative period, such as 30 minutes, and keep the sampling results into the localization database on the server. To save the time, multiple cards are used to sample the RSSI information on several reference points simultaneously. For a certain access point AP_i , the average RSSI value from the reference point j is denoted by μ_{ij} , and its variance is σ_{ij} .

Note that, in the underground mine environment, the working field is mostly a linear area. If a long corridor is regarded as one area, the relative distance from the entity to

AP might be large. To solve this, we divide the linear laneway into some “virtual areas,” in which the center position will be chosen as the reference point of this virtual area. The sparse division will decrease the localization accuracy, and the dense division may result in serious localization jumping, thus decreasing the localization smoothness. Given a long laneway, we deploy two access points with a distance of 100 m. Our testing shows that it is an efficient way to divide this laneway with 100 m into 5 virtual areas, where the length of each area is 20 m. In this way, the localization algorithm will satisfy both accuracy and smoothness.

3.3. Graph Construction for Reference Points. In this subsection, a connected graph G will be constructed for the reference points V , which is used to determine the track of each mobile entity and to improve the localization smoothness. According to the description, each reference point u belongs to a certain partition or area, denoted by $A(u)$. In the following, u and v are two reference points. We describe the rules for graph construction.

(1) $A(u)$ and $A(v)$ are two areas; that is, $A(u) \neq A(v)$. There are three cases to be discussed.

- (a) $A(u)$ and $A(v)$ are not connected or shared with a door. Two points are not connected either.
- (b) $A(u)$ and $A(v)$ are connected or shared with a door. Moreover, points u and v are the shortest point pair between two connected areas. Two points are connected.
- (c) $A(u)$ and $A(v)$ are connected or shared with a door. However, points u and v are not the shortest point pair between two connected areas. Two points cannot be connected.

(2) $A(u)$ and $A(v)$ are the same area; that is, $A(u) = A(v)$. Two points are also connected in the graph G . Generally, if there are more than two reference points in one area, they are all connected with others.

In this way, we have constructed an undirected graph G , illustrated in Figure 4. By rule 1-a, point 3 cannot be connected with point 7, for two areas are not connected. By rule 1-b, point 3 is connected with point 2. However, point 3 cannot be connected with point 1 according to rule 1-c. Followed by rule 2, point 10 and point 11 are connected, for they belong to the same area.

3.4. Tree-Based Smooth Localization. As described above, the time is divided into many discrete slots. For example, the length of each time slot is 1 second. During each time slot, the mobile entity will locally broadcast the detection message. The neighboring access points capture the detection message, compute the RSSI values, and transmit to the server. As a result, the server can obtain the RSSI information (or RSSI vector) about each mobile entity in this time slot. This vector can be expressed as $\{(AP_{i_1}, RSSI_{i_1}), \dots, (AP_{i_k}, RSSI_{i_k})\}$, where each item $(AP_{i_j}, RSSI_{i_j})$ denotes that access point AP_{i_j} has

detected the RSSI value of $RSSI_{i_j}$ from the mobile entity, and s is the number of RSSI values in the vector.

The previous works [8, 10] have proposed a RSSI-distance method to measure the matching similarity between the current RSSI vector and each sampled RSSI vector in the localization database. However, RSSI information between two fixed nodes is not stable as time passed and wireless transmission is apt to unreliable, which may lead to the incorrect localization result, worse path matching error, and wrong jumping ratio. Next, we will design a tree-based smooth localization (TSL) mechanism for practical indoor tracking. This subalgorithm contains three steps, weight assignment, accumulative weight computation, and localization determination.

In the first step, each reference point will be assigned a weight by RSSI information. For the mobile entity u , assume that the RSSI information detected by AP_i in current time slot is denoted by x_i . It is also assumed that the RSSI information obeys the Poisson distribution [11]. Thus, the probability that this entity locates on the position j from the view of AP_i is

$$P_{ij} = \frac{1}{\sigma_{ij}\sqrt{2\pi}} e^{-(x_i - \mu_{ij})^2 / 2\sigma_{ij}^2}, \quad (3)$$

where the constants μ_{ij} and σ_{ij} are introduced in the above subsection. The AP set that receives the RSSI information from mobile entity u in the time slot $t + 1$ is denoted by $\{AP_{i_1}, AP_{i_2}, \dots, AP_{i_s}\}$, where $i_1, i_2, \dots, i_s \in [1, m]$, and m is the number of access points in the system. The combination probability that the entity locates on the reference point j is denoted by P_j as

$$P_j = \prod_{k=1}^s P_{i_k j}. \quad (4)$$

With the gathered RSSI information during the time slot $t + 1$, we assign a weight $w(j)$ for each reference point j , which denotes the possibility that the mobile entity u may locate on this point with the collected RSSI information. The weight of each area is computed as

$$w(j) = \frac{P_j}{\sum_{k=1}^n P_k}, \quad (5)$$

where n is the number of reference points in the system. By this way, each reference point has been assigned a weight. Note that, the weight assignment method is not unique. We also can use another method for weight assignment. Though the weight is not strictly accurate, this is useful to predict the moving track.

The second step of TSL will compute the accumulative weight for each reference point on the constructed tree. For simplicity, $L(t)$ denotes the localization result of time slot t for the mobile entity u . To determine the localization in time slot $t + 1$, the algorithm constructs a width-first searching (WFS) tree T rooted at the point $L(t)$ for graph G . Each point j knows its children set, denoted by $chl(j)$. We compute the accumulative weight for point j , denoted by $Aw(j)$, as follows. For each leaf point in tree T , the accumulative weight is its

TSL sub-algorithm:

Step 1. Weight Assignment
 For each $AP_i \in \{AP_{i_1}, AP_{i_2}, \dots, AP_{i_s}\}$
 For each reference point j

$$P_{ij} = \frac{1}{\sigma_{ij}\sqrt{2\pi}} e^{-(x_i - \mu_{ij})^2 / (2\sigma_{ij}^2)}$$

$$P_j = \prod_{k=1}^s P_{i_k j}$$

$$w(j) = \frac{P_j}{\sum_{k=1}^n P_k}$$

Step 2. Accumulative Weight Computation
 Construct a tree T rooted at $L(t)$ for graph G
 For each reference point j

$$Aw(j) = \begin{cases} w(j), & j \text{ is a leaf} \\ w(j) + \sum_{k \in chl(j)} Aw(k), & \text{else} \end{cases}$$

Step 3. Localization Determination
 $Hop = 0;$
 $pos = null;$
 For each point j do
 If $Aw(j) \geq w_0$
 If $hop_j > Hop$
 $pos = j$
 $Hop = hop_j$
 If $Hop > 0$
 $L(t + 1) = pos$
 Else
 $L(t + 1) = L(t)$

ALGORITHM 1: Formal description of the TSL subalgorithm.

weight. For each intermediate point, the accumulative weight is the sum of accumulative weights of all the children nodes plus its weight. That is,

$$Aw(j) = \begin{cases} w(j), & j \text{ is a leaf} \\ w(j) + \sum_{k \in chl(j)} Aw(k), & \text{else.} \end{cases} \quad (6)$$

Finally, the TSL algorithm will search for a reference point whose accumulative weight is more than a threshold w_0 and furthest from the root, denoted by j_0 . Note that, the distance of two nodes is defined as the hop number between two nodes in the tree T . As a result, the mobile entity will locate on the point j_0 in time slot $t + 1$. That is, $L(t + 1) = j_0$. This indicates that the mobile entity has moved to the reference point j_0 in time slot $t + 1$ with very high probability. If there is no point whose accumulative weight is more than w_0 , we regard that the tracked entity is static during time slot $t + 1$. That is, $L(t + 1) = L(t)$. Though the entity may move in this time slot, the system cannot correctly judge the moving track as the RSSI information is unstable. The system will take a localization decision with a delay. As a result, the wrong localization jumping among several reference points will be avoided as possible. The TSL subalgorithm is formally described in Algorithm 1.

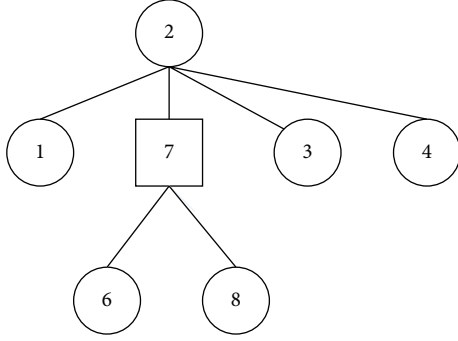


FIGURE 5: Illustration of localization smooth.

TABLE 1: An example of weights and accumulative weights.

Point	1	3	4	6	7	8
W	0.10	0.10	0.15	0.20	0.10	0.25
Aw	0.10	0.10	0.15	0.20	0.55	0.25

3.5. Illustration of the RSL Algorithm. We illustrate the RSL algorithm by an example. The reference points are chosen and drawn in Figure 4. The parameter w_0 is 0.50. For time slot t , assume that $L(t) = 2$. To compute the localization of time slot $t + 1$, the algorithm first constructs a WFS tree rooted at point 2, shown in Figure 5. Assume that the mobile entity is currently located around the reference point 8. After RSSI collection, we will compute the weight and accumulative weight of each point. By Table 1, the accumulative weights of point 6 and point 8 are 0.20 and 0.25, respectively. The accumulative weight of point 7 is the sum of weights of points 6, 7, and 8. So, $Aw(7) = 0.20 + 0.10 + 0.25 = 0.55$. According to the RSSI information, the algorithm may not distinguish the real-time position, either point 6 or point 8, for the mobile entity. However, the system can regard that the mobile entity has moved to point 7 with very high probability. We think it is reasonable, for point 7 to lie on the moving path from point 2 to the current position (i.e., point 8).

3.5.1. Algorithm Discussion. When locating the mobile entity in each time slot, the algorithm computes the weights and accumulative weights for all the reference points. As the numbers of reference points and mobile entities are both large, the requirement of computational capacity is very high for the practical localization system. To improve the computation efficiency, we propose a local searching mechanism for the RSL algorithm. Given a maximum velocity of the mobile entity, each entity will not move a long distance in a short time (such as 1 s, 2 s, etc.). For time slot $t + 1$, the RSL algorithm will construct a local tree T' whose maximum depth is not more than k rooted at $L(t)$, where k is predefined constant (e.g., 5 or 10) in the system.

4. Experimental Results

This section presents the numerical results to demonstrate the efficiency and smoothness of the proposed localization

algorithm. Though there are some localization algorithms based on RF techniques, they all require the additional conditions for indoor localization. For example, LANDMARC requires the dense deployment of beacon nodes, and the EZ algorithm [12] will occasionally fix the localization by GPS. Moreover, there is no special work on smooth localization. As a result, we mainly evaluate the performance of the RSL algorithm by comparing with the RADAR system [8] on the WiFi test platform. The RADAR system introduces two different methods of weight assignment, Euclidean distance, and Manhattan distance. So, we will denote RAD + Euc and RAD + Man to express the localization methods with different weight assignments. The experiments mainly observe the performance of three localization measurements, point decision accuracy, path matching error, and wrong jumping ratio, respectively. The definitions for these measurements are described in the above section. The accumulative weight threshold w_0 is set as 0.50. Besides, this proposed algorithm has little effect on the layout of the goods around the mobile entity regarding the spatial uniqueness of RSSI distribution.

4.1. Experiment Environment. The experiment is conducted at the Demo Center of Alcatel-Lucent Shanghai Bell Co. Ltd. There are totally 12 reference points and 6 access points in an area of about 400 squares meters. The reference points and AP deployments are also illustrated in Figure 4.

4.2. Numerical Results for Localization Algorithms. The first experiment mainly observes the performance of point decision accuracy for different algorithms. In particular, the mobile entity will statically locate in one place for continuous 115 time slots in the evaluations. By the collected RSSI information, we can compute the point decision accuracy for different algorithms. Table 2 gives the PDA comparison of different algorithms. On the average, the RSL algorithm improves the PDA by about 15% and 8% compared to the RAD + Euc and RAD + Man algorithms. Considering the highlighted worst case, RSL can enhance the worst PDA from 0.54 to 0.69. Thus, the proposed algorithm can get smoother localization compared to the RADAR system for the static case.

The second experiment observes the performance of path matching error and wrong jumping ratio for different algorithms. We select two different paths in the target field. One is 1-2-7-8-9-12, denoted by path A. The other is 5-6-7-8-10-11, denoted by path B. Moreover, the evaluations adopt two different moving patterns through each path. One is moving with the uniform velocity, denoted by pattern a. The other is similar with case a, except that the mobile entity will stay on each reference point for 10 seconds, denoted by pattern b. We give the evaluation results in Table 3 to Table 6, in which the numbers in the brackets denote the lasting time for different paths. For pattern a, the proposed algorithm reduces the path matching error of about 9.2% compared to the RADAR system. Moreover, the RSL algorithm decreases the wrong jumping ratio by at least 30% compared to the RADAR system from Tables 3 and 4. For moving pattern b, the RSL algorithm will reduce the path matching error of about 15.1% compared

TABLE 2: PDA comparison for different algorithms.

Number	Real position	RAD + Euc	RAD + Man	RSL
1	1	0.91	0.91	0.91
2	1	0.92	0.92	0.94
3	1	0.68	0.81	0.93
4	7	0.54	0.62	0.71
5	7	0.77	0.77	0.83
6	9	0.79	0.83	0.87
7	9	0.71	0.70	0.74
8	11	0.64	0.72	0.84
9	11	0.55	0.67	0.69

TABLE 3: Performance for path A under pattern a (64 s).

Number	Measurement	RAD + Euc	RAD + Man	RSL
1	PME	0.36	0.36	0.30
2	WJR	20.31	21.88	9.38

TABLE 4: Performance for path B under pattern a (61 s).

Number	Measurement	RAD + Euc	RAD + Man	RSL
1	PME	0.61	0.57	0.57
2	WJR	18.03	16.39	11.48

TABLE 5: Performance for path A under pattern b (109 s).

Number	Measurement	RAD + Euc	RAD + Man	RSL
1	PME	0.43	0.45	0.39
2	WJR	29.36	29.36	10.09

TABLE 6: Performance for path B under pattern b (104 s).

Number	Measurement	RAD + Euc	RAD + Man	RSL
1	PME	0.38	0.42	0.30
2	WJR	25	27.88	8.65

with the RADAR system. At the same time, the proposed algorithm also decreases the wrong jumping ratio by about 65% compared with the RADAR system from Table 5 and Table 6. That is due to the tree-based mechanism adopted in RSL, which helps to avoid the wrong jumps in localization as much as possible.

Based on the evaluation results, the proposed algorithm can improve three localization measurements compared with the previous algorithms, such as RAD + Euc and RAD + Man. In particular, the RSL algorithm will work excellently for the performance of wrong jumping ratio. As a result, this algorithm improves the localization smoothness compared with the previous algorithms intuitively.

5. Conclusion

In this paper, a novel RSL algorithm is designed, implemented, and validated. This algorithm purely depends on RF technique and uses a serial of access points to track the

mobile entities in the indoor environment. The evaluations demonstrate that this system is more effective than the previous related works. On our evaluation, the RSL algorithm can reduce the path matching error and wrong jumping ratio by about 10% and 30% compared with the previous systems. As the RSSI information is unstable, RSL may not be fully smooth. In the future, our team will continue to improve the point decision accuracy, path matching error, and wrong jumping ratio. In many applications, delay is another important measurement for localization. In the future, we will study the tradeoff between the smoothness and delay for real-time localization.

Conflict of Interests

The authors declare that there is no conflict of interests regarding the publication of this paper.

Acknowledgment

This paper is sponsored by the Chinese National Science and Technology Major Project 2012ZX03005009.

References

- [1] Cricket Projects, "Cricket v2 user manual," Tech. Rep., MIT Computer Science and Artificial Intelligence Lab, Cambridge, Mass, USA, 2004.
- [2] R. Want, A. Hopper, V. Falcao, and J. Gibbons, "Active badge location system," *ACM Transactions on Information Systems*, vol. 10, no. 1, pp. 91–102, 1992.
- [3] N. B. Priyantha, A. Chakraborty, and H. Balakrishnan, "The Cricket location-support system," in *Proceedings of the 6th Annual ACM International Conference on Mobile Computing and Networking (MOBICOM '00)*, pp. 32–43, ACM Press, New York, NY, USA.
- [4] N. Patwari and A. O. Hero III, "Using proximity and quantized RSS for sensor localization in wireless networks," in *Proceedings of the 2nd ACM International Workshop on Wireless Sensor Networks and Applications (WSNA '03)*, pp. 20–29, San Diego, Calif, USA, September 2003.
- [5] K. Yedavalli, B. Krishnamachari, S. Ravulath, and B. Srinivasan, "Ecolocation: a sequence based technique for RF localization in wireless sensor networks," in *Proceedings of the 4th International*

Symposium on Information Processing in Sensor Networks (IPSN '05), pp. 285–292, April 2005.

- [6] X. Shen, Z. Wang, P. Jiang, R. Lin, and Y. Sun, “Connectivity and RSSI based localization scheme for wireless sensor networks,” in *Proceedings of the International Conference on Intelligent Computing (ICIC '05)*, pp. 578–587, Hefei, China, August 2005.
- [7] Y. Lee, E. Stuntebeck, and S. C. Miller, “MERIT: MESH of RF sensors for indoor tracking,” in *Proceedings of the 3rd Annual IEEE Communications Society on Sensor and Ad Hoc Communications and Networks (Secon '06)*, pp. 545–554, September 2006.
- [8] P. Bahl and V. N. Padmanabhan, “RADAR: an in-building RF-based user location and tracking system,” in *Proceedings of the 19th Annual Joint Conference of the IEEE Computer and Communications Societies (IEEE INFOCOM '00)*, vol. 2, pp. 775–784, Tel Aviv, Israel, March 2000.
- [9] M. N. Lionel, Y. Liu, Y. C. Lau, and A. P. Patil, “LANDMARC: Indoor location sensing using active RFID,” *Wireless Networks*, vol. 10, no. 6, pp. 701–710, 2004.
- [10] M. Terwilliger, A. Gupta, V. Bhuse, Z. H. Kamal, and M. A. Salahuddin, “A localization system using wireless network sensors: a comparison of two techniques,” in *Proceedings of the Workshop on Positioning Navigation and Communication (WPNC '04)*, March 2004.
- [11] S. Saha, K. Chaudhuri, D. Sanghi, and P. Bhagwat, “Location determination of a mobile device using IEEE 802.11b access point signals,” in *Proceedings of the IEEE Wireless Communications and Networking (WCNC '03)*, vol. 3, pp. 1987–1992, 2003.
- [12] K. Chintalapudi, A. P. Iyer, and V. N. Padmanabhan, “Indoor localization without the pain,” in *Proceedings of the 16th Annual Conference on Mobile Computing and Networking (MobiCom '10)*, pp. 173–184, September 2010.

Research Article

A Novel Deployment Scheme Based on Three-Dimensional Coverage Model for Wireless Sensor Networks

Fu Xiao,^{1,2,3} Yang Yang,¹ Ruchuan Wang,^{1,2,3} and Lijuan Sun^{1,2,3}

¹ Nanjing University of Posts and Telecommunications, Nanjing 210003, China

² Jiangsu High Technology Research Key Laboratory for Wireless Sensor Networks, Nanjing 210003, China

³ Key Lab of Broadband Wireless Communication and Sensor Network Technology, Ministry of Education, Nanjing 210003, China

Correspondence should be addressed to Fu Xiao; xiaof@njupt.edu.cn

Received 4 May 2014; Accepted 4 June 2014; Published 17 June 2014

Academic Editor: Shukui Zhang

Copyright © 2014 Fu Xiao et al. This is an open access article distributed under the Creative Commons Attribution License, which permits unrestricted use, distribution, and reproduction in any medium, provided the original work is properly cited.

Coverage pattern and deployment strategy are directly related to the optimum allocation of limited resources for wireless sensor networks, such as energy of nodes, communication bandwidth, and computing power, and quality improvement is largely determined by these for wireless sensor networks. A three-dimensional coverage pattern and deployment scheme are proposed in this paper. Firstly, by analyzing the regular polyhedron models in three-dimensional scene, a coverage pattern based on cuboids is proposed, and then relationship between coverage and sensor nodes' radius is deduced; also the minimum number of sensor nodes to maintain network area's full coverage is calculated. At last, sensor nodes are deployed according to the coverage pattern after the monitor area is subdivided into finite 3D grid. Experimental results show that, compared with traditional random method, sensor nodes number is reduced effectively while coverage rate of monitor area is ensured using our coverage pattern and deterministic deployment scheme.

1. Introduction

With the development of wireless communication, sensor, and microelectromechanical system technology, wide application prospect is exhibited for wireless sensor networks, such as in military, environmental monitoring, health, medicine, smart home, and other areas, and it has shown a huge advantage especially in unmanned monitoring or harsh environment; thus wireless sensor networks act as an important basic perception network for internet of things (IOT). As one of the basic problems in infrastructure, widespread research interests have been attracted in coverage control and nodes' deployment. Research demonstrated that the deployment of sensor nodes reflects the cost and the performance of wireless sensor network by references [1, 2]. Reasonable deployment can obtain the optimum allocation of WSN resources; thus the perceived quality of the sensor network can be greatly enhanced. Given a sensor network, the coverage problem

is a leading indicator to measure the effect of deployment, which reflects sensor node's monitoring level in designated surveillance area [3]. However, most existing works on sensor deployment mainly concentrate on ideal two-dimensional planes. Actually in real applications, sensors are deployed on three-dimensional environments.

In this paper, a three-dimensional coverage model and optimum deployment scheme are proposed for wireless sensor networks. The rest of this paper is organized as follows. In Section 2, related works are introduced. The three-dimensional coverage problem in wireless sensor network and optimum coverage pattern based on cuboids is proposed in Section 3. In Section 4, the relationship between coverage and sensor nodes' radius is deduced, and also the minimum number of sensor nodes to maintain network area's full coverage is calculated. Experimental results show the effectiveness of our method in Section 5, and conclusion is made in Section 6.

2. Related Works

The deployment scheme is one of the most important problems in wireless sensor networks, which act as the fundamental infrastructure for target monitor. According to the different methods of node deployment, it can be divided into random deployment and deterministic deployment. Deterministic deployment is characterized by calculating the precise location of all sensor nodes and then placing each sensor node to obtain optimum connectivity and coverage by using the minimum number in monitoring area whose size and characteristic are known. This deployment divides network into lattices and then sensor nodes are placed. Dhillon and Chakrabarty [4, 5] proposed the maximum average coverage algorithm and the maximum minimum coverage algorithm, which are based on current node deployment; sensor nodes are placed assignably in the grid through the use of optimized strategy to meet point's coverage requirements in each grid and ensure that the number of sensor nodes is minimized, while these node deployment schemes focus primarily on the ideal 2D plane, including the optimum deployment patterns based on rules polygon [6].

In fact, sensor nodes are in realistic three-dimensional physical world, whose perception model and corresponding perception of the scene are 3D structure. However, traditional simplified 2D perception model and its cover-control algorithm are difficult to directly be applied in realistic 3D physical environment [7, 8]. With the development of research work and the expanded demand for practical application, 3D sensor network attracts much attention, such as acoustic sensor network and atmospheric monitoring sensor network which are based on 3D scene [9]. Particularly in recent years, with the rise of underwater sensor network, researchers started to think about the sensor nodes' perception model and its corresponding deployment method which is closer to the realistic physics world. Ammari and Das [10] presented a distributed redeployment method for underwater sensor network by adjusting the position of nodes in the depth of the underwater to reduce the overlapping area, so as to achieve maximum coverage of the network. Alam and Haas [11] designed the Reuleaux tetrahedron model to characterize k -coverage of a 3D field and investigated the corresponding minimum sensor spatial density, considering the full coverage problem and the connection problem of 3D field, through calculating and comparing the common volume business of polyhedro. Reference [12] concludes that, when the ratio of node's communication radius to sensing radius is equal to or greater than a fixed value, the cover effect of truncated octahedron is better than that of cube, which is six-prism and rhombic dodecahedron. Amac Guvensan and Gokhan Yavuz [13] analyzed and summarized the directional coverage models of wireless multimedia sensor networks and thought that the sensing models of the sensor nodes for the three-dimensional space are the current hot spot. Liu and Ma [14] studied the coverage problem of wireless sensor networks for rolling terrains, and they derived the expected coverage ratios under the stochastic sensors deployment based on digital elevation model (DEM). Topcuoglu et al. [15, 16] studied positioning and utilizing sensors on a 3D terrain; however

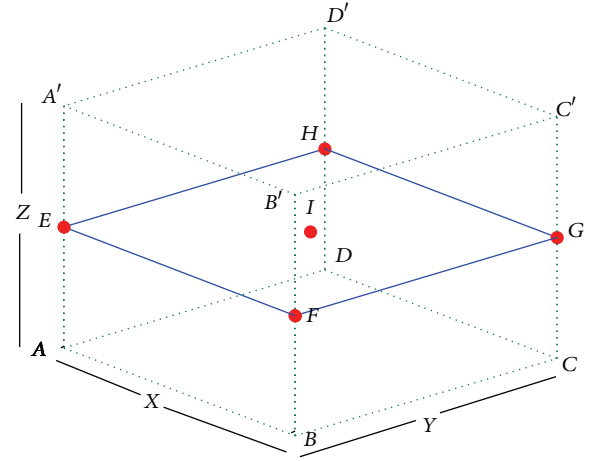


FIGURE 1: Coverage pattern Ω .

these works are not suited to 3D environments, such as atmospheric monitoring. And Kong et al. [17] studied the complex surface coverage problem in sensor networks.

The most related work is Zhang et al. [18], which studied the problem of constructing low-connectivity and full coverage for three-dimensional sensor networks. But they spend much work on ensuring k -connectivity ($k \leq 4$) for the whole network. Our work is based on this, while we put more emphasis on deterministic deployment for sensor networks to ensure the three-dimensional space coverage. The Optimum coverage pattern and relationship between coverage and sensor nodes' radius are deduced in this paper. Experimental results show that, compared with traditional random method, nodes number is reduced effectively, while coverage rate of monitor area is ensured using our method.

3. Three-Dimensional Coverage Problem in Wireless Sensor Network

3.1. Problem Description. In wireless sensor network, we consider that all sensors are of the same type and have sphere-shaped sensing field with radius r_s . 3D monitoring scene coverage can be abstracted as the ball-coverage problem, that is, covering a 3D space with several numbers of balls with the same radius, and each coverage area can be overlapped, and the requirement of completely coverage for monitoring area can be achieved finally. Considering the aim of prolonging network lifetime, optimization coverage problem corresponds to a specific problem that maximum covered a 3D space with least nodes.

3.2. Definitions

Definition 1 (coverage pattern Ω). In three-dimensional space, a coverage pattern Ω is defined as in Figure 1, where $ABCDA'B'C'D'$ is a cuboid with length, width, and height as x , y , and z and its volume is denoted by V . Plane $EFGH$ is located in the middle of cuboids $ABCDA'B'C'D'$. That is to

say, it is parallel to the bottom $ABCD$ at $z/2$ height and its center is point I .

Nodes deployment scheme is as follows: among five given points $E, F, G, H,$ and I , a sensor node is placed at each position.

Definition 2 (full coverage of coverage pattern Ω). Given a coverage pattern Ω and spheres with radius r centering at each point in five points $E, F, G, H,$ and I , Ω is fully covered if every point in cuboid $ABCD A' B' C' D'$ can be covered at least by one node.

Definition 3 (covering density). The ratio of the total volume of the five spheres with radius r to the volume of cuboid $ABCD A' B' C' D'$ is called covering density of Ω , which can be denoted by $\sigma(r, V)$ as follows:

$$\sigma(r, V) = \frac{20\pi r^3}{(3V)}. \tag{1}$$

Definition 4 (optimum coverage pattern Ω'). Given sensing range r , a coverage pattern is called the optimum coverage pattern Ω' if $\sigma(r, V)$ is minimum among all coverage patterns which ensure the full coverage.

4. Establishment of Optimum Coverage Pattern

From Definition 4, to obtain the optimum coverage pattern for each case, the maximum volume of cuboid $ABCD A' B' C' D'$ which is denoted by V_{\max} should be obtained, as shown in (2), where x, y, z are the lengths of three orthogonal edges in the cuboid, as follows:

$$V_{\max} = xyz. \tag{2}$$

V_{\max} can be obtained by solving a nonlinear optimization problem under constraints generated from full coverage. As shown in Figure 1, compared with other planes parallel to plane $EFGH$, plane $ABCD$ and plane $A' B' C' D'$ are the hardest to cover since the intersections of sensing spheres on these planes are smaller than those on other parallelograms. If planes $ABCD$ and $A' B' C' D'$ are covered, then any other parallelograms parallel to plane $EFGH$ in this coverage pattern must be covered. According to the geometrical symmetry, we can map the full coverage of 3D cuboid to 2D rectangle $ABCD$. We suppose that the radius of sensor nodes is r_s ; then the sensing range of nodes is a circular area with the radius r'_s in plane $ABCD$. As Figure 2 illustrated, we can get

$$r'_s = \sqrt{r_s^2 - \frac{z^2}{4}}. \tag{3}$$

The optimum full coverage of rectangle $ABCD$ is obtained if the intersections of five sensor nodes' sensing sphere are smallest in rectangle $ABCD$. According to the relationship

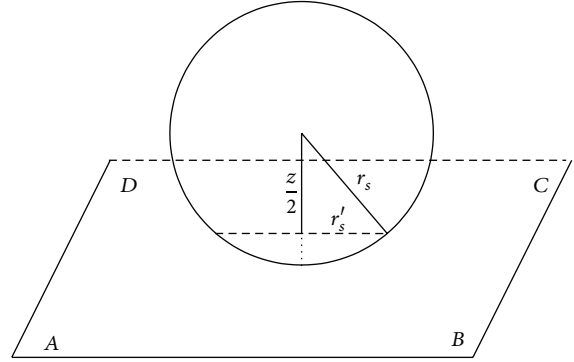


FIGURE 2: Coverage radius r'_s in plane $ABCD$.

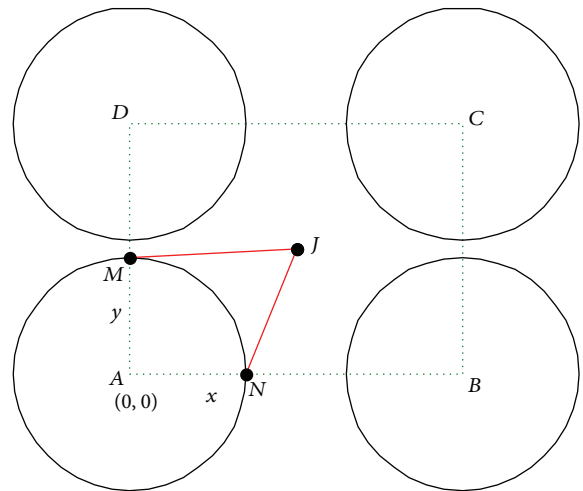


FIGURE 3: Case 1: relationship between x and y .

between length x , width y , and sensing radius, this problem can be divided into the following three cases.

Case 1. When $x > 2r'_s, y > 2r'_s$, as illustrated in Figure 3.

Let point J be the projection point of I at rectangle $ABCD$. Each sensing range of the sensor nodes at points $E, F, G, H,$ and I is circular area with radius r'_s centering at each point in $A, B, C, D,$ and J . Assuming that A is the origin point O at $(0, 0)$, B at $(x, 0)$, C at (x, y) , and D at $(0, y)$, then we can get coordinates of J as $(x/2, y/2)$, and $|AM| = |AN| = r'_s$ is known. To ensure that the uncovered area in rectangle $ABCD$ be covered by the circular area with radius r'_s centered at J , which is not covered by the other four circular areas with radius r'_s centering at A, B, C, D , the following conditions must be satisfied:

$$\begin{aligned} |JM| &\leq r'_s, \\ |JN| &\leq r'_s. \end{aligned} \tag{4}$$

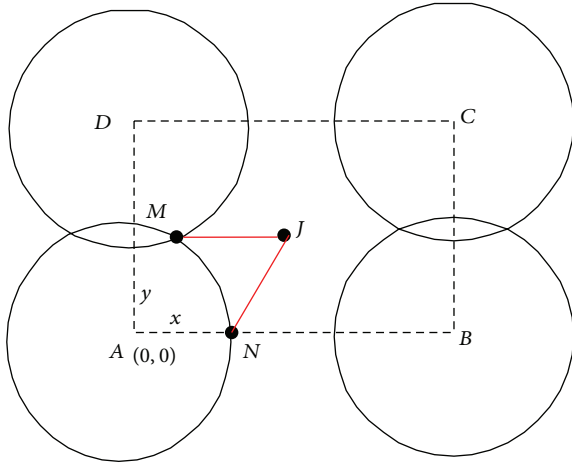


FIGURE 4: Case 2: relationship between x and y .

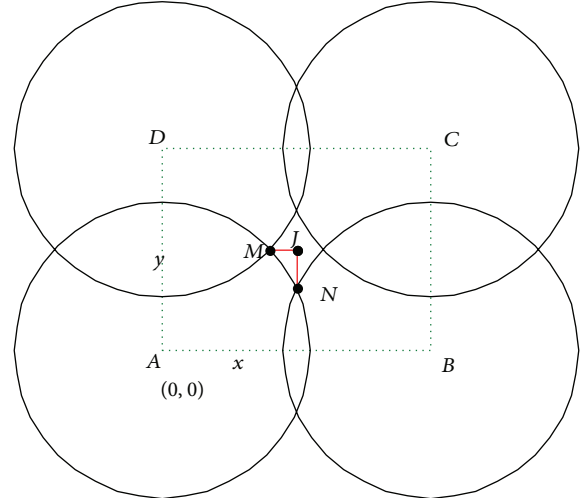


FIGURE 5: Case 3: relationship between x and y .

That is,

$$\begin{aligned}
 x^2 + y^2 - 4x\sqrt{r_s^2 - \frac{z^2}{4}} &\leq 0, \\
 x^2 + y^2 - 4y\sqrt{r_s^2 - \frac{z^2}{4}} &\leq 0, \\
 x &> 2\sqrt{r_s^2 - \frac{z^2}{4}}, \\
 y &> 2\sqrt{r_s^2 - \frac{z^2}{4}}, \\
 z &< 2\sqrt{r_s^2 - \frac{z^2}{4}}.
 \end{aligned} \tag{5}$$

Case 2. When $x > 2r'_s, y \leq 2r'_s$, as seen in Figure 4.

Similarly, to ensure that rectangle ABCD be fully covered by five sensor nodes, these following conditions should be satisfied:

$$\begin{aligned}
 x^2 + y^2 - 4x\sqrt{r_s^2 - \frac{z^2}{4}} &\leq 0, \\
 x^2 - y^2 - 4x\sqrt{r_s^2 - \frac{y^2}{4} - \frac{z^2}{4}} &\leq 0, \\
 x &> 2\sqrt{r_s^2 - \frac{z^2}{4}}, \\
 y &\leq 2\sqrt{r_s^2 - \frac{z^2}{4}}, \\
 z &< 2\sqrt{r_s^2 - \frac{z^2}{4}}.
 \end{aligned} \tag{6}$$

Case 3. When $x \leq 2r'_s, y \leq 2r'_s$, as illustrated in Figure 5.

Similarly, these following conditions should be satisfied to ensure rectangle ABCD be fully covered by five sensor nodes:

$$\begin{aligned}
 x^2 - y^2 - 4x\sqrt{r_s^2 - \frac{y^2}{4} - \frac{z^2}{4}} &\leq 0, \\
 y^2 - x^2 - 4y\sqrt{r_s^2 - \frac{x^2}{4} - \frac{z^2}{4}} &\leq 0, \\
 x &\leq 2\sqrt{r_s^2 - \frac{z^2}{4}}, \\
 y &\leq 2\sqrt{r_s^2 - \frac{z^2}{4}}, \\
 z &< 2\sqrt{r_s^2 - \frac{z^2}{4}}.
 \end{aligned} \tag{7}$$

Suppose the monitor environment is subdivided into cuboids with length x , width y , height z , and volume V and radius of sensor nodes is r_s . By solving formula (2) under constraint as conditions (5), (6), and (7), we can obtain the optimum coverage pattern Ω' as follows:

$$\begin{aligned}
 x &= \frac{2\sqrt{6}r_s}{3}, \\
 y &= \frac{2\sqrt{6}r_s}{3}, \\
 z &= \frac{2\sqrt{3}r_s}{3}, \\
 V &= \frac{16\sqrt{3}r_s^3}{9}.
 \end{aligned} \tag{8}$$

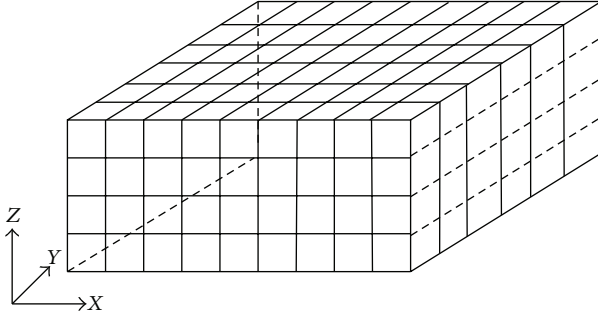


FIGURE 6: 3D mesh dissections on the actual environment.

5. Simulations and Analysis

Suppose that the actual environment is a 3D rectangular with length L , width W , and height H , respectively. The cuboid owns space division character, and the real 3D physical environment can be subdivided into several meshes to achieve full coverage by adopting our optimal cuboid coverage pattern. To facilitate analysis, we ignore the region boundary in actual environment.

5.1. 3D Mesh Dissections on Actual Environment. Based on structure size of the optimum coverage pattern, we subdivided the 3D rectangular into several small cuboids with length equal to $2\sqrt{6}r_s/3$, width equal to $2\sqrt{6}r_s/3$, and height equal to $2\sqrt{3}r_s/3$, as shown in Figure 6. We considered each little cuboid as an optimum coverage pattern and placed sensor nodes in Ω' . So the rectangular area is subdivided into cuboids as $ABCD A' B' C' D'$, and sensor nodes are deployed in the corresponding vertexes $A, B, C, D, A', B', C', D'$ and point I . Number N of nodes to achieve full coverage of 3D scene can be calculated as follows:

$$N = \left(\left(\left\lceil \frac{3L}{2\sqrt{6}r_s} \right\rceil + 1 \right) \times \left(\left\lceil \frac{3W}{2\sqrt{6}r_s} \right\rceil + 1 \right) + \left\lceil \frac{3L}{2\sqrt{6}r_s} \right\rceil \right) \times \left\lceil \frac{H}{2\sqrt{3}r_s/3} \right\rceil. \quad (9)$$

5.2. Performance Analysis. We have conducted a series of simulation experiments in this given 3D monitor region to compare the differences between random deployment and deterministic deployment regarding required number of sensor nodes. For instance, deploying the sensor nodes in a cube with edge length 1000 m, when $r_s = 30$ m, we need around 14645 nodes to achieve full coverage of scene according to formula (5). We compare with random covering algorithm in the same area under the conditions of meeting the same coverage. The comparison results are shown in Figure 6 (meet 80% coverage in Figure 7(a), meet 90% coverage in Figure 7(b), and meet 100% coverage in Figure 7(c)). We can see that the deterministic deployment pattern needs smaller number of nodes than the widely used random

TABLE 1: The influence of initial nodes number on the scene coverage rate.

Nodes number	Random strategy	Proposal strategy
10000	67.71%	68.60%
11000	71.16%	75.46%
12000	74.25%	82.32%
13000	77.00%	89.17%
14000	79.46%	96.03%
15000	81.65%	100%
16000	83.61%	100%
17000	85.37%	100%

deployment pattern under the conditions of meeting same coverage.

To validate the coverage influence of initial number of nodes on actual environment between random deployment and our deterministic deployment, we deploy the sensor nodes with $r_s = 30$ m in a cube with edge length of 1000 m and change the number of initial nodes. The results are shown in Table 1.

Table 1 illustrates that our deterministic deployment can make more coverage of actual area than random deployment under the condition of the same initial nodes. As illustrated by Zhang et al. [18], the constructing low-connectivity and full coverage three-dimensional sensor networks had been studied. Around 17200 nodes are needed to achieve 2-connectivity in a cube with edge length of 1000 m and sensor coverage radius equal to 30 m, which are the same as ours. While, in our scheme, we mainly focused on coverage and little attention had been paid to connective in sensor networks, no more than 15000 nodes are needed in our simulation results. Around 2200 nodes are reduced while coverage rate of monitor area is ensured using our method.

6. Conclusion and Future Work

This paper mainly proposes a coverage pattern which is based on cuboid structure through analyzing the coverage characteristics of 3D scene. By deducing the required number of sensor nodes for full coverage in 3D monitor space theoretically, we get the deployment positions of sensor nodes based on our coverage pattern after subdividing the finite 3D grid triangulation of network area. A series of simulation experiments proves the availability of this deterministic deployment scheme and significant number of sensor nodes can be saved using this proposed scheme.

The results of this paper are carried out on the basis of 0-1 sphere sensing model, and future research can be carried out following these directions: (1) extending this 0-1 sphere sensing model to probabilistic sphere sensing coverage model; (2) mobile sensor and k -coverage deployment scheme. Moreover, connectivity problem is still an open interesting problem in three-dimensional deployment domains.

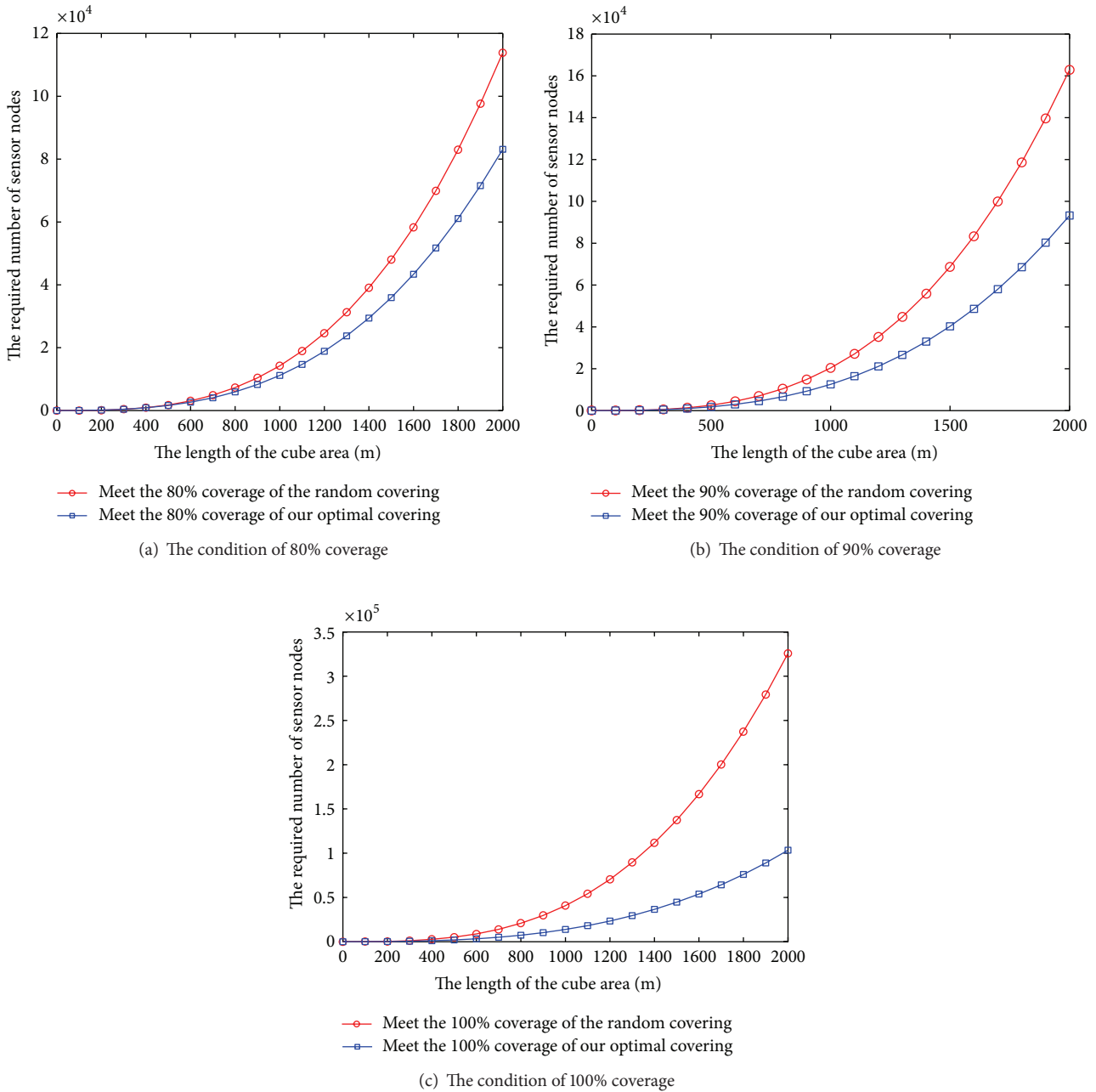


FIGURE 7: The condition of different coverage using our method and traditional random method.

Conflict of Interests

The authors declare that there is no conflict of interests regarding the publication of this paper.

Acknowledgments

This research is supported by National Natural Science Foundation of China (nos. 61373137, 61373017, 61170065, and 61171053), Six Industries Talent Peaks Plan of Jiangsu (no. 2013-DZXX-014), Scientific Technological Support Project of

Jiangsu (no. BE2012755), Scientific Research & Industry Promotion Project for Higher Education Institutions (JHB2012-7), and Jiangsu Qinglan Project.

References

[1] O. E. Onur, C. Ersoy, H. Deliç, and L. Akarun, "Surveillance wireless sensor networks: deployment quality analysis," *IEEE Network*, vol. 21, no. 6, pp. 48-53, 2007.

[2] S. Kumar and D. K. Lobiyal, "Sensing coverage prediction for wireless sensor networks in shadowed and multipath

- environment,” *The Scientific World Journal*, vol. 2013, Article ID 565419, 11 pages, 2013.
- [3] J. Heidemann, W. Ye, J. Wills, A. Syed, and Y. Li, “Research challenges and applications for underwater sensor networking,” in *Proceedings of the IEEE Wireless Communications and Networking Conference (WCNC '06)*, pp. 228–235, Las Vegas, Nev, USA, April 2006.
- [4] S. S. Dhillon and K. Chakrabarty, “Sensor placement for grid coverage under imprecise detections,” in *Proceeding of the International Conference on Information Fusion*, pp. 1581–1587, Annapolis, Md, USA, July 2002.
- [5] S. S. Dhillon and K. Chakrabarty, “Sensor placement for effective coverage and surveillance in distributed sensor networks,” in *Proceedings of the IEEE Wireless Communications and Networking Conference*, pp. 1609–1614, New Orleans, La, USA, March 2003.
- [6] X. L. Bai, Z. Q. Yun, D. Xuan, T. H. Lai, and W. Jia, “Deploying four-connectivity and full-coverage wireless sensor networks,” in *Proceedings of the 27th IEEE Communications Society Conference on Computer Communications (INFOCOM '08)*, pp. 296–300, Phoenix, Ariz, USA, April 2008.
- [7] H. M. Ammari and S. K. Das, “Critical density for coverage and connectivity in three-dimensional wireless sensor networks using continuum percolation,” *IEEE Transactions on Parallel and Distributed Systems*, vol. 20, no. 6, pp. 872–885, 2009.
- [8] D. Pompili, T. Melodia, and I. F. Akyildiz, “Three-dimensional and two-dimensional deployment analysis for underwater acoustic sensor networks,” *Ad Hoc Networks*, vol. 7, no. 4, pp. 778–790, 2009.
- [9] K. Akkaya and A. Newell, “Self-deployment of sensors for maximized coverage in underwater acoustic sensor networks,” *Computer Communications*, vol. 32, no. 7, pp. 1233–1244, 2009.
- [10] H. M. Ammari and S. K. Das, “A study of k-coverage and measures of connectivity in 3D wireless sensor networks,” *IEEE Transactions on Computers*, vol. 59, no. 2, pp. 243–257, 2010.
- [11] S. N. Alam and Z. J. Haas, “Coverage and connectivity in three-dimensional networks,” in *Proceedings of the ACM MobiCom*, pp. 346–357, Los Angeles, Calif, USA, September 2006.
- [12] M. K. Watfa and S. Commuri, “The 3-dimensional wireless sensor network coverage problem,” in *Proceedings of the IEEE International Conference on Networking, Sensing and Control (ICNSC '06)*, pp. 856–861, Gainesville, Fla, USA, May 2006.
- [13] M. Amac Guvensan and A. Gokhan Yavuz, “On coverage issues in directional sensor networks: a survey,” *Ad Hoc Networks*, vol. 9, no. 7, pp. 1238–1255, 2011.
- [14] L. Liu and H. Ma, “On coverage of wireless sensor networks for rolling terrains,” *IEEE Transactions on Parallel and Distributed Systems*, vol. 23, no. 1, pp. 118–125, 2012.
- [15] H. R. Topcuoglu, M. Ermis, and M. Sifyan, “Positioning and utilizing sensors on a 3-D terrain part I-theory and modeling,” *IEEE Transactions on Systems, Man and Cybernetics C: Applications and Reviews*, vol. 41, no. 3, pp. 376–382, 2011.
- [16] H. R. Topcuoglu, M. Ermis, and M. Sifyan, “Positioning and utilizing sensors on a 3-D terrain part II-Solving with a hybrid evolutionary algorithm,” *IEEE Transactions on Systems, Man and Cybernetics C: Applications and Reviews*, vol. 41, no. 4, pp. 470–480, 2011.
- [17] L. Kong, M. Zhao, X. Liu, Y. Liu, M. Wu, and W. Shu, “Surface coverage in sensor networks,” *IEEE Transaction on Parallel and Distributed Systems*, vol. 25, no. 1, pp. 234–243, 2014.
- [18] C. Zhang, X. Bai, J. Teng, D. Xuan, and W. Jia, “Constructing low-connectivity and full-coverage three dimensional sensor networks,” *IEEE Journal on Selected Areas in Communications*, vol. 28, no. 7, pp. 984–993, 2010.